Novel Thin Film Nanocomposite Membranes with Improved Properties for Enhanced Desalination Performance

Masoumeh Zargar

B.Sc. (Hons), M.Sc.

Thesis submitted for the degree of

Doctor of Philosophy

School of Chemical Engineering

Faculty of Engineering, Computer & Mathematical Sciences

The University of Adelaide, Australia

January 2016

Dedication

This thesis is deeply dedicated to:

My lovely parents, Parvin and Naser, for their great supports and continuous care

My amazing husband, Alireza, for his love, understanding, encouragements and sacrifices

Declaration

I certify that this work contains no material which has been accepted for the award of any other degree or diploma in my name, in any university or other tertiary institution and, to the best of my knowledge and belief, contains no material previously published or written by another person, except where due reference has been made in the text. In addition, I certify that no part of this work will, in the future, be used in a submission in my name, for any other degree or diploma in any university or other tertiary institution without the prior approval of the University of Adelaide and where applicable, any partner institution responsible for the joint-award of this degree.

I give consent to this copy of my thesis when deposited in the University Library, being made available for loan and photocopying, subject to the provisions of the Copyright Act 1968.

The author acknowledges that copyright of published works contained within this thesis resides with the copyright holder(s) of those works.

I also give permission for the digital version of my thesis to be made available on the web, via the University's digital research repository, the Library Search and also through web search engines, unless permission has been granted by the University to restrict access for a period of time.

Masoumeh Zargar Date: 01.10.2015

List of Publications

The doctoral thesis is prepared in "Publication" style according to the "specifications for Thesis (2015)" of the University of Adelaide. It includes publications that have been published, submitted for publication, or ready to be submitted:

- M. Zargar, B. Jin and S. Dai*, In Membrane Processing for Dairy Ingredient Separation, ed. J. D. Kang Hu, Wiley-Blackwell, 2015, Ch. Development and application of reverse osmosis for separation p. 139 (ISBN: 978-1-118-59017-1).
- M. Zargar, B. Jin* and S. Dai*, An integrated statistic and systematic approach to determine synthesis-performance correlation of thin film composite reverse osmosis membranes, submitted to Industrial & Engineering Chemistry Research (IE-2105-019756).
- M. Zargar, Y. Hartanto, B. Jin* and S. Dai*, Understanding functionalized nanoparticle incorporation in thin film composite membranes: interaction and desalination performance, submitted to Journal of Membrane Science (JMS-15-1287)
- M. Zargar, Y. Hartanto, B. Jin* and S. Dai*, Hollow mesoporous silica nanoparticles: a peculiar structure for thin film nanocomposite membranes, submitted to the ACS Applied Materials & Interfaces (am-2015-094259).
- M. Zargar, Y. Hartanto, B. Jin* and S. Dai*, Polyethylenimine modification of silica nanoparticles: a positive approach to develop sustainable thin film nanocomposite membranes, will be submitted.

Some relevant components of the work have been presented in conferences and symposiums:

- M. Zargar, B. Jin, S. Dai, Static protein adsorption on nanocomposite membranes: the contribution of nanofillers' surface functionality, ICONN 2016 - International Conference on Nanoscience and Nanotechnology, 7-11 Feb 2016, Canberra, Australia.
- M. Zargar, Y. Hartanto, S. Dai, B. Jin, Thin film nanocomposite membranes:

which medium to choose for nanoparticle integration, 12th International Conference on Membrane Science and Technology (MST2015), 1-3 November 2015, Tehran, Iran.

- M. Zargar, S. Dai, B. Jin, Thin film composite reverse osmosis membranes hybridized with surface modified silica nanoparticles for enhanced desalination performance, 2nd International Conference on Desalination using Membrane Technology, 26-29th July 2015, Singapore.
- M. Zargar, S. Dai, B. Jin, An optimization strategy to investigate the structure-performance correlation of thin film composite reverse osmosis membranes, 2nd International Conference on Desalination using Membrane Technology, 26-29th July 2015, Singapore.
- M. Zargar, S. Dai, B. Jin, An optimization strategy to fabricate thin film composite reverse osmosis (TFC-RO) membranes, RACI SA Student polymer & Bionanotechnology Symposium (SASPBS14), 29th August 2014, Adelaide, South Australia.
- M. Zargar, S. Dai, B. Jin, Effect of solid and porous nanoparticles' incorporation at low concentration into the polymeric membranes' structure, RACI SA Student polymer & Bionanotechnology Symposium (SASPBS14), 29th August 2014, Adelaide, South Australia.
- M. Zargar, S. Dai, B. Jin, Fabrication and characterization of uniform mesoporous silica nanoparticles with the average particle size of 100 nm, The International Conference on Nanoscience and Nanotechnology (ICONN 2014), 2-6 February 2014, Adelaide Convention Centre, South Australia.
- M. Zargar, B. Jin, S. Dai. Fabrication and characterization of polyamide thin film composite membranes, RACI SA Student polymer & Bionanotechnology Symposium (SASPBS13), 4th October 2013, Adelaide, South Australia.

I have also co-authored the following publications during my PhD candidature:

- Y. Hartanto M. Zargar, H. Wang, B. Jin* and S. Dai*, Thermo-responsive acidic microgels as functional draw agents for forward osmosis desalination, submitted

to Environmental Science & Technology (es-2015-04123d).

- Y. Hartanto, M. Zargar, B. Jin*, S. Dai*, Cationic thermos-responsive microgels as functional draw agents for forward osmosis desalination, will be submitted.

Acknowledgments

One of the joys of completion is to look over the journey past and remember all the friends and family who have helped and supported me along this long but fulfilling road.

First of all, I would like to express my profound appreciation and thanks to my lovely supervisors, Associate Professor Bo Jin who has always supported me and behaved like a father to me when I faced the difficult situations in my PhD mission and life and Associate Professor Sheng Dai who has always supported me with his generosity, care and deep technical knowledge. They were tremendous mentors for me. Without their enthusiastic supervision, inspiration, guidance and endless supports, completion of this thesis would not have been possible. I would like to sincerely thank them for encouraging my research and for allowing me to grow as a researcher. I owe them my confidence in speech and my research skills. Words cannot express the deepness of my gratitude to them.

I would like to give special thanks to all my group members and lab mates for their helps and supports. Working with them was a real joy. Special thanks to Mr Yusak Hartanto for his research contributions and fruitful discussions.

My grateful thanks go to the School of Chemical Engineering staff and administration for their individual helps. Special thanks to the Chemical Engineering workshop team, Mr Jason Peak, Mr Jeffrey Hiorns and Mr Michael Jung who always were ready to assist without making me feel indebted. Their immense supports for the setups establishment and helps to solve the problems of the instruments are priceless. Also thanks to Dr Tian Yi Ma for his help with N_2 sorption characterization.

Special thanks to my fellow friends who supported me and incented me to strive towards my goal: Ms Kiana Kashefi, Dr Sona Taheri, Dr Hamideh Elekaei Behjati, Dr Moein Navvab Kashani, Mrs Bita Bayatsarmadi, Mrs Shervin Kabiri, Ms Mahdieh Nemati, Dr Hadi Madani, Dr Sara Azari, Mrs Hanaa Heqab, Dr Sanaz Orandi, Mrs Mailin Misson, Dr Amir Mellati and Dr Meisam Valizadeh Kiamahaleh.

I would also like to acknowledge the University of Adelaide for IPRS scholarship to support me for my PhD study.

Last but not list, special thanks to my family. Words cannot express how grateful I am to my mother, father, my mother-in law and father-in-law, for all of the sacrifices that they've made on my behalf. Their prayer for me was what sustained me thus far. At the end, I would like to express my deep appreciation to my husband 'Alireza', who has always been my best friend. His unconditional support, encouragement, quiet patience and unwavering love were undeniably the bedrock upon which the past nine years of my life have been built. Without his supports, I could not surely conduct this work.

Abstract

Nowadays, polymeric thin film composite (TFC) membranes have received increasing applications for separation and purification processes such as desalination and wastewater treatment. The development of nanotechnology has opened new frontiers in the advancement of TFC membranes. The incorporation of nanomaterials into the thin film polyamide (PA) layer of TFC membranes, making a structure known as thin film nanocomposite (TFN) membrane, can offer the advantages of both inorganic nanofillers and organic polymeric membranes. However, the possibility of nanoparticles' leakage and their low compatibility with organic membranes make the successful fabrication of TFN membranes challenging. Hence, investigating the structure-performance correlation of TFC/TFN membranes and their interactions with the incorporated nanomaterials is of great importance.

In my PhD project, a serial of TFC membranes incorporated with variously sized, structured and surface functionalized silica nanoparticles have been developed and extensively characterized with the aim to advance the knowledge of interfacial interactions between inorganic nanomaterials and the thin film PA layer of TFC membranes.

A statistical analysis was applied to study some key fabrication parameters of TFC membranes including PSF concentration in phase separation and aqueous phase soaking time and heat curing time in the interfacial polymerization course. Our findings highlighted the importance of considering interactions when devising a strategy to fabricate TFC membranes in order to optimize the overall desalination performance.

After the study of the TFC fabrication parameters, fabrication of TFN membranes was performed to get a better understanding on the interfacial interactions between nanoparticles and TFC membranes. SN with different sizes (50 nm and 100 nm) and surface functionalities (hydroxyl, amine or epoxy) were synthesized and successfully incorporated into TFC membranes. Desalination performance evaluation of the TFN membranes showed that no matter which functional group was present on SN, the

resulting TFN membranes had higher water flux and comparable or higher salt rejection compared with the TFC membrane without nanoparticles. In addition, nanoparticle surface functionalization using epoxy and amine moieties facilitated the chemical interaction between SN and the TFC membranes, resulting in TFN membranes with higher crosslinking density of their PA selective layer and improved performance stability.

After studying the solid SN, hydrophilic hollow mesoporous silica nanoparticles (HMSN) have been used to fabricate novel TFN membranes in order to study the contribution of this peculiar porous structure on the properties and desalination performance of the resulting TFN membranes. The HMSN with an average particle size of ~ 68 nm were synthesized and incorporated into TFC membranes. The performance evaluation results revealed that with 0.03 wt % HMSN incorporation, water flux could improve up to 40 percent without obvious alteration of the salt rejection. Moreover, the compaction resistance of the resulting membranes was enhanced after HMSN incorporation.

To enhance the compatibility of introduced SN with the PA layer, polyethyleneimine (PEI) modified SN (SN-PEI) were fabricated and incorporated into the TFC membranes. Introduction of SN-PEI to the TFC membranes could facilitate the formation of strong covalent bonds between SN-PEI and PA layer, improve the compatibility of SN with the organic PA and enhance the physicochemical properties of the resulting TFN membranes. The cross-flow filtration performance evaluation of the fabricated membranes showed improved water flux and salt rejection capability in addition to a higher compaction resistance for the developed TFN membranes.

This thesis project has attempted to advance fundamental knowledge of the nanocomposite formation and fundamental processes governing water transport through reactive nanostructure to guide the development of nanoparticle-enabled multifunctional membranes.

Table of Contents

Declaration i

List of Publications ii

Acknowledgments v

Abstract vii

Table of Contents ix

List of Tables xiii

List of Figures xiv

1. Introduction 1

1.1. Background and project objectives 2

1.2. Thesis Outline 4

2. Literature Review 9

2.1. Introduction 10

2.2. Reverse Osmosis and its Working Mechanism 11

2.3. Reverse Osmosis Membranes 12

2.3.1. Inorganic reverse osmosis membranes 13

2.3.2. Polymeric reverse osmosis membranes 13

2.3.3. Thin film composite reverse osmosis membranes 15

2.4. Membrane Modules and Configurations 17

2.4.1. Spiral wound configuration 17

2.4.2. Hollow fiber, flat sheet and tubular configurations 18

2.5. Transport Mechanisms and Models in Reverse Osmosis Membranes 20

2.5.1. Diffusion-based models 20

2.5.2. Pore models 23

2.6. Reverse Osmosis Process 26

2.6.1. Overview of the process and performance evaluation in reverse osmosis membranes 26

2.6.2. Parameters affecting performance of reverse osmosis membranes 27

2.7. Technical and Economic Challenges 30

2.7.1. Concentration polarization 30

2.7.2. Fouling 31

2.7.3. Energy 34

2.8. Reverse Osmosis Process in Dairy Industry 35
2.8.1. Application of reverse osmosis membranes in dairy industry 35
2.8.2. Factors affecting the performance of reverse osmosis membranes in dairy processing..... 38
2.8.3. Concentration polarization and fouling of reverse osmosis membranes during milk concentration..... 39
2.9. Current Development in Reverse Osmosis Membranes 41
2.9.1. Thin film nanocomposite reverse osmosis membranes..... 41
2.9.2. Membrane surface modification and process optimization..... 42
2.10. Conclusions and Outlooks..... 43
3. An Integrated Statistic and Systematic Approach to Study the Structure-Performance Correlation of Thin Film Composite Reverse Osmosis Membranes for Desalination..... 52
3.1. Abstract 53
3.2. Introduction 54
3.3. Materials and Methods 56
3.3.1. Materials..... 56
3.3.2. TFC-RO membrane fabrication 56
3.3.3. Membrane Characterization 58
3.3.4. Membrane performance evaluation..... 58
3.4. Results and Discussion..... 59
3.4.1. Design of experiments and statistical analysis 59
3.4.2. Effect of PSF concentration and its significant interactions 67
3.4.3. Effect of aqueous phase soaking time and its significant interactions 69
3.4.4. Effect of heat curing time and its interactions..... 70
3.5. Conclusions 71
3.6. Supporting Information 75
4. Understanding Functionalized Nanoparticle Incorporation in Thin Film Composite Membranes: Interactions and Desalination Performance..... 80
4.1. Abstract 81
4.2. Introduction 82
4.3. Experimental 84
4.3.1. Materials..... 84
4.3.2. Synthesis and surface modification of silica nanoparticles..... 84
4.3.3. Fabrication of TFC and SN-TFC membranes 85

4.3.4. Characterization of nanoparticles, TFC and SN-TFC membranes 86
4.3.5. Membrane performance evaluation 88
4.4. Results and Discussion 89
4.4.1. Characterization of fabricated nanoparticles 89
4.4.2. Characterization of TFC and SN-TFC membranes 90
4.4.3. Performance evaluation of TFC and SN-TFC membranes 96
4.5. Conclusions 100
4.6. Supporting Information 106
5. Hollow Mesoporous Silica Nanoparticles: a Peculiar Structure for Thin Film Nanocomposite Membranes 115
5.1. Abstract 116
5.2. Introduction 117
5.3. Experimental 118
5.3.1. Materials 118
5.3.2. Fabrication of HMSN 119
5.3.3. Fabrication of TFC and TFN membranes 119
5.3.4. Characterization of nanoparticles, TFC and TFN membranes 120
5.3.5. Membrane performance evaluation 122
5.4. Results and Discussion 122
5.4.1. Synthesis and characterization of HMSN 122
5.4.2. Characterization of TFN membranes 127
5.4.3. Desalination performance of TFN membranes 129
5.5. Conclusions 132
5.6. Supporting Information 138
6. Polyethyleneimine Modification of Silica Nanoparticles: a Positive Approach to Develop Sustainable Thin Film Nanocomposite Membranes 142
6.1. Abstract 143
6.2. Introduction 144
6.3. Experimental 146
6.3.1. Materials 146
6.3.2. Fabrication of PEI modified silica nanoparticles (SN-PEI) 146
6.3.3. Fabrication of TFC/TFN membranes 147
6.3.4. Characterization 148

6.3.5. Membrane performance evaluation 149
6.4. Results and Discussion 150
6.4.1. Synthesis and characterization of the surface modified nanoparticles 150
6.4.2. Characterization of TFC and TFN membranes 153
6.4.3. Performance evaluation of TFC and TFN membranes 157
6.5. Conclusions 159
6.6. Supporting Information 164
7. Conclusions 166
7.1. Conclusions 167
7.2. Recommendations 169

List of Tables

Table 2-1 Commercially available RO membranes and modules (Chian et al. 2007). Reproduced with permission of Humana Press..... 19
Table 3-1 (a) TFC-RO membrane fabrication parameters, codes and actual levels as used in the full factorial design, (b) experimental design matrix, response values and factor levels for each run in the factorial design. 62
Table 3-2 Analysis of variance of the 2FI regression model for water flux and salt rejection. 62
Table 3-3 (a) Analysis of variance of the reduced 2FI regression model for water flux and salt rejection (b) Statistics used to investigate the goodness of fit for the reduced water flux and salt rejection models. 64
Table 4-1 XPS results for SN50 with different surface functionalities. 90
Table 4-2 XPS results for TFC membrane and TFN membranes incorporated with different surface functionalized SN50. 95
Tab 5-1 XPS results for HMSN, TFC and 0.05 wt % HMSN incorporated TFN membrane. 127
Table 6-1 Hydrodynamic sizes and zeta potentials of SN, SN-NH_2 and SN-PEI. 151
Table 6-2 XPS analysis for SN, SN-NH_2 and SN-PEI. 153
Table 6-3 XPS analysis for SN-PEI, TFC and the TFN membrane with 0.05 wt % SN-PEI. 157

List of Figures

Figure 2-1 Schematic view of normal osmosis and reverse osmosis processes. 12
Figure 2-2 The classification of polymeric membranes (Ren & Wang, 2011). Reproduced with permission of Springer 14
Figure 2-3 Schematic of the TFC-RO membranes and the chemical structure of the aromatic polyamide. 16
Figure 2-4 Schematic diagram of a Spiral wound RO Module (Ettouney & Wilf 2009). Reproduced with permission of Springer 18
Figure 2-5 The schematic diagram of hollow fibre membrane (Chen et al., 2011). Reproduced with permission of Springer 19
Figure 2-6 The schematic diagram of membranes for solution diffusion mechanism. 21
Figure 2-7 Schematic view of the membrane pore for pore flow models 24
Figure 2-8 The schematic view of RO process. 26
Figure 2-9 The schematic view of concentration polarization profile in a cross flow membrane system. 31
Figure 2-10 Conceptual illustrations of antifouling mechanisms: (a) steric repulsion; (b) formation of a water layer; (c) electrostatic repulsion (Kang &Cao, 2012). Reproduced with permission of Elsevier 33
Figure 3-1 Schematic illustration of the two-stage casting strategy to fabricate TFC-RO membranes (a) phase inversion process to fabricate PSF supporting interlayer; (b) Interfacial polymerization to synthesize the polyamide selective barrier layer including schematic of the final TFC-RO membranes. 58
Figure 3-2 Pareto charts for the effect of various parameters on (a) water flux; (b) salt rejection (A: PSF concentration, B: MPD soaking time, and C: heat curing time). 63
Figure 3-3 Actual vs. predicted values of the responses by the regression models: (a) water flux; (b) salt rejection. 66
Figure 3-4 Response surface plots of water flux and salt rejection as a function of: (a, b) PSF concentration (A) and MPD soaking time (B) at a fixed heat curing time of 15 min; (c, d) MPD soaking time (B) and heat curing time (C) at a fixed MPD soaking time of 6 min. 66
Figure 3-5 SEM micrographs displaying the cross-section (left) and bottom (right) of PSF support layers cast using different concentrations of PSF: (a,b) 9 %; (c,d) 12 %; (e,f) 15 %. 68
Figure 4-1 micrographs and TEM images (inset) of the different sized SN, A) SN50, B) SN100, C) SN50-NH_2, D) SN100-NH_2, E) SN50-EPX and F) SN100-EPX. Particle size and morphology are similar as the SN before modification. 89
Figure 4-2 A) TGA thermograms for SN50 before and after surface functionalization, B) FTIR spectra for PES support, TFC membrane and a typical SN-TFC membrane. 91
Figure 4-3 SEM micrographs of the surfaces and cross-section of different TFC/SN-TFC membranes: A) TFC, B) SN50-TFC, C) SN50-NH_2-TFC, D) SN50-EPX-TFC, E) SN100-TFC, F) SN100-NH_2-TFC, G) SN100-EPX-TFC. For the surface images, the low magnification images were taken at 55000x and the high magnification images were taken at 200000x and for the cross-section images, the low magnification images were at 2000x and the high magnification ones were at 25000x. 92

Figure 4-4 Cross-section TEM images of the A) TFC, B) SN50-TFC, C) SN50-NH_2-TFC and SN50-EPX-TFC membranes; the scale bars are 100 nm. 94
Figure 4-5 A) Comparison on the streaming potential measurements for the TFC membranes with and without SN50-NH_2, B) Contact angles for the TFC membranes incorporated with different concentrations of SN50 and 0.05 wt% SN-NH_2 and SN-EPX, C) Performance evaluation for various TFC membranes incorporated with different concentrations of SN50. 97
Figure 4-6 A) Desalination performance evaluation for the TFC membranes incorporated with various SN with different surface functionalities, B) Normalized salt rejection for the fabricated SN-TFC membranes vs. filtration time. 100
Figure 5-1 The schematic illustration of the HMSN fabrication strategy. The CTAB and PtBA templates can be removed simultaneously through ion exchange and dissolution. ... 123
Figure 5-2 A) FTIR spectra for the CTAB and PtAB templates, HMSN-b and HMSN B) TGA thermograms for CTAB and PtBA templates, HMSN-b and HMSN. 125
Figure 5-3 High and low magnification A) TEM and B) SEM images of the HMSN. The hollow mesoporous structure of HMSN can be clearly seen from the high resolution TEM image.Scale bars for the TEM images are 100 nm and 50 nm (inset) and for the SEM images are 1 µm and 200 nm (inset). 125
Figure 5-4 Nitrogen adsorption/ desorption isotherms for the fabricated HMSN; the inset is the pore size distribution obtained from the BJH method. 126
Figure 5-5 Low and high magnification SEM surface (top) and cross-section (bottom) images of the synthesized TFC membrane and TFN membranes incorporated with different concentrations of HMSN: A) TFC, B) TFN, 0.01 wt %, C) TFN, 0.03 wt %, D) TFN, 0.05 wt % and E) TFN, 0.1 wt %. For the surface images, the magnifications are 25000x and 120000x, and for the cross-section images, the magnifications are 2000x and 50000x. 127
Figure 5-6 Images taken from a typical TFN membrane incorporated with 0.05 wt % HMSN A) tilted surface images from cross-section SEM sample, and B) cross-section TEM images. For the SEM images, the scale bars are 4 µm and 500 nm, and for the TEM images the scale bars are 200 nm and 50 nm. 128
Figure 5-7 Comparison on the contact angles of various fabricated TFC/TFN membranes as a function of HMSN loading. Contact angle of the TFN membrane incorporated with 0.05 % HMSN-b is also included for comparision. The reported contact angles are the average of at least 8 different positions on each membrane. 129
Figure 5-8 The performance evaluations of the fabricated TFC/TFN membranes in terms of water flux and salt rejection as a function of HMSN loading. The performance of the TFN membrane with 0.05 wt % HMSN-b is also shown for comparison. 130
Figure 5-9 The water flux of the fabricated TFC and TFN membranes versus compaction time against DI water at 1.5 MPa and 25 ± 0.1 ºC. 132
Figure 6-1 The schematic description of the general strategy to fabricate SN-PEI. 150
Figure 6-2 TGA thermograms for: a) SN, b) SN-NH_2, and c) SN-PEI. 152
Figure 6-3 SEM images, TEM images (inset), and EDX spectra for A) SN, and B) SN-PEI. The scale bars are 200 nm for TEM images and 5 µm for SEM images. 152
Figure 6-4 High and low magnification SEM surface images of the fabricated membranes: A) control TFC, B) TFN incorporated with 0.03 wt % SN-PEI C) TFN incorporated with 0.05 wt % SN-PEI, and D) TFN incorporated with 0.1 wt % SN-PEI. 154

Figure 6-5 A) SEM cross-section image, B) surface SEM image obtained from the tilted cross-section SEM sample, and C) EDX spectra obtained through EDX mapping for the control TFC membrane; and D) SEM cross-section image, E) surface SEM image obtained from the tilted cross-section SEM sample, and F) EDX spectra obtained through EDX mapping for the TFN membrane incorporated with 0.1 wt % SN-PEI. 155
Figure 6-6 The comparison of the contact angles of various fabricated TFC and TFN membranes. 156
Figure 6-7 Performance evaluation for the fabricated TFC/TFN membranes in terms of water flux and salt rejection as a function of SN-PEI loading. 157
Figure 6-8 The water flux of the fabricated TFC and TFN membranes versus compaction time at 1.5 MPa and 25±0.1 ºC. 158

Chapter 1

Introduction

1.1. Background and project objectives

Water is a crucial source for different aspects of human life. The scarcity of fresh water resources and the need for additional water supplies are critical in many arid regions of the world. This issue will be more important in the future due to the increase in world's population and decrease in fresh water resources. In this respect, the importance of desalination as a general strategy to convert salt water to fresh water is more discernible [1]. To date, the reverse osmosis (RO) process via polymeric thin film composite (TFC) membranes is considered as the most widely used technology for desalination. The main advantages of these membranes are their higher separation performance and stability over a wider range of temperature and pH compared with the traditionally used cellulose acetate membranes [2]. However, high capital and operating costs due to fouling and chlorine attack, and high energy consumption due to the low permeability of these membranes are the main challenges for their industrial applications. Therefore, several attempts have been made during the past decades to improve the physicochemical properties and separation performance of TFC membranes. However, there is still an on-going need to develop technically and economically feasible TFC membranes, with improved separation capability and efficiency, and reduced costs for various industrial and municipal applications [3, 4].

The development of nanotechnology has opened new frontiers in the advancement of TFC membranes. The incorporation of nanomaterials into the thin film polyamide (PA) layer of TFC membranes, making a structure known as thin film nanocomposite (TFN) membrane, can offer the advantages of both inorganic nanofillers and organic polymeric membranes. However, the possibility of nanoparticles' leakage and their low compatibility with organic membranes make the successful fabrication of TFN membranes challenging. Hence, investigating the structure-performance correlation of TFC/TFN membranes and their interactions with the introduced nanomaterials is of great importance. Till now, there are very few studies reporting on understanding the influence of in-situ introduction of nanomaterials on the chemistry of the fabricated TFN membranes which have mainly focused on one type of interaction [5-7]. Further, extensive identification of

physicochemical properties of TFN membranes after introducing nanoparticles with different sizes and surface modifications and correlation of them with the TFN membranes' performance are missing. Moreover, the integration of novel structures of nanomaterials with the TFC membranes can be worthy of investigation to guide the development of nanoparticle-enabled multifunctional membranes.

Silica nanoparticles (SN) have good biocompatibility, thermal and mechanical stability and can be easily surface functionalized [8, 9]. Importantly, SN show hydrophilic characteristic due to their abundant surface hydroxyl groups which can be beneficial for the permeability enhancement and fouling mitigation after being introduced into TFC membranes [10, 11]. In addition, SN as an inexpensive material can produce potentially commercially viable membranes. Therefore, SN has been chosen as a typical nanofiller to develop novel functional TFN membranes throughout this PhD project. Here, SN with different sizes, surface functionalities and structures have been synthesized and incorporated into the PA layer of TFC membranes. The physicochemical properties of the fabricated SN and TFC/TFN membranes and the desalination performance of the resulting membranes in terms of water flux and salt rejection have been extensively evaluated. The final goal is to advance the knowledge of interfacial interactions between inorganic nanomaterials and the thin film PA layer of TFC membranes.

The specific objectives of this PhD project include:

- To investigate the structure-performance correlation of TFC membranes considering their fabrication parameters.
- To synthesize and characterize a range of silica nanoparticles with various sizes, surface functionalities and structures and apply them as the nanofillers for TFC membranes.
- To identify the contribution of hollow mesoporous silica nanoparticles (HMSN) to the desalination performance of the TFN membranes being developed.
- To study the role of the polymer surface modification of inorganic nanofillers in the desalination performance and nanocomposite structure of the resulting TFN membranes.

- To expand the knowledge of the interfacial interactions between inorganic nanomaterials and the thin PA layer of TFC membranes.

1.2. Thesis Outline

This thesis is written in a publication-based format. It starts with an introduction and background for this research followed by the review of recent contributions to the field. The major experimental results are presented in four journal papers (under review) which are presented as Chapters 3 to 6, where the title of each chapter reflects the title of the submitted/ ready to submit paper.

The thesis structure is summarized as follows:

Chapter 1 contains a brief background and introduction for this work and highlights the key objectives. The structure of the thesis body and the motivation behind each of the following chapters are also briefed in this chapter.

Chapter 2 presents a background and literature review on the development of TFC membranes in RO process. This chapter provides an overview on the TFC membrane materials, module configurations and transport mechanisms of the RO membranes. Here, we summarize the key parameters in terms of TFC membrane characteristics and operation conditions, and technical and economic challenges in the application of RO processes such as fouling and concentration polarization. The RO process in dairy industry is elaborated as an example for the application of RO membranes in the fields other than desalination. Finally, the prospects for the development of RO materials and technologies and the importance of TFN development are briefed. The literature study presented in this part has been published as a book chapter by Wiley-Blackwell in July 2015.

Chapter 3 is based on the optimisation of some TFC membrane fabrication parameters. Microporous supports and PA layers of TFC membranes have been fabricated and the effect of some fabrication parameters, which are widely varied in the literature, on the water flux and salt rejection of TFC membranes is

systematically evaluated. Statistical analysis is used throughout this section to identify the interaction of selected parameters and investigate their significance. The outcomes from this chapter have guided us on the selection of fabrication parameters used for the following stages of the study. This chapter is presented as a journal paper, which has been submitted to Industrial & Engineering Chemistry Research (IE-2105-019756).

Chapter 4 proposes TFN membranes incorporated with differently sized and surface functionalized silica nanoparticles to get a better understanding on the interfacial interactions between nanoparticles and TFC membranes. The successful synthesis and functionalization of nanoparticles and TFN membranes is extensively characterized in this chapter. Furthermore, the influence of surface functionality of nanoparticles (hydroxyl, amine and epoxy) on the desalination performance and physicochemical properties of the developed TFN membranes is studied. The Chapter 4 is written as a journal paper, which has been submitted to the Journal of Membrane Science (JMS-15-1287).

Chapter 5 proceeds the extensive study of solid SN incorporated TFC membranes by exploring the novel application of hollow mesoporous silica nanoparticles (HMSN) as the nanofiller for the PA layer of TFC membranes. Highly dispersible HMSN with the average particle size of ~ 68 nm are synthesized through several stages including emulsion polymerization of PTBA for the core template, hydrothermal synthesis for the silica shell formation and solvent extraction for the simultaneous templates' removal from the nanoparticles. The influence of HMSN loading concentration on the structure and performance of resulting TFN membranes have been studied in detail. This Chapter is presented as a journal paper, which has been submitted to the ACS Applied Materials & Interfaces (am-2015-094259).

Chapter 6 follows the exploration of different surface functionality of SN by developing a novel TFN membrane hybridized with polyethyleneimide (PEI) modified silica nanoparticles. The main focus is to identify the influence of PEI modification on the performance and properties of the resulting TFN membranes. PEI is deemed to enhance surface hydrophilicity of TFN membranes and as a result

improve their water permeability. In addition, PEI modification is chosen to enhance the compatibility of inorganic nanofillers with the organic PA layer of TFC membranes. The resulting TFN membranes display higher water flux and salt rejection compared with the membranes without nanoparticles. The Chapter 6 is prepared in publication format and will be submitted soon.

Chapter 7 concludes the key research findings and technical data, which are summarised from Chapters 3-6. Concise recommendations for advancing the outcomes of the current study and further studies have also been presented in this chapter.

References

[1] M.A. Rayan, B. Djebedjian, I. Khaled, Evaluation of the effectiveness and performance of desalination equipment in Egypt, 2004.

[2] L.Y. Ng, A.W. Mohammad, C.P. Leo, N. Hilal, Polymeric membranes incorporated with metal/metal oxide nanoparticles: A comprehensive review, Desalination 308 (2013) 15-33.

[3] K.P. Lee, T.C. Arnot, D. Mattia, A review of reverse osmosis membrane materials for desalination- Development to date and future potential, Journal of Membrane Science 370 (2011) 1-22.

[4] M. Elimelech, W.A. Phillip, The Future of Seawater Desalination: Energy, Technology, and the Environment, Science 333 (2011) 712-717.

[5] Emadzadeh, D., et al., Synthesis, modification and optimization of titanate nanotubes-polyamide thin film nanocomposite (TFN) membrane for forward osmosis (FO) application. Chemical Engineering Journal, 2015. 281: p. 243-251.

[6] Lind, M.L., et al., Influence of Zeolite Crystal Size on Zeolite-Polyamide Thin Film Nanocomposite Membranes. Langmuir, 2009. 25(17): p. 10139-10145.

[7] Kim, S.G., et al., Nanocomposite poly(arylene ether sulfone) reverse osmosis membrane containing functional zeolite nanoparticles for seawater desalination. Journal of Membrane Science, 2013. 443: p. 10-18.

[8] L. Jin, W. Shi, S. Yu, X. Yi, N. Sun, C. Ma, Y. Liu, Preparation and characterization of a novel PA-SiO_2 nanofiltration membrane for raw water treatment, Desalination 298 (2012) 34-41.

[9] H. Yamada, C. Urata, Y. Aoyama, S. Osada, Y. Yamauchi, K. Kuroda, Preparation of Colloidal Mesoporous Silica Nanoparticles with Different Diameters and Their Unique Degradation Behavior in Static Aqueous Systems, Chemistry of Materials 24 (2012) 1462-1471.

[10] G.d. Kang, Y.m. Cao, Development of antifouling reverse osmosis membranes for water treatment: A review, Water Research 46 (2012) 584-600.

[11] G.L. Jadav, P.S. Singh, Synthesis of novel silica-polyamide nanocomposite membrane with enhanced properties, Journal of Membrane Science 328 (2009) 257-267.

Chapter 2

Statement of Authorship

Title of Paper	Development and application of reverse osmosis for separation
Publication Status	☑ Published ☐ Accepted for Publication ☐ Submitted for Publication ☐ Unpublished and Unsubmitted work written in manuscript style
Publication Details	Masoumeh Zargar, and Sheng Dai, in Membrane Processing for Dairy Ingredient Separation, ed. J. D. Kang Hu, Wiley-Blackwell, 2015, ch. Development and application of reverse osmosis for separation p. 139. (ISBN: 978-1-118-59017-1)

Principal Author

Name of Principal Author (Candidate)	Masoumeh Zargar		
Contribution to the Paper	Performing the literature review and writing the manuscript.		
Certification:	This paper reports on original research I conducted during the period of my Higher Degree by Research candidature and is not subject to any obligations or contractual agreements with a third party that would constrain its inclusion in this thesis. I am the primary author of this paper.		
Signature		Date	22/09/2015

Co-Author Contributions

By signing the Statement of Authorship, each author certifies that their stated contribution to the publication is accurate and that permission is granted for the publication to be included in the candidate's thesis.

Name of Co-Author	Bo Jin		
Contribution to the Paper	Supervising the development of the work, assisting in the manuscript review and assessment.		
Signature		Date	22/09/2015

Name of Co-Author	Sheng Dai		
Contribution to the Paper	Supervising the development of the work, assisting in the manuscript review and assessment.		
Signature		Date	22/09/2015

Zargar, M., Jin, B. & Dai, S. (2015). Development and application of reverse osmosis for separation. In J. Dickson & K. Hu (Eds.), *Membrane Processing for Dairy Ingredient Separation* (Ch. 6, pp. 139-175). Wiley-Blackwell.

Chapter 3

Statement of Authorship

Title of Paper	An integrated statistic and systematic approach to determine synthesis-performance correlation of thin film composite reverse osmosis membranes
Publication Status	☐ Published ☐ Accepted for Publication ☑ Submitted for Publication ☐ Unpublished and Unsubmitted work written in manuscript style
Publication Details	Masoumeh Zargar, Bo Jin*, Sheng Dai*, An integrated statistic and systematic approach to determine synthesis-performance correlation of thin film composite reverse osmosis membranes, Submitted to Industrial & Engineering Chemistry Research (IE-2105-019756).

Principal Author

Name of Principal Author (Candidate)	Masoumeh Zargar		
Contribution to the Paper	Designing and performing the experiments, analysis of the results and writing the manuscript		
Certification:	This paper reports on original research I conducted during the period of my Higher Degree by Research candidature and is not subject to any obligations or contractual agreements with a third party that would constrain its inclusion in this thesis. I am the primary author of this paper.		
Signature		Date	22/09/2015

Co-Author Contributions

By signing the Statement of Authorship, each author certifies that their stated contribution to the publication is accurate and that permission is granted for the publication to be included in the candidate's thesis.

Name of Co-Author	Bo Jin		
Contribution to the Paper	Supervising the development of the work, assisting in the manuscript review and assessment.		
Signature		Date	22/9/2015

Name of Co-Author	Sheng Dai		
Contribution to the Paper	Supervising the development of the work, assisting in the data interpretation, manuscript review and assessment.		
Signature		Date	22/9/2015

An Integrated Statistic and Systematic Approach to Study the Structure-Performance Correlation of Thin Film Composite Reverse Osmosis Membranes for Desalination

Masoumeh Zargar, Bo Jin*, Sheng Dai*

School of Chemical Engineering, the University of Adelaide, Adelaide, SA, 5005, Australia

*Corresponding authors

Email: bo.jin@adelaide.edu.au; s.dai@adelaide.edu.au

Submitted to Industrial & Engineering chemistry Research (IE-2105-019756)

3.1. Abstract

Thin film composite reverse osmosis (TFC-RO) membranes are the most commonly used polymeric membranes in desalination process. The membrane properties and performance are dominated by many fabrication parameters, including chemistry of polymer monomers and synthesis conditions. The interactions within these parameters make membrane fabrication complex. Our study revealed that the integration of statistic method with systematic approach could facilitate the understanding of synthesis-performance correlations for the fabrication of TFC-RO membranes able to demonstrate improved desalination performance. In this study, the influence of three major fabrication parameters: polysulfone concentration, aqueous phase soaking time and heat curing time on the overall desalination performance of the resulting TFC-RO membranes was systematically evaluated. Experimental results were statistically validated using analysis of variance (ANOVA). Two mathematical models for water flux and salt rejection were developed based on the statistical data validation. The most influential correlations were identified as the polysulfone concentration on water flux and the aqueous phase soaking time on salt rejection. Interaction of soaking time with the other two parameters was also found to be significant on salt rejection. Our findings highlighted the importance of considering interactions when devising a strategy to fabricate TFC-RO membranes in order to optimize the overall desalination performance.

***Keywords*:** Thin-film composite membranes; Desalination; Reverse osmosis; Statistic analysis; Interfacial polymerization.

3.2. Introduction

Development of thin film composite (TFC) membranes is the most significant achievement in the advancement of reverse osmosis (RO) technology using polymeric membranes. The first TFC membrane was prepared by Caddot and his co-workers in the late 1970s through the in-situ polycondensation on porous polysulfone support. That membrane was a replacement for single layer asymmetric RO membranes synthesized via phase inversion of cellulose acetate [1-3]. The TFC-RO membranes have promising advantages in terms of desalination performance, such as greater water flux, high salt/organic rejection, excellent operation stability in a wide range of temperature (0 - 45C°) and pH (1 - 11), and more resistance to compaction and attack by biological agents compared with traditional cellulose acetate membranes [4-6]. Therefore, the development of these membranes has attracted plenty of research attention over the past decades. Typically, TFC-RO membranes consist of three layers: (1) a woven or nonwoven fabric layer on the bottom acting as the mechanical support to withstand high pressure operation; (2) a microporous support membrane which is directly cast on the fabric through phase inversion process; and (3) an ultrathin selective barrier layer laminated on the denser side of the microporous support by interfacial polymerization [7]. Nowadays, the most commonly used materials for the microporous support membrane and selective barrier layer in the TFC-RO membranes are polysulfone (PSF) and cross-linked polyamide (PA) respectively [8]. The key factors influencing the phase inversion process associated with TFC-RO membranes' fabrication are casting solution concentration and composition, coagulation bath composition, operating conditions (temperature, humidity, etc.), and casting operations such as casting speed, film thickness and fabric pre-treatment. For the interfacial polymerization of selective barrier layer, the most important parameters include the type and concentration of monomers, additives, organic solvents, soaking and reaction times, curing time and temperature and washing strategies [9, 10]. Overall performance of the TFC-RO membranes could be improved progressively through manipulation of fabrication parameters and optimization of physiochemical characteristics of individual layers in terms of their resistance, efficiency and formation [6, 11]. Since the structures and properties of the microporous support have significant influence on the formation

and characteristics of PA selective barrier layer [8, 12-14], the final optimization strategy should consider these fabrication stages simultaneously to ensure the best performance of fabricated TFC-RO membranes is achieved.

To date, there are many studies on identifying key fabrication parameters and their impact on final RO membrane performance some of which are [8, 9, 15-28]. Compared with the large number of studies focusing on the influence of one factor at a time, few reports could be found systematically studying the interaction of parameters. For instance, some studies have been performed to investigate the effect of microporous support structure and chemistry on the performance of TFC membranes [8, 13, 26]. They found that the support layer characteristics have profound influence on the performance of the final TFC-RO membranes. However, the interaction of fabrication parameters of PA selective layer with different support structures has not been considered in these works. Many other reports documented the correlation between the RO performances of the TFC membranes and curing time associated with interfacial polymerization, and suggested that curing time has significant influence on TFC membrane performance [9, 15, 16]. However, again only one-on-one correlations were developed by them. Another parameter which is believed to be important for the TFC-RO membrane properties and performance is the aqueous phase soaking time. It is believed that these above parameters should have interactions, which can also significantly affect the membrane's overall performance. Hence, it is crucial to understand the interrelation of these parameters to ensure high quality and performance of resulting TFC-RO membranes is achieved. Furthermore, the desalination performance of the TFC-RO membranes is always required to be evaluated by two conflicting parameters: water flux and salt rejection. Generally, a TFC-RO membrane with higher water flux could perform a lower salt rejection rate, and vice versa. Therefore, it is important to use statistical methods to identify the best fabrication conditions for optimized separation performance.

To elucidate relationships among these key TFC membrane fabrication parameters, a systematic study using statistical analysis together with Design Expert software has been performed in this study. To the best of our knowledge, no study has been carried out to understand how the aqueous phase soaking time influences on the membrane performance considering the variations in curing time and support layer

porosity. Herein, PSF concentration in the phase inversion process and aqueous phase soaking time and heat curing time in the interfacial polymerization course are chosen as the independent variables. TFC-RO membranes are fabricated following a two-step casting method by fixing fabrication parameters other than the selected independent parameters at the most common or optimum reported values. The obtained membranes have been evaluated using a cross-flow filtration unit to investigate the RO membranes' structure and performance properties. Full factorial design has been selected to design the experiments and statistical methods have been used to establish these fabrication parameters correlations as mathematical models. The research outcomes will provide better insight into the interrelationship among these parameters, which can be beneficial for simultaneously optimizing synthesis stages of the TFC-RO membranes and their desalination performance in terms of water flux and salt rejection.

3.3. Materials and Methods

3.3.1. Materials

Commercial polyester non-woven fabric (100 µm) was kindly supplied by PURUIXIN-TOP-SCIENCE and used as the backing layer for PSF interlayer. PSF (Udel P-1700 CL2611 CMP, (Mw≅45000)) was provided by Solvay Speciality Polymers and used to fabricate PSF support interlayer. N, N-dimethylformamide (DMF, anhydrous, 99.8%, Merck) was used as the solvent to dissolve PSF. An adjustable casting knife (Elcometer 3530/2, Elcometer, UK) was used for casting PSF support layer on glass surface. For the establishment of PA selective layer on the PSF support, 1, 3-phenylenediamine (MPD, >99%), 1, 3, 5-benzenetricarbonyl trichloride (TMC, 98%), and n-Hexane were purchased from Sigma Aldrich. Sodium chloride (NaCl) was purchased from VWR International.

3.3.2. TFC-RO membrane fabrication

The TFC-RO membranes were synthesized through a two-stage casting method following a full-factorial design. For the support layer, PSF membrane was made through phase inversion process at different PSF concentrations (9-15 % (w/w)). Typically, PSF beads were dried at 60 °C overnight and added to DMF. The mixture was stirred at room temperature to form a clear homogenous solution and then

degassed in an ultrasonication bath equipped with degassing function for 3 h. Subsequently, the non-woven fabric was placed on a clean glass plate and wetted with degassed DMF. Excessive solvent was removed by a soft rubber roller on the surface of fabric followed by tapping fabric to glass plate. After that, the above-prepared PSF solution was casted on the polyester fabric using an adjustable casting knife with a fixed height at 200 µm. The glass plate was then immediately immersed in a precipitation bath containing distilled water and 2 % DMF at 22 °C to initiate phase inversion process. The precipitated PSF supports were allowed to stay in the bath for at least 10 min to ensure complete phase separation and then washed thoroughly with distilled water and stored in distilled water at 5 °C for further experiments. In order to fabricate the PA selective barrier layer of TFC-RO membranes, the synthesised PSF support was clamped between an acrylic plastic plate, a rubber gasket and an acrylic plastic frame on the top of that. Then, 2 % (w/v) MPD aqueous solution was poured inside the frame and allowed to soak for 2-10 min. After lapsing the designated MPD soaking time, excess MPD solution was drained and the assembly was air-dried for around 1 min, followed by disassembling and tightly rolling the PSF support with a soft rubber roller until no visible droplets were remained on surface of the support. The plate-gasket-frame disassembly/ rolling/ reassembly period was fixed at 2.5-3 min in all experiments. Following to that, 0.1 % (w/v) TMC in n-hexane solution was poured into the frame and allowed to react with the adsorbed MPD for 1 min resulting in the formation of an ultra-thin PA selective layer over the surface of PSF support. Then, excess organic phase was drained and the membrane was air-dried for 30 s followed by two washing stages with 0.2 % (w/v) Na_2CO_3 aqueous solution and subsequently distilled water, each for 30 s. The whole assembly was then moved to a recirculating oven set at 60 °C for further polymerization/curing for different residence time (10-20 min). After curing in oven, the fabricated TFC-RO membranes were washed with 22 °C distilled water and stored in distilled water at 5 °C for further characterization and evaluation. The schematic illustration of the two-stage casting procedure to fabricate PSF support and PA selective barrier layer of TFC-RO membranes is presented in Fig 3-1.

a)

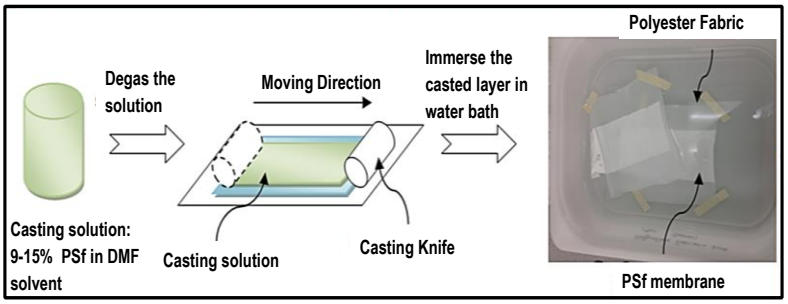

b)

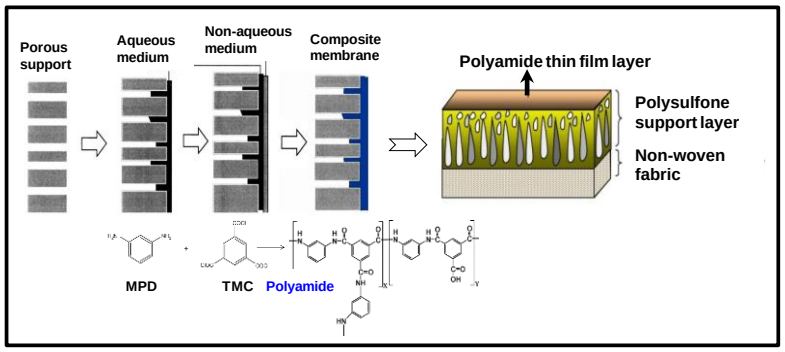

Figure 3-1 Schematic illustration of the two-stage casting strategy to fabricate TFC-RO membranes (a) phase inversion process to fabricate PSF supporting interlayer; (b) Interfacial polymerization to synthesize the polyamide selective barrier layer including schematic of the final TFC-RO membranes.

3.3.3. Membrane Characterization

The cross-section and bottom morphologies of fabricated TFC-RO membranes were characterized using a scanning electron microscopy (FEI Quanta 450 FEG Environmental SEM (ESEM)) with a voltage of 5-20 kV and working distance of 10 mm. Membrane samples were prepared by freeze fracturing of wet membranes in liquid nitrogen. The prepared samples were dried overnight and sputter coated with ~5 nm layer of platinum using CRESSINGTON 208 high-resolution sputter coater machine. Attenuated total reflectance Fourier transform infrared spectroscopy (ATR-FTIR) was performed using a NICOLET 6700 spectrometer equipped with a diamond ATR and the data were subsequently used to evaluate chemical structures of fabricated TFC-RO membranes.

3.3.4. Membrane performance evaluation

A high-pressure cross-flow filtration setup was established to evaluate performance of the fabricated TFC-RO membranes. The effective membrane area of the filtration cell (CF042, Sterlitech) was 42 cm^2. In order to control pressure creep in the system, a pressure relief valve was included on the feed entry line to the membrane cell.

Before each test, membrane coupons were compacted with distilled water in the system for at least 16 h at 1.5 MPa to reach equilibrium flux; they were then tested with 15 L of 2000 mg/L NaCl solution. The operating conditions were controlled at 1.5 MPa and 25 ± 1 °C, and the concentrate flow rate was fixed at 4 L/min. During the experiments, the concentrate flow was recycled back to the feed tank and permeate was collected in a container positioned on a digital balance for flux measurement. The schematic illustration of the assembled filtration setup is presented in supporting information (Fig 3S-1). The weight of the collected permeate was recorded using a LabX Direct Software (Mettler Toledo) and flux (J) was calculated based on the collected permeate at different time intervals using Equation 1. In order to evaluate the salt rejection performance of each TFC-RO membrane, the conductivity of permeate and feed water were measured using a conductometer (AQUA, Cond./ pH, TPS, Australia). Conductivities were subsequently converted to their equivalent salt concentrations using a pre-calibration curve shown in supporting information (Fig 3S-2). Salt rejection (R %) could then be calculated through Equation 2.

$$J = \frac{V_P}{\mathrm{A.t}} \quad (1)$$

$$R\% = \left(1 - \frac{C_P}{C_F}\right) \times 100 \quad (2)$$

where J is the permeate water flux (LMH), V_P is the collected permeate volume (L), A is the active membrane surface area (m^2), t is the operation time (h), R is the salt rejection and C_P and C_F are the equivalent NaCl concentrations in collected permeate and feed water, respectively.

3.4. Results and Discussion

3.4.1. Design of experiments and statistical analysis

To identify key parameters and their optimum conditions for TFC-RO membrane fabrication, enormous experiments need to be carried out throughout the multiple-step synthesis process. However, the experimental outcomes could be inconclusive due to the possible interactions of these parameters. Using the design of experiments (DOE) technique can optimize the response values through a few experiments involving several factors at a time. DOE can simplify experimental operation and

data analysis, and importantly provides a better understanding of the interrelationships among studied parameters [29]. The main step to the DOE is the selection of response values, independent factors and their levels. Several parameters are involved in TFC-RO membrane fabrication procedure making it difficult, even via statistical tools, to perform a comprehensive study considering all factors at the same time. This is why most studies have focused on a selected group of parameters rather than a wide range of variables and levels [23, 24, 27, 28]. Each of these studies could be helpful to understand the influence of some fabrication parameters and finally correlate them to the TFC membranes performance. In this study, considering the possible correlations of the membrane synthesis conditions in fabrication process and the non-studied correlations in previous reported studies, three key parameters including PSF support concentration, MPD soaking time and heat curing time were chosen as independent variables to understand their interrelationship influence on the overall desalination performance of TFC-RO membranes. The outcomes can provide further insights to enhance the understanding of the scientific community. A two-level full factorial design, which not only evaluates the effect of individual parameters and their relative importance but also the interactional influence of two or more variables, has been established to determine the correlation. Each experiment has been performed at least three times and the results have been averaged. In order to find out the curvature that may exist in the model and experimental error, three replicates at the centre point were also conducted. Student *t*-test and ANOVA were applied to calculate the significance of each independent parameter and the interactions on the variation of main response: water flux and salt rejection. The principles for selection of the studied parameters' levels and the values chosen for the fixed fabrication parameters are discussed herein.

Different concentrations (9-15 %) of PSF casting solutions were applied for support layer fabrication. The concentration range was selected based on the known morphology change of the support layer from a finger-like structure to a sponge-like structure by concentration increment. The clamping strategy to perform interfacial polymerization was used because of its reported optimum performance results [9, 30] and the concentrations chosen for MPD and TMC were based on the values giving high performance in previous studies considering these parameters [9, 18, 19]. The aqueous phase soaking time was tested between 2 and 10 min, which were the most

commonly reported soaking time limits in the literature [13, 30]. Regarding the curing parameters, Ghosh et al. reported that for hexane, which is one of the most popular organic solvents for PA fabrication, 60 °C was the best heat curing temperature at a 10 min curing time [16]. In addition, Zhang et al. reported on the suitability of curing up to 20 min at 60 °C in their experiments with hexane as the solvent [9]. Therefore, hexane was chosen as the organic solvent, 60 °C was selected as the curing temperature, and 10 and 20 min were chosen as the selected levels for the curing time.

Taking into account of the centre point, each factor has been designed at three levels (+1, 0, -1) as shown in Table 3-1a. The key factors along with the experimental matrix design, specifying the experimental conditions for each run, and the real and coded values for each level are shown in Table 3-1b. Water flux and salt rejection values for each desalination evaluation using the fabricated TFC-RO membranes are also illustrated in Table 3-1b. The experimental results showed that the water flux varied between around 23 to 47 LMH, while the salt rejection varied between around 80 to 94% for the fabricated membranes. The FTIR spectra of the fabricated TFC-RO membranes with their PSF interlayer support are illustrated in Fig 3S-3.

As indicated in Table 3-1a, X_1, X_2 and X_3 are the coded values for the selected independent parameters, representing PSF concentration (A), MPD soaking time (B) and heat curing time (C). Y_1 and Y_2 are the coded values for the responses: water flux and salt rejection. Following regression analysis of the 2^3 full factorial design, regression coefficients (β), which represent the main and interaction effect of independent variables on the response values, can be obtained. While Y_i shows the general term for the response, the statistical model for this design can be described by Equation 3 [29]:

$$Y_i = \beta_0 + \beta_1 X_1 + \beta_2 X_2 + \beta_3 X_3 + \beta_{12} X_1 X_2 + \beta_{13} X_1 X_3 + \beta_{23} X_2 X_3 + \beta_{123} X_1 X_2 X_3 \quad (3)$$

where β_0 is the intercept of the regression line, β_1, β_2 and β_3 imply the effect of concentration, MPD soaking time and curing time, respectively. β_{12}, β_{13} and β_{23} show the interacting effect of PSF concentration-MPD soaking time, PSF concentration-curing time and MPD soaking time-curing time, respectively. β_{123} is the interaction of all three parameters.

Table 3-1 (a) TFC-RO membrane fabrication parameters, codes and actual levels as used in the full factorial design, (b) experimental design matrix, response values and factor levels for each run in the factorial design.

(a)

Factor	Code	Real values of the levels		
		-1	0	+1
(A) PSF concentration in casting solution (%(w/w))	X_1	9	12	15
(B) MPD soaking time (min)	X_2	2	6	10
(C) Curing time (min)	X_3	10	15	20

(b)

Runs	Level of Factors (High: +1; Centre:0 ; Low:-1) (Coded)			Input Variables (Actual)			Responses	
	X_1	X_2	X_3	A	B	C	Y_1-Flux (LMH)	Y_2-Salt rejection (%)
TFC1	-1	-1	-1	9	2	10	47.3	90.7
TFC2	+1	-1	-1	15	2	10	30.31	84.3
TFC3	-1	-1	+1	9	2	20	40.11	84.63
TFC4	+1	-1	+1	15	2	20	24.53	80.11
TFC5	-1	+1	-1	9	10	10	40.01	89.96
TFC6	+1	+1	-1	15	10	10	27.91	91.89
TFC7	-1	+1	+1	9	10	20	37.72	93.7
TFC8	+1	+1	+1	15	10	20	23.33	94.13
TFC9	0	0	0	12	6	15	41.8	90.7
TFC10	0	0	0	12	6	15	45.71	91.9
TFC11	0	0	0	12	6	15	39.35	88.8

Using the selected design, the independent parameters and dependent variables were fitted to Equation 3. The goodness of fit for each variable was evaluated for both water flux and salt rejection. The regression coefficients obtained through the two-level-interaction (2FI) factorial fit for each response and their interactions in terms of coded factors are presented in Table 3-2.

Table 3-2 Analysis of variance of the 2FI regression model for water flux and salt rejection.

Model term	**Water Flux (L/m^{2}h)**				**Salt Rejection (R%)**			
	Regression Coefficient (β)	**Sum of Square**	**F-Value**	**P-Value**	**Regression Coefficient (β)**	**Sum of Square**	**F-Value**	**P-Value**
Intercept	33.90	-	-	-	88.68	-	-	-
A	-7.38	436.01	58.68	0.0046	-1.07	9.16	4.35	0.1283
B	-1.66	22.04	2.97	0.1835	3.74	112.05	53.23	0.0053
C	-2.48	49.20	6.62	0.0823	-0.53	2.29	1.09	0.3736
AB	0.76	4.62	0.62	0.4879	1.66	22.04	10.47	0.0480
AC	-0.11	0.097	0.013	0.9163	-0.047	0.018	0.0086	0.9321
BC	0.76	4.65	0.63	0.4866	2.03	32.97	15.66	0.0288
Curvature	-	153.37	20.64	0.0200	-	6.98	3.32	0.1661
P-Value for the model		0.0350				0.0265		
P-Value for the lack of fit		0.7229				0.5245		
R^2		0.9586				0.9658		
Adjusted R^2		0.8759				0.8975		
Predicted R^2		0.7749				0.4662		

Pareto charts in Fig 3-2 indicate the effect of all studied factors on water flux and salt rejection, in which the effective parameters are represented in descending order of frequency and the length of bars shows proportional impact of each parameter on the specified response with 95 % confidence level.

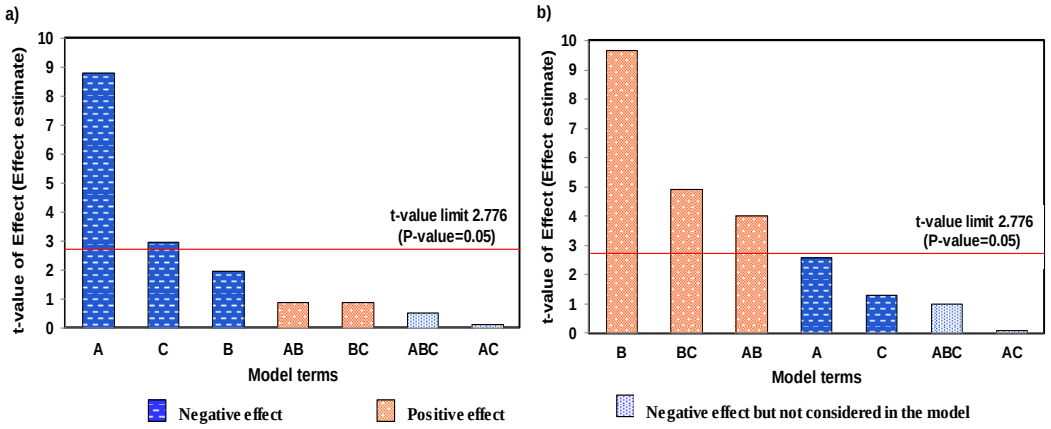

Figure 3-2 Pareto charts for the effect of various parameters on (a) water flux; (b) salt rejection (A: PSF concentration, B: MPD soaking time, and C: heat curing time).

The probability value (*p*-value) is used as a tool for assessing significant terms. The *p*-value is the smallest level of significance that leads to the null hypothesis to be rejected. Generally, *p*-values of less than 0.05 (95 % confidence interval) lead to the rejection of null hypothesis and the parameter associated with them is considered significant. Herein, 0.05 was chosen as the significance level and the minimum adequate model was obtained by stepwise deletion of non-significant terms.

After backward elimination of non-significant terms, the final empirical models in terms of coded factors were obtained as equations 4 and 5:

$$Y_1 = 33.90 - 7.38A - 2.48C \quad (4)$$

$$Y_2 = 88.68 - 1.07A^* + 3.74B - 0.53C^* + 1.66AB + 2.03BC \quad (5)$$

In terms of actual factors, the final models can be expressed as:

$$Y_1 = 70.87 - 2.46(Concentration) - 0.49(Curing\ time) \quad 6)$$

$$Y_2 = 108.04 - 1.19(Concentration)^* - 2.25(MPD\ soaking\ time) - 0.72(Curing\ time)^* + 0.14(Concentration)(MPD\ soaking\ time) + 0.10(MPD\ soaking\ time)(Curing\ time) \quad (7)$$

Note that although PSF concentration and curing time are not statistically significant, they are represented in the salt rejection reduced model to maintain hierarchy. The summary of ANOVA table for the reduced 2FI model is represented in Table 3-3 (a, b).

Table 3-3 (a) Analysis of variance of the reduced 2FI regression model for water flux and salt rejection (b) Statistics used to investigate the goodness of fit for the reduced water flux and salt rejection models.

(a)

Model term	Water Flux (L/m^{2}h)				Salt Rejection (R%)			
	Regression Coefficient (β)	Sum of Square	F-Value	P-Value	Regression Coefficient (β)	Sum of Square	F-Value	P-Value
Intercept	33.90	-	-	-	88.68	-	-	-
A	-7.38	436.01	56.83	0.0001	-1.07	9.16	8.14	0.0739*
B	-	-	-	-	3.74	112.05	74.55	0.0011
C	-2.48	49.20	6.41	0.0391	-0.53	2.29	2.87	0.2954*
AB	-	-	-	-	1.66	22.04	17.05	0.0203
AC	-	-	-	-	-0.047	-	0.19	-
BC	-	-	-	-	2.03	32.97	24.30	0.0203
Curvature	-	153.37	19.99	0.0029	-	6.98	5.3	0.0103

*Although factors A and C are not significant for the salt rejection case, these terms have remained in the model to maintain hierarchy.

(b)

Statistics	Water Flux (L/m^{2}h)	Salt Rejection (R%)
P-Value for the model	0.0003	0.0050
P-Value for the lack of fit	0.7012	0.7716
R^2	0.9003	0.9655
Adjusted R^2	0.8719	0.9229
Predicted R^2	0.8106	0.8221
C.V. %	7.65	1.41
Stdandard Deviation	2.77	1.26
Adequate Precission	11.809	14.810

Among linear coefficients (A, B, C), PSF concentration (A) and heat curing time (C) had significant effects on water flux (Y1) ($p < 0.05$). However, MPD soaking time (B) and interactions appeared to have non-significant influences on water flux ($p >> 0.05$). For the salt rejection (Y2), among the selected parameters, MPD soaking time (B) was convinced to be the most influential individual term while the influence of PSF concentration and curing time were not significant. The interactions within PSF concentration-MPD soaking time (AB) and MPD soaking time-curing time (BC) were also found to be statistically significant on the salt rejection. In summary, the statistical analysis results revealed that, among studied parameters, the PSF concentration is the most significant term with respect to water flux, while MPD soaking time has the highest influence on salt rejection.

The goodness of fit for the models was evaluated through the ANOVA, as summarized in Table 3-3(a, b). As presented, the fitted models for both responses were significant ($p < 0.05$), indicating that the model terms have remarkable influence on the responses. The corresponding p-value to the lack of fit, which is the measure of model fitness and reveals the variation of the data around the fitted model, was found to be insignificant for both models. This is a desirable result, which confirms the models fit well. Another important parameter is the coefficient of determination (R^2), which is a measure of the amount of variation around the mean and shows the accuracy of model. Where R^2 is close to 1, the associated model is considered acceptable. However, since R^2 increases with the addition of more variables to the model, regardless of their significance, its closeness to unity does not always imply that the regression model is accurate. Hence, using adjusted-R^2, which is the modified R^2 considering the numbers of model terms, is more recommended [29]. The adjusted-R^2 close to 90 % indicates high model accuracy in terms of predicting the values in the study domain. Therefore, the adjusted and predicted R^2 for both models are in reasonable agreement with each other, which certifies the models' accuracy and goodness (Table 3-3b). C.V. %, which stands for the coefficient of variation, is the standard deviation as a percentage of the mean. Whereas the C.V. % should be less than 10 for a good model, the obtained models in this study for both water flux and salt rejection can be considered accurate. Another important regression term for the model evaluation is the adequate precision which calculates the signal to noise ratio by comparing the range of the predicted values at the design points to the average prediction error. An adequate precision higher than 4 is desirable, implying that the model is able to navigate through the design area. Herein, the adequate precision for both responses is greater than 4, which once again confirms the models' goodness of fit [29]. The actual experimental responses versus the predicted values as represented in Fig 3-3 are also in good agreement with each other, confirming the adequacy of model for prediction of responses in the design domain.

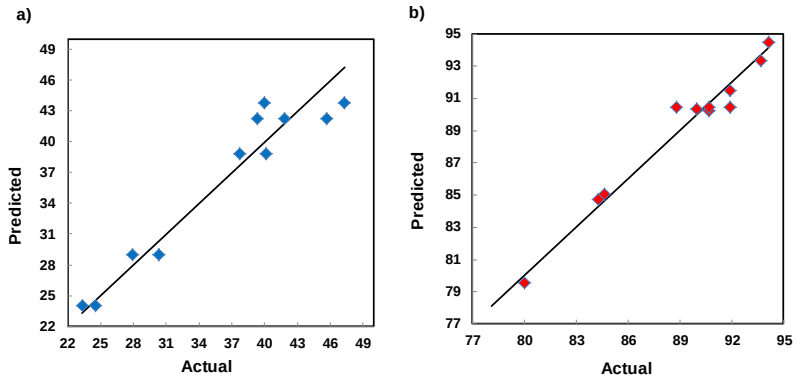

Figure 3-3 Actual vs. predicted values of the responses by the regression models: (a) water flux; (b) salt rejection.

3D Surface plots of water flux and salt rejection as a function of studied parameters are represented in Fig 3-4 for interpretation of the results.

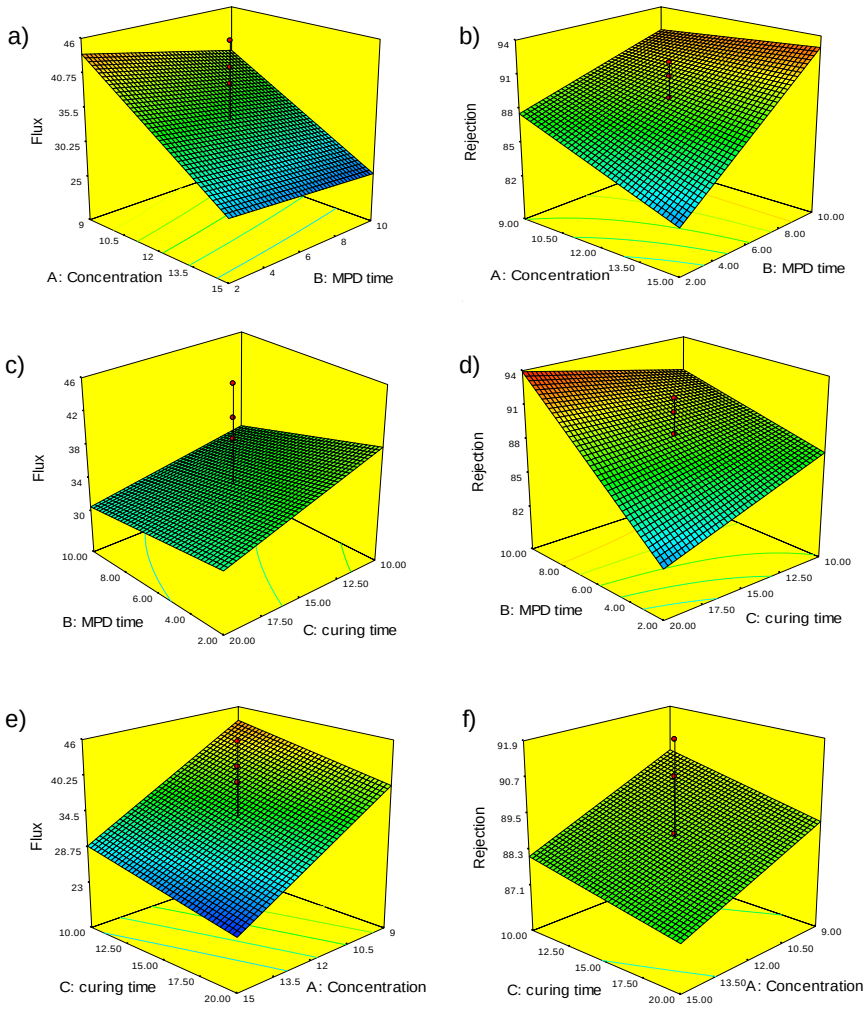

Figure 3-4 Response surface plots of water flux and salt rejection as a function of: (a, b) PSF concentration (A) and MPD soaking time (B) at a fixed heat curing time of 15 min; (c, d) MPD soaking time (B) and heat curing time (C) at a fixed MPD soaking time of 6 min.

The contour plots have also been demonstrated in supporting information (Fig 3S-4). The obtained models can be helpful to advance the general understanding of the interaction of the studied parameters and the results can provide insights to best determine the values of these parameters in different systems considering their interrelationships.

3.4.2. Effect of PSF concentration and its significant interactions

Concentration of PSF in casting solution was selected as one of the model terms, as polymer concentration in the casting solution has been proven to have considerable impact on the structure and morphology of support layer [14, 31]. Higher viscosity of the concentrated casting polymer solutions results in lower transform rate and therefore, slower liquid-liquid demixing in the precipitation bath. This phenomenon delays the propagation of the finger-like macrovoids during phase inversion process and as a result fewer macrovoids form in the fabricated PSF supports [14, 32]. It has also been reported that the surface porosity of PSF membranes decreases by increasing the polymer concentration due to an enhanced local concentration of polymer in the interface of PSF film and non-solvent (water in this case) while precipitation occurs [32]. Therefore, the more the concentration of PSF in the casting solution, the less the general porosity of the obtained PSF supports would be.

Fig 3-5 illustrates the SEM images of cross-section and bottom view of three PSF supports casted from 9, 12 and 15 % PSF-DMF solutions. It is evident from the SEM micrographs of the PSF supports casted with 9 % PSF [Fig 3-5(a, b)] that such membranes contain uniform finger-like pores spanned throughout the whole PSF support, leading to an open porous structure on the bottom of the TFC-RO membranes. The finger-like structure with open pores is a desirable characteristic in terms of producing higher water permeable PSF support layers and consequently higher water flux of TFC-RO membranes. On the contrary, using 15 % PSF casting solutions, the sponge-like structured PSF supports with rare macro-voids in the middle of the layer are formed. That explains why 15 % PSF fabricated TFC-RO membranes display lower water flux compared with the 9 % PSF supported TFC-RO membranes [Table 3-1.b, Fig 3-5(e, f)]. The low porosity of PSF interlayer also contributes to the formation of denser PA selective barrier layer during the subsequent interfacial polymerization course due to limited diffusion of MPD

monomers [8, 33]. Hence, the formation of low water permeable PA selective barrier layers on the PSF supports with low porosity further decreases the overall water flux of the resulting TFC-RO membranes. That can explain why the water fluxes significantly declined with the increment of PSF concentration (Table 3-1b).

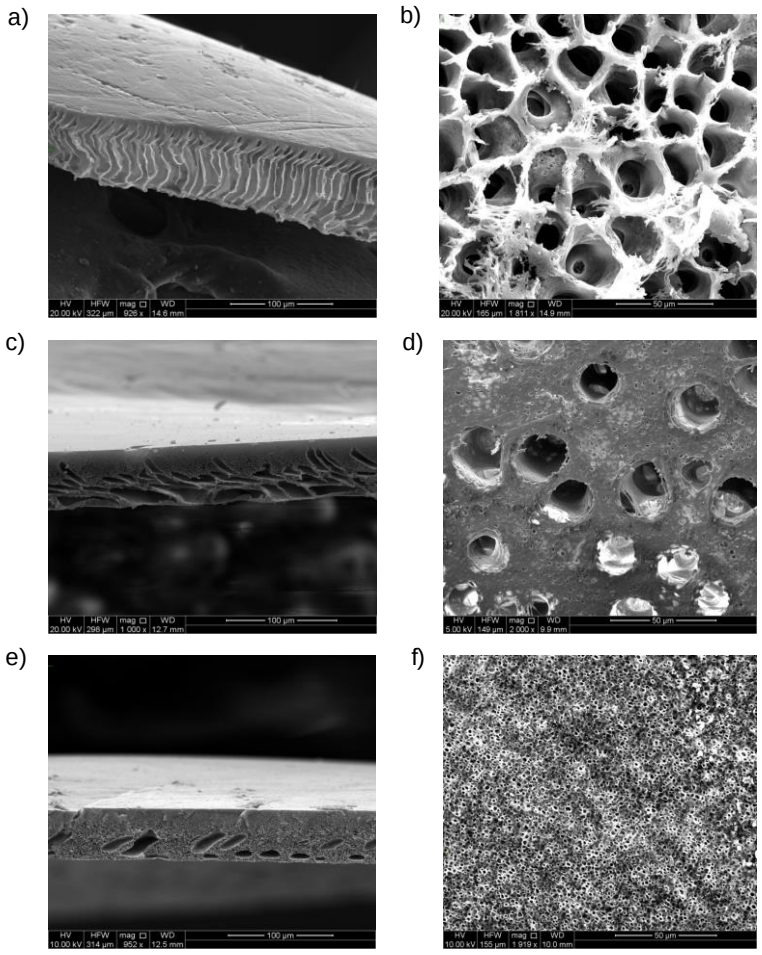

Figure 3-5 SEM micrographs displaying the cross-section (left) and bottom (right) of PSF support layers cast using different concentrations of PSF: (a,b) 9 %; (c,d) 12 %; (e,f) 15 %.

On the other hand, greater salt rejection is expected for the TFC-RO membranes fabricated with denser PSF support layers [26]. However, the salt rejection data of some TFC-RO membranes at different MPD soaking times appeared to be contradicted with what we assumed, although the PSF concentration by itself was not recognised as a significant term. This can be explained through the statistically significant influence of MPD soaking time and PSF concentration interaction. Fig 3-4b shows that salt rejection decreases as the PSF concentration increases with a short MPD soaking time. This might be due to the smaller porosity of PSF support

membrane at higher concentrations, which contributes to lower MPD adsorption in a shorter soaking time and results in forming pinhole defects or lower degree of cross-linking density in the PA selective barrier layer which is formed subsequently [30]. However, at a long soaking time, the dense PSF supports fabricated through high concentrated casting solutions could get sufficiently wet by the MPD aqueous solution, leading to a higher salt rejection.

3.4.3. Effect of aqueous phase soaking time and its significant interactions

Considering the response values for the desalination performance of the TFC-RO membranes (Table 3-1b) and the corresponding *p*-values (Table 3-3a), MPD soaking time showed insignificant negative influence on water flux but highly significant positive effect on salt rejection. Our experimental results indicated that an increase in the soaking time results in declining water flux, but improving salt rejection when the PSF concentration is set at both high and low levels. This can be explained by the fact that PSF support can adsorb more MPD and get wet better when encountered with the MPD aqueous phase for longer time. Therefore, a long MPD soaking time can increase the MPD penetration depth inside the PSF support pores, resulting in reducing water permeability of TFC-RO membranes. It could also decline the formation of defects in the PA selective layer formed on the surface of denser supports, and hence increases salt rejection capability [30, 34]. This is in line with the significant influence of PSF concentration and MPD soaking time interaction on salt rejection. The relatively small influence of the long MPD soaking time on water flux can be explained by the interfacial polymerization which is the reaction among the monomers on the interface of two immiscible aqueous and organic phases. Although the long MPD soaking time enhances the MPD monomer penetration inside the PSF support, the PA selective layer cannot highly diffuse inside the PSF pores due to the limited TMC supply to the interlayers. Hence, an increment of MPD soaking time does not make significant reductions in water flux but could make substantial improvement in salt rejection, especially in the case of TFC-RO membranes formed on dense PSF supports. Therefore, a longer MPD soaking time should be considered for fabricating TFC-RO membranes on the support layers with smaller pores.

3.4.4. Effect of heat curing time and its interactions

Most of the reported studies on MPD-TMC reaction system emphasize on heat curing as an important stage for stabilizing and strengthening the PA selective layer [16]. Considering the response values for the experiments presented in Table 3-1b and the regression coefficients associated with curing time, it is suggested that the heat curing time at 60 °C has significant influence on water flux, while it has insignificant effect on salt rejection in the design domain. Curing leads to extra solvent removal from the TFC-RO membranes. It can also facilitate additional cross-linking and increase the PA packing density which provides stronger PA selective layer. This phenomenon results in decreasing overall TFC-RO membrane porosity and consequently water flux reduction [15, 16, 25]. This explanation justifies the negative effect of increased curing time on the water flux.

On the other hand, curing time seems to have complex effect on salt rejection. Generally, a denser and more cross-linked structure of PA selective layer is obtained following a longer curing time which leads to a stronger barrier against water and salt passage [16]. Therefore, salt rejection could be improved by increasing the curing time. That is most likely the case when the procedure involves a longer MPD soaking time which can ensure wetness of all surface pores and thus minimize defect formation. However, prolonged curing might also result in damaging the ultrathin PA selective barrier layer, form defects and consequently decrease the salt rejection capability [9]. In this case, when the curing is operated at a short soaking time, less MPD is adsorbed on the surface pores. As a result, the TFC-RO membrane could be formed with a thinner and more superficial PA layer, compared with the TFC-RO membranes fabricated in a longer MPD soaking time which can increase the possibility of PA selective layer shrinkage and defect formation in a longer curing time. That explains why the increment in curing time can have a negative influence on salt rejection of TFC-RO membranes fabricated over denser PSF support layers at a shorter MPD soaking time. Herein, the experimental results and the statistical analysis showed that curing for 10 min provided TFC-RO membranes with higher water flux and acceptable salt rejection. Therefore, 10 min can be considered as the optimum curing time value for the case of hexane as the organic solvent and 60°C curing temperature.

3.5. Conclusions

This study focused on the interactions of three key parameters of PSF support membrane concentration, aqueous phase soaking time and heat curing time during the course of TFC-RO membrane fabrication. We statistically analysed these parameters' simultaneous impact on TFC-RO membrane desalination performance in terms of water flux and salt rejection. Fabrication conditions of TFC-RO membranes were tailored according to a 2^3 full factorial design of experiments. The linear regression models were fitted to the experimental data of water flux and salt rejection. Experimental data of desalination performance and characteristics of the TFC-RO membranes revealed that these three synthesis parameters and their interactions could significantly affect thin film layer structures and consequently water flux and salt rejection values. Statistical analysis results showed that PSF concentration had the most significant impact on the water flux, while MPD soaking time was the most influential parameter on the salt rejection. A high PSF concentration and long curing time for the TFC-RO membrane fabrication could lead to significant reduction of the water flux, while their impact on the salt rejection was subject to the MPD soaking time. A longer MPD soaking time resulted in a slight decline in water flux, while highly improved salt rejection capability of the membranes. From our experimental results, it can be generally concluded that, for 15 % PSF concentration, at any curing time, a higher MPD soaking time is required to achieve the best performance. On the other hand, for 9 % PSF concentration, at low curing time, a lower MPD soaking time and at high curing time, a higher MPD soaking time can give the best performance results. ANOVA confirmed that the fitted regression models were accurate enough to navigate through the designed domain. Finally, we can emphasize that interaction correlations along with the individual parameters should be considered when devising a strategy to synthesize TFC-RO membranes in order to ensure desirable desalination performance.

References

[1] J.E. Cadotte, Reverse osmosis membrane, in, U.S., August 1977.

[2] N. Misdan, W.J. Lau, A.F. Ismail, Seawater Reverse Osmosis (SWRO) desalination by thin-film composite membrane—Current development, challenges and future prospects, Desalination, 287 (2012) 228-237.

[3] R. Baker, Membrane Technology and Applications (3rd Edition), John Wiley & Sons, Somerset, NJ, USA, 2012.

[4] M. Elimelech, Z. Xiaohua, A.E. Childress, H. Seungkwan, Role of membrane surface morphology in colloidal fouling of cellulose acetate and composite aromatic polyamide reverse osmosis membranes, Journal of Membrane Science, 127 (1997) 101-109.

[5] D. Li, H. Wang, Development of Reverse Osmosis Membranes in Desalination: A Review, in: Chemeca 2010: Engineering at the Edge, Barton, A.C.T.: Engineers Australia, Hilton Adelaide, South Australia, 2010, pp. 490-499.

[6] B.H. Jeong, E.M.V. Hoek, Y. Yan, A. Subramani, X. Huang, G. Hurwitz, A.K. Ghosh, A. Jawor, Interfacial polymerization of thin film nanocomposites: A new concept for reverse osmosis membranes, Journal of Membrane Science, 294 (2007) 1-7.

[7] R.J. Petersen, Composite reverse osmosis and nanofiltration membranes, Journal of Membrane Science, 83 (1993) 81-150.

[8] A.K. Ghosh, E.M.V. Hoek, Impacts of support membrane structure and chemistry on polyamide–polysulfone interfacial composite membranes, Journal of Membrane Science, 336 (2009) 140-148.

[9] R.X. Zhang, J. Vanneste, L. Poelmans, A. Sotto, X.L. Wang, B. Van der Bruggen, Effect of the manufacturing conditions on the structure and performance of thin-film composite membranes, Journal of Applied Polymer Science, 125 (2012) 3755-3769.

[10] Azari, S., Karimi, M., Kish, M. H., Structural Properties of the Poly(acrylonitrile) Membrane Prepared with Different Cast Thicknesses, Anglais, 49 (2010) 7.

[11] S. Yu, M. Liu, X. Liu, C. Gao, Performance enhancement in interfacially synthesized thin-film composite polyamide-urethane reverse osmosis membrane for seawater desalination, Journal of Membrane Science, 342 (2009) 313-320.

[12] J.R. McCutcheon, M. Elimelech, Influence of membrane support layer hydrophobicity on water flux in osmotically driven membrane processes, Journal of Membrane Science, 318 (2008) 458-466.

[13] N. Misdan, W.J. Lau, A.F. Ismail, T. Matsuura, Formation of thin film composite nanofiltration membrane: Effect of polysulfone substrate characteristics, Desalination, 329 (2013) 9-18.

[14] A. Tiraferri, N.Y. Yip, W.A. Phillip, J.D. Schiffman, M. Elimelech, Relating performance of thin-film composite forward osmosis membranes to support layer formation and structure, Journal of Membrane Science, 367 (2011) 340-352.

[15] A. Prakash Rao, S.V. Joshi, J.J. Trivedi, C.V. Devmurari, V.J. Shah, Structure–performance correlation of polyamide thin film composite membranes: effect of coating conditions on film formation, Journal of Membrane Science, 211 (2003) 13-24.

[16] A.K. Ghosh, B.H. Jeong, X. Huang, E.M.V. Hoek, Impacts of reaction and curing conditions on polyamide composite reverse osmosis membrane properties, Journal of Membrane Science, 311 (2008) 34-45.

[17] R.R. Sharma, S. Chellam, Temperature and concentration effects on electrolyte transport across porous thin-film composite nanofiltration membranes: Pore transport mechanisms and energetics of permeation, Journal of Colloid and Interface Science, 298 (2006) 327-340.

[18] J. Wei, X. Liu, C. Qiu, R. Wang, C.Y. Tang, Influence of monomer concentrations on the performance of polyamide-based thin film composite forward osmosis membranes, Journal of Membrane Science, 381 (2011) 110-117.

[19] I.C. Kim, J. Jegal, K.H. Lee, Effect of aqueous and organic solutions on the performance of polyamide thin-film-composite nanofiltration membranes, Journal of Polymer Science Part B: Polymer Physics, 40 (2002) 2151-2163.

[20] T. Wang, Y. Yang, J. Zheng, Q. Zhang, S. Zhang, A novel highly permeable positively charged nanofiltration membrane based on a nanoporous hyper-crosslinked polyamide barrier layer, Journal of Membrane Science, 448 (2013) 180-189.

[21] S.S. Madaeni, S. Koocheki, Application of taguchi method in the optimization of wastewater treatment using spiral-wound reverse osmosis element, Chemical Engineering Journal, 119 (2006) 37-44.

[22] M. Khayet, C. Cojocaru, M. Essalhi, Artificial neural network modeling and response surface methodology of desalination by reverse osmosis, Journal of Membrane Science, 368 (2011) 202-214.

[23] A. Idris, F. Kormin, M.Y. Noordin, Application of response surface methodology in describing the performance of thin film composite membrane, Separation and Purification Technology, 49 (2006) 271-280.

[24] J.M. Gohil, A.K. Suresh, Development of high flux thin-film composite membrane for water desalination: a statistical study using response surface methodology, Desalination and Water Treatment, 52 (2013) 5219-5228.

[25] A. Prakash Rao, N.V. Desai, R. Rangarajan, Interfacially synthesized thin film composite RO membranes for seawater desalination, Journal of Membrane Science, 124 (1997) 263-272.

[26] P.S. Singh, S.V. Joshi, J.J. Trivedi, C.V. Devmurari, A.P. Rao, P.K. Ghosh, Probing the structural variations of thin film composite RO membranes obtained by coating polyamide over polysulfone membranes of different pore dimensions, Journal of Membrane Science, 278 (2006) 19-25.

[27] C.J. Lee, S.S. Wang, G.C. Lin, W. Hu, L.T. Chen, Pilot Production of Polysulfone Hollow Fiber for Ultrafiltration Using Orthogonal Array Experimentation, Industrial & Engineering Chemistry Research, 34 (1995) 813-819.

[28] S. Pourjafar, M. Jahanshahi, A. Rahimpour, Optimization of TiO_2 modified poly(vinyl alcohol) thin film composite nanofiltration membranes using Taguchi method, Desalination, 315 (2013) 107-114.

[29] D.C. Montgomery, Design and Analysis of Experiments, John Wiley & Sons, New York, 1996.

[30] W. Xie, G.M. Geise, B.D. Freeman, H.S. Lee, G. Byun, J.E. McGrath, Polyamide interfacial composite membranes prepared from m-phenylene diamine, trimesoyl chloride and a new disulfonated diamine, Journal of Membrane Science, 403–404 (2012) 152-161.

[31] C.A. Smolders, A.J. Reuvers, R.M. Boom, I.M. Wienk, Microstructures in phase-inversion membranes. Part 1. Formation of macrovoids, Journal of Membrane Science, 73 (1992) 259-275.

[32] R.M. Boom, I.M. Wienk, T. van den Boomgaard, C.A. Smolders, Microstructures in phase inversion membranes. Part 2. The role of a polymeric additive, Journal of Membrane Science, 73 (1992) 277-292.

[33] M.F. Jimenez-Solomon, P. Gorgojo, M. Munoz-Ibanez, A.G. Livingston, Beneath the surface: Influence of supports on thin film composite membranes by interfacial polymerization for organic solvent nanofiltration, Journal of Membrane Science, 448 (2013) 102-113.

[34] M. Fathizadeh, A. Aroujalian, A. Raisi, Effect of lag time in interfacial polymerization on polyamide composite membrane with different hydrophilic sub layers, Desalination, 284 (2012) 32-41.

TOC:

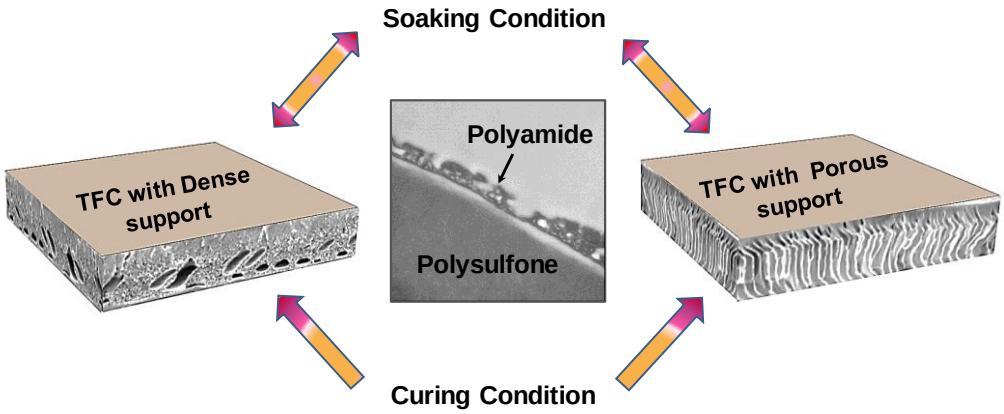
Soaking Condition
TFC with Dense support
Polyamide
Polysulfone
TFC with Porous support
Curing Condition

3.6. Supporting Information

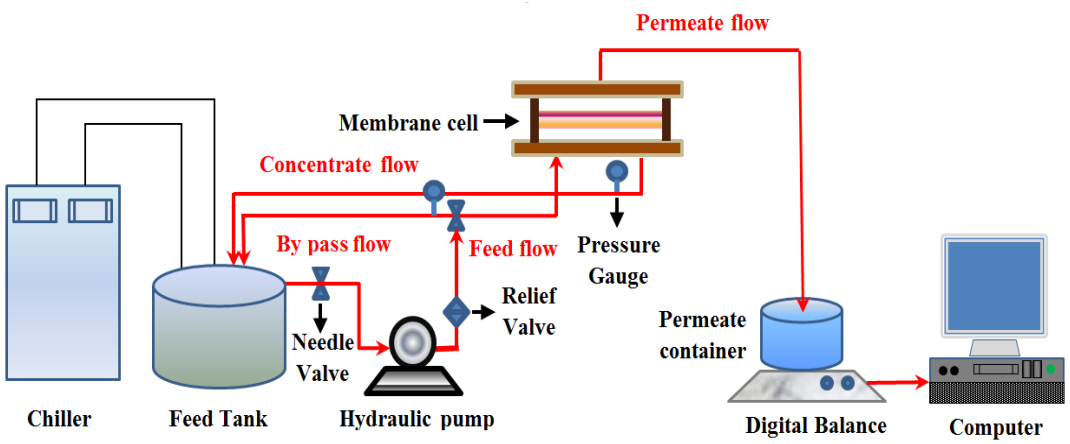

Fig3S-1 Schematic representation of the established desalination setup

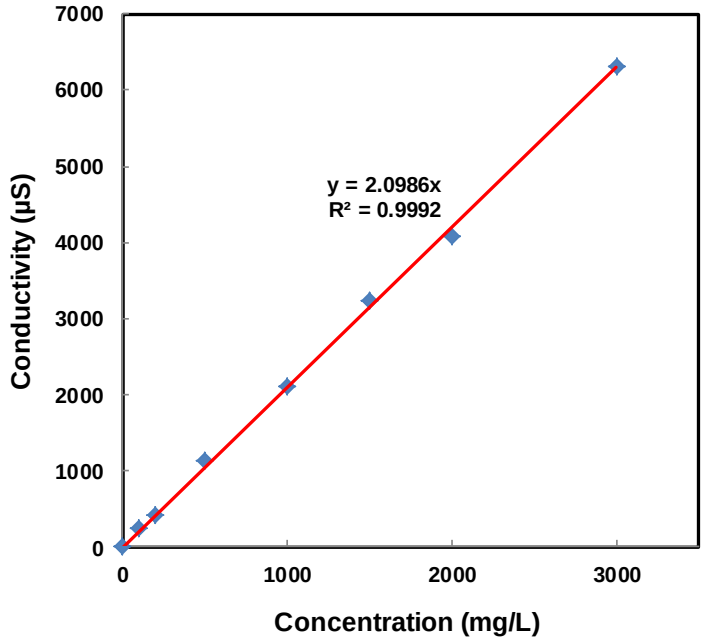

Fig 3S-2 The Measured calibration curve relating conductivity to NaCl concentration for calculating the salt rejection values

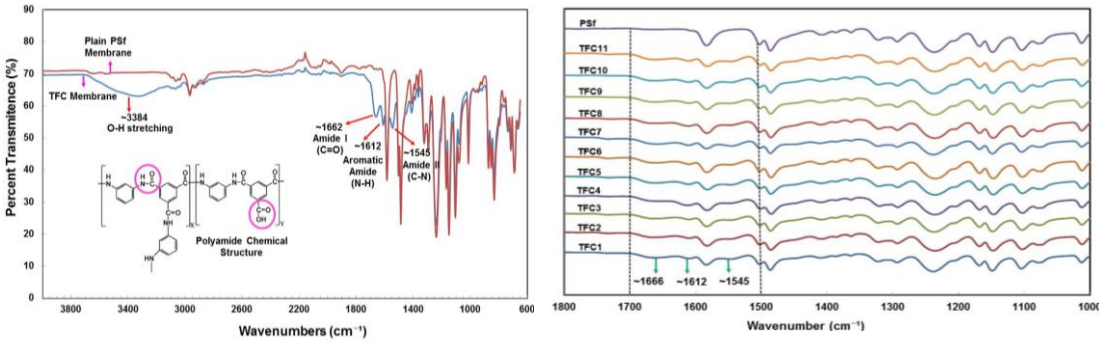

Fig 3S-3 ATR-FTIR spectra of (a) a typically fabricated TFC-RO membrane in comparison with its PSF support; (b) fabricated TFC-RO membranes at different experimental conditions in this study. The emergence of primary amide characteristic groups of PA at around 1660, 1612 and 1545 cm-1 associated with C=O (amide I band), N-H (aromatic amide) and C-N (amide II band) respectively, indicated the successful formation of PA selective barrier layer over PSF substrate under different experimental conditions. In addition, a broad stretching absorption band at around 3400cm-1 which is the characteristic of stretching -OH in the carboxylic acid functional group (-COOH) also certifies the formation of polyamide over PSF membrane.

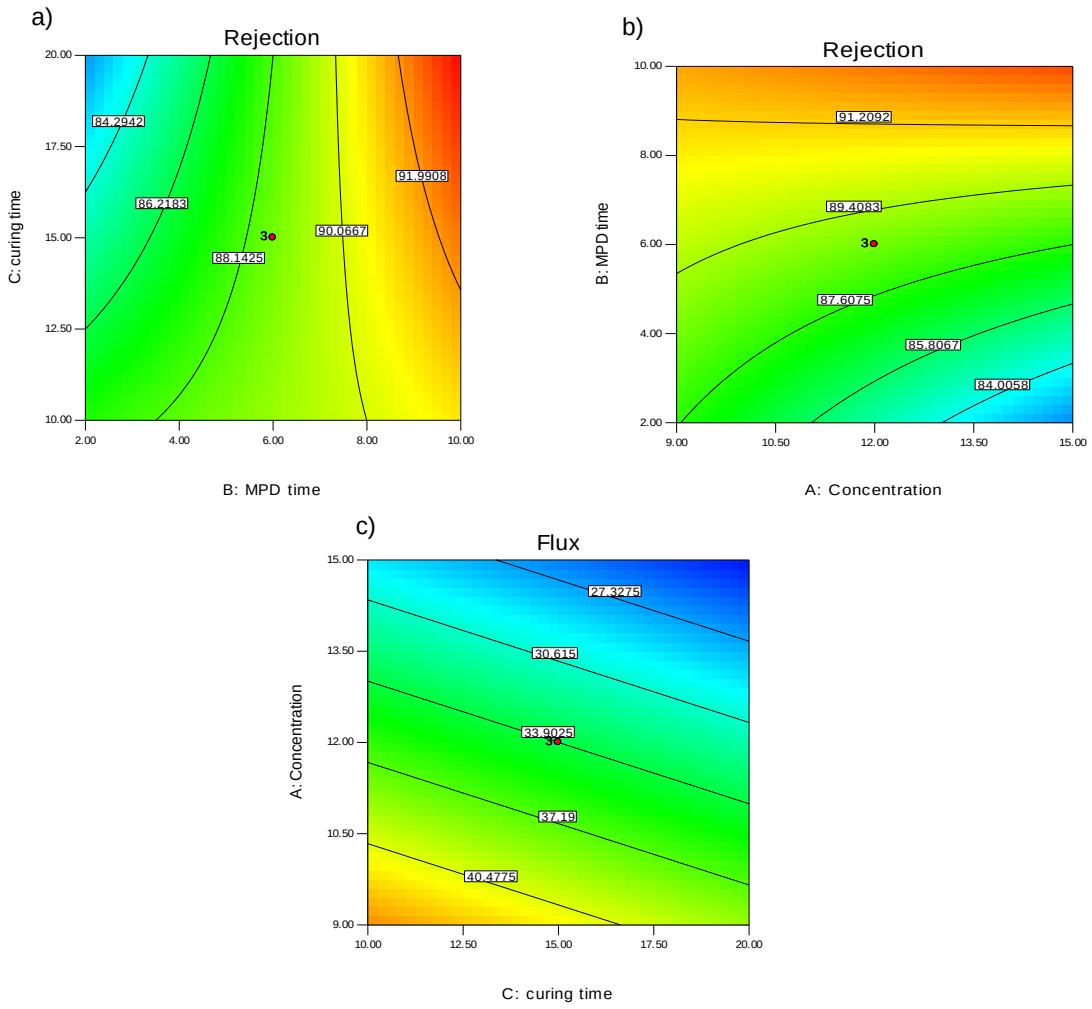

Fig 3S-4 Contour plots for the water flux and salt rejection demonstrating the effect of different process variables on the water flux and salt rejection for better visualization of the results (a) Curing time (C) and MPD soaking time (B) on salt rejection at the fixed PSF concentration of 12 %; (b) MPD soaking time (B) and PSF concentration (A) on salt rejection at a fixed curing time of 15 min; (c) PSF concentration (A) and Curing time (C) on water flux at a fixed MPD soaking time of 6 min

Chapter 4

Statement of Authorship

Title of Paper	Understanding Functionalized Nanoparticle Incorporation in Thin Film Composite Membranes: Interaction and Desalination Performance
Publication Status	☐ Published ☐ Accepted for Publication ☑ Submitted for Publication ☐ Unpublished and Unsubmitted w ork w ritten in manuscript style
Publication Details	Masoumeh Zargar, Yusak Hartanto, Bo Jin*, Sheng Dai*, Understanding Functionalized Nanoparticle Incorporation in Thin Film Composite Membranes: Interaction and Desalination Performance, Submitted to Journal of membrane science (JMS-15-1287).

Principal Author

Name of Principal Author (Candidate)	Masoumeh Zargar
Contribution to the Paper	Designing and performing the experiments, analysis of the results and writing the manuscript.
Certification:	This paper reports on original research I conducted during the period of my Higher Degree by Research candidature and is not subject to any obligations or contractual agreements with a third party that would constrain its inclusion in this thesis. I am the primary author of this paper.
Signature	Date: 22/09/2015

Co-Author Contributions

By signing the Statement of Authorship, each author certifies that their stated contribution to the publication is accurate and that permission is granted for the publication to be included in the candidate's thesis.

Name of Co-Author	Yusak Hartanto
Contribution to the Paper	Assistance in some characterizations.
Signature	Date: 22/09/2015

Name of Co-Author	Bo Jin
Contribution to the Paper	Supervising the development of the work, assisting in the manuscript review and assessment.
Signature	Date: 22/9/2015

Name of Co-Author	Sheng Dai
Contribution to the Paper	Supervising the development of the work, assisting in the data interpretation, manuscript review and assessment.
Signature	Date: 22/9/2015

Understanding Functionalized Nanoparticle Incorporation in Thin Film Composite Membranes: Interactions and Desalination Performance

Masoumeh Zargar, Yusak Hartanto, Bo Jin*, Sheng Dai*

School of Chemical Engineering, The University of Adelaide, SA, 5005, Australia

*Corresponding authors

E-mail: bo.jin@adelaide.edu; s.dai@adelaide.edu.au

Submitted to Journal of Membrane Science (JMS-15-1287)

4.1. Abstract

The emergence of nanotechnology in membrane science has opened new frontiers in the development of advanced thin film nanocomposite (TFN) membranes. However, the possibility of nanoparticles' leakage and their low compatibility with organic membranes make the successful fabrication of TFN membranes challenging. Herein, a series of TFN membranes incorporated with differently sized and surface functionalized silica nanoparticles (SN) were fabricated to get a better understanding on the interfacial interaction between nanoparticles and thin film composite (TFC) membranes. The physicochemical properties of functionalized SN and their resulting TFN membranes were characterized using SEM, TEM, DLS, TGA, ATR-FTIR, tensiometer and streaming potential analysis. The results confirm the successful incorporation of SN to the TFC membranes. The surface hydrophilicity, surface morphology and surface chemistry of resultant membranes can be strongly affected by the concentration, size and surface functionality (hydroxyl, epoxy and amine) of SN. Water fluxes increase after SN hybridization with 40% increase for the 0.1 wt. % SN-TFC without sacrificing salt rejection capability. In addition, nanoparticle surface functionalization using epoxy and amine moieties facilitates the chemical interaction between SN and the TFC membranes, resulting in a more stable TFN membrane. Our research outcomes provide new insights into the structure-performance correlation of the TFC membranes incorporated with various inorganic nanoparticles.

Keywords: Thin film nanocomposite membrane, Surface modification, Water flux, Salt rejection, Structure-property correlation

4.2. Introduction

Nowadays, polymeric thin film composite (TFC) membranes have received increasing applications for separation and purification processes such as desalination and wastewater treatment. The TFC membranes demonstrate higher separation performance and stability over a wider range of temperature and pH compared with traditionally used cellulose acetate membranes [1]. Although many studies on fabrication and separation performance of the TFC membranes have been reported during the past decades, there is an on-going need to develop technically and economically feasible TFC membranes, which are able to enhance separation capability and efficiency, and reduce energy and capital costs for various industrial and municipal applications [2, 3].

Recent studies reported that the integration of nanoparticles with the TFC membranes to fabricate thin film nanocomposite (TFN) membranes can improve physicochemical properties such as hydrophilicity, mechanical stability and thermal resistance in addition to the permselectivity of the generated TFN membranes [4-6]. The commonly used nanoparticles include zeolite [5, 7, 8], silica [9-12], titanium dioxide [13, 14], silver [15, 16], graphene oxide [17-19], carbon nanotubes [6, 20, 21] and so on. The TFN membranes can be fabricated through either direct deposition of the TFC membranes with nanoparticles or incorporating nanoparticles into the TFC membrane during the interfacial polymerization course. Surface deposition approach is deemed as a post modification strategy and is mainly used for improving the antifouling capability of the membranes. Although this method makes the modified TFC membranes more active due to the high exposure of nanoparticles to membrane surface, the deposited nanoparticles might be lost during high pressure filtration processes. Therefore, it is necessary to functionalize nanoparticles by chemical modification to enhance the stability on TFN membrane surface. Further, generation of stress weak points due to possible nanoparticle aggregation might be another issue associated with the TFN membranes fabricated through deposition approach, which gives rise to the chance of future defect formation during the filtration processes. The other strategy is the incorporation of nanoparticles into the TFC membrane through mixing them with either aqueous or organic phase during the interfacial polymerization process. Jeong et al. (2007) fabricated the first TFN

membrane through in-situ incorporation of zeolite A nanoparticles (size 50-200 nm) to the polyamide (PA) membranes and reported enhanced separation performance and fouling resistance for their synthesized TFN membranes [7]. The sustainable improvement in the structure and performance of the TFN membranes is highly dependent on the stability of nanoparticles inside the membrane matrix together with their homogeneous and controllable distribution [4]. Although some nanoparticles might be exposed to the membrane surface in this approach, the overall stability of nanoparticles in the TFN membrane is higher than the membranes prepared by surface deposition strategy due to the partially or fully encapsulation of nanomaterials inside the PA thin film layers.

Silica nanoparticles (SN) have good biocompatibility and mechanical stability and can be easily surface functionalized [10, 22]. Importantly, SN show hydrophilic characteristic due to their abundant surface hydroxyl groups which can be beneficial for enhancing permeability and fouling resistance of the TFN membranes [4, 9]. Therefore, some researchers have studied the application of SN to modify TFC membranes. For instance, Tiraferri et al. (2012) studied the incorporation of commercial silica with an average diameter of 14 nm on the surface of TFC membranes via the post-fabrication modification strategy to improve membranes' antifouling capability and reported a high fouling resistance for their TFN membranes [11].

Till now, there is very few studies reported on understanding the influence of in-situ introduction of nanomaterials on the chemistry of the fabricated TFN membranes. Further, the extensive identification of physicochemical properties of TFN membranes after introducing nanoparticles with different surface functionalities and correlation of them with the TFN performance were missing in the previous studies. This study aims to address these gaps in the literature, and develops novel TFN membranes incorporated with SN having different sizes and surface functional groups. Our research will focus on evaluating the structure-property correlation of resulting TFN membranes. We will synthesize different sized SN (fitting in the range of PA thickness) followed by functionalizing their surfaces with amine or epoxy functional groups to be ready to interact with PA monomers during the interfacial polymerization, and then incorporate these fabricated nanoparticles into the TFC membranes. The surface functionalization of the fabricated SN and the

physicochemical properties of the synthesized TFN membranes, which are called as SN incorporated TFC (SN-TFC) in this study, are extensively characterized. Further, desalination performance of the SN-TFC membranes in terms of water flux and salt rejection are evaluated using a cross-flow filtration unit. The research outcomes will provide new insights into the effect of nanoparticle incorporation on the overall performance and properties of TFN membranes.

4.3. Experimental

4.3.1. Materials

Polyether sulfone support (PES-MQ-50kDa) was obtained from Synder filtration (USA). 1, 3-phenylenediamine (MPD, >99 %), 1, 3, 5-benzenetricarbonyl trichloride (TMC, 98%), n-hexane, tetraethyl orthosilicate (TEOS, >99%), L-arginine, (3-aminopropyl) trimethoxysilane (APTMS, 97 %) and (3-glycidyloxypropyl) trimethoxysilane (GPMS, >98 %) were purchased from Sigma-Aldrich. Sodium chloride (NaCl), aqueous ammonia solution (28 %) and cyclohexane were obtained from VWR International.

4.3.2. Synthesis and surface modification of silica nanoparticles

4.3.2.1. Fabrication of silica nanoparticles

SN with an average size of 100 nm were fabricated according to a modified Stöber approach [23]. Briefly, 50 ml absolute ethanol, 0.9 ml Milli-Q water and 2.04 ml of 28% aqueous ammonia were mixed together and stirred for 10 min at room temperature. 2.9 ml of TEOS was rapidly injected to the mixture and the solution was stirred at 25 ºC for 24 h. The resulting SN were washed 3-4 times with ethanol and then redispersed and stored in ethanol.

SN with an average size of 50 nm were synthesized according to a modified approach reported by Fouilloux et al. (2010) [24]. In a typical experiment, 30 ml of 6 mM L-arginine solution was prepared. 4.65 ml cyclohexane was then added as the solvent for upper organic phase. The mixture was transferred to a pre-heated 60 ºC oil bath to warm up, followed by dropwise injection of 5.7 ml TEOS to the organic phase. The stirring rate of the solution was fixed at a low value such that the aqueous phase was well mixed while the organic phase was left intact. The reaction was

further continued for 72 h under constant stirring and heating. Finally, bluish silica solution was washed several times with Milli-Q water and stored in ethanol.

4.3.2.2. Preparation of amine and epoxy-functionalized silica nanoparticles (SN-NH_2 and SN-EPX)

A modified approach from Chang et al. (2013) was applied to functionalize the surface of nanoparticles with amine groups [25]. Typically, 100 mg of the synthesized SN were dispersed in 50 ml of ethanol and degassed with nitrogen at 80 ºC for 1 h. This was followed by the quick injection of 135 µL APTMS to the reaction vessel. The solution was then refluxed for 6 h. After centrifugation and washing with ethanol and water, amine-functionalized SN (SN-NH_2) were obtained and finally redispersed in ethanol.

Epoxy group was introduced to the surface of SN according to an established approach [26]. In brief, 100 mg of as-synthesized SN was added into 2.5 ml of 5 wt% GPMS in anhydrous toluene and then stirred for 12 h at room temperature. The epoxy functionalized silica nanoparticles (SN-EPX) were centrifuged and washed with anhydrous toluene and absolute ethanol, respectively, followed by drying under vacuum. The general schematics for preparing SN-NH_2 and SN-EPX are illustrated in Supporting Information (Fig 4S-1).

4.3.3. Fabrication of TFC and SN-TFC membranes

To obtain the TFC membranes, an ultra-thin PA layer was casted on ultrafiltration PES support membranes through interfacial polymerization. The PES support was first clamped between an acrylic plastic plate, a rubber gasket and an acrylic plastic frame. Then, 2 % (w/v) MPD aqueous solution was poured into the frame and allowed to penetrate to the PES support for 10 min. Excess MPD solution was drained and the PES support was rolled with a soft rubber roller until no visible droplets were remained on the surface of the membrane. This was followed by reassembling the holder and pouring 0.1 (w/v) % TMC hexane solution into the frame. After 1 min of reaction, excess TMC solution was disposed and the membrane was air-dried for another 1 min, followed by 10 min curing in a recirculating oven set at 60 ºC. The fabricated TFC membranes were washed with 22 °C distilled water and stored wet at 5 °C for further characterization and evaluation. The TFC membrane without any nanoparticle is called control TFC in this study.

SN-TFC membranes were fabricated exactly as described, except that different amount of nanoparticles (SN, SN-NH_2, and SN-EPX) was dispersed in MPD aqueous solution. To obtain good nanoparticle dispersions, the mixtures of nanoparticles and MPD aqueous solution were sonicated for 1 h with the temperature controlled at 22ºC exactly before the interfacial polymerization process.

4.3.4. Characterization of nanoparticles, TFC and SN-TFC membranes

Attenuated total reflectance Fourier transform infrared spectroscopy (ATR-FTIR) was performed using a NICOLET 6700 spectrometer equipped with a diamond ATR to evaluate chemical structures and functionalities of various fabricated nanoparticles and membranes.

The surface charge of the synthesized nanoparticles were measured using a Malvern Zetasizer Nano ZS (Malvern Inst. Ltd., U.K.) based on the dynamic light scattering (DLS). The samples were prepared by dispersing them in milli-Q water and the measurements were performed at room temperature.

Thermogravimetric analysis (TGA) was performed on ~ 5 mg dried nanoparticles in order to estimate the density of their surface functional groups using a TGA/DSC 2 STAR^e System from 30 °C to 800 °C at a heating rate of 10 °C/min under air. To minimise the contribution of physisorbed water during TGA analysis, an isotherm step at 120 °C was set for 1 h and the following weight loss was normalized for comparison by considering the initial weight of each sample equivalent to the remained weight of the samples at the end of this isotherm.

The morphology of fabricated nanoparticles and membranes were characterized using a scanning electron microscope (FEI Quanta 450 FEG Environmental SEM (ESEM)) at the voltage of 5-20 kV and the working distance of 10 mm. The instrument was equipped with an energy-dispersive X-ray (EDX) detector for elemental analysis. For the cross-section SEM imaging of the membrane samples, small pieces of fabric free and wet membranes were freeze-fractured in liquid nitrogen and mounted vertically on SEM stand. The prepared samples were dried overnight and sputter coated with ~ 5 nm layer of platinum using a CRESSINGTON 208 high-resolution sputter coater before imaging.

TEM images were taken on a FEI Tecnai G2 Spirit Transmission Electron Microscope at an acceleration voltage of 100 kV. Nanoparticle samples were prepared by placing one drop of ethanol dispersed nanoparticles on 200 mesh carbon coated copper grids. Membrane samples for cross-section TEM imaging were prepared by gently removing the polyester backing layer to ensure PA and PSF layers remained together. Small pieces of fabric free membranes were cut and embedded in Epon resin and cured in oven at 50 ºC overnight. From the cured samples, 60-70 nm cross sections were cut on a Leica EM UC6 Ultramicrotome and mounted on formvar and carbon coated copper grids for imaging.

An Anton Paar SurPASS Electrokinetic Analyser (Anton Paar GmbH) was used to evaluate the streaming potentials of the fabricated membranes. The membranes were mounted in the adjustable gap cell apparatus and zeta potentials were obtained from the slope of streaming potential versus pressure according to the Helmholtz-Smoluchowski approach. The measurements were carried out in 10 mM KCl solution at different pHs adjusted using 0.1 M HCl or NaOH. Four repeats were recorded and the averages in each pH were reported.

X-ray photoelectron spectroscopy (XPS) was performed on the samples using a Kratos Axis Ultra with a monochromatic aluminium x-ray running at 225 W and the characteristic energy of 1486.6 eV. The area of analysis (Iris aperture) was 0.3 mm x 0.7 mm and the electron take off angle was normal to the sample surface with analysis depth of approximately 15 nm from the sample surface. The spectra were scanned in the range of -10 to 1110 eV and the pass energy and step of 160 eV and 500 meV were used. The charge neutraliser system was used to reduce the surface charge of the samples. CasaXSP software package was eventually used to interpret the obtained survey spectra.

Contact angle measurements were performed on an Attension Theta Optical tensiometer in sessile drop mode at room temperature. The membranes were attached to clean glass slides using double sided tape and a milli-Q water droplet (1 µl) was automatically dispensed on the surface of the membranes. A FireWire camera (55 mm focus length) recorded the droplet surface contact angle equilibrated for 10 s from the time it was dispensed. Curve fitting and data analysis was then performed

using the OneAttension software. The reported contact angles were the average of at least 8 different positions on each membrane.

4.3.5. Membrane performance evaluation

A reverse osmosis cross-flow filtration setup was used to evaluate performance of the fabricated TFC/SN-TFC membranes. The effective membrane area of the filtration cell (CF042, Sterlitech) was 42 cm^2. Prior to performance evaluation, the membrane coupons were compacted with distilled water in the filtration unit for at least 16 h under the pressure of 1.5 MPa to reach equilibrium flux. The system was then operated with 15 L of 2000 mg/L NaCl solution with the pressure, temperature and concentrate flow rate controlled at 1.5 MPa, 25 ± 0.1 °C and 4 L/min respectively. The concentrate flow was recycled back to the feed tank while operating the system, and the permeate was led to a container on a digital balance for flux measurement. The schematic illustration of this lab-scale filtration setup is presented in Supporting Information (Fig 4S-2). The weight of collected permeate was recorded using a LabX Direct Software (Mettler Toledo) and the flux (J) was calculated accordingly using Equation 1. In order to evaluate salt rejection, the conductivities of collected permeate and feed water were measured using a conductometer with probe cell constant, k = 1.0 (AQUA, Cond. / pH, TPS, Australia) and were subsequently converted to equivalent salt concentrations using a pre-calibration curve shown in Supporting Information (Fig 4S-3). Salt rejection (R %) could be calculated through Equation 2.

$$J = \frac{V_P}{\mathrm{A.\,t}} \tag{1}$$

$$R\% = \left(1 - \frac{C_P}{C_F}\right) \times 100 \tag{2}$$

where J is the permeate water flux (LMH), V_P is the collected permeate volume (l), A is the active membrane surface area (m^2), t is the operation time (h), R is the salt rejection and C_P and C_F are the equivalent NaCl concentrations in collected permeate and feed water, respectively.

4.4. Results and Discussion

4.4.1. Characterization of fabricated nanoparticles

SEM micrographs and TEM images of the synthesized SN in Fig 4-1 show that both nanoparticles have uniform spherical structures with their average sizes of ~ 50 and ~ 100 nm.

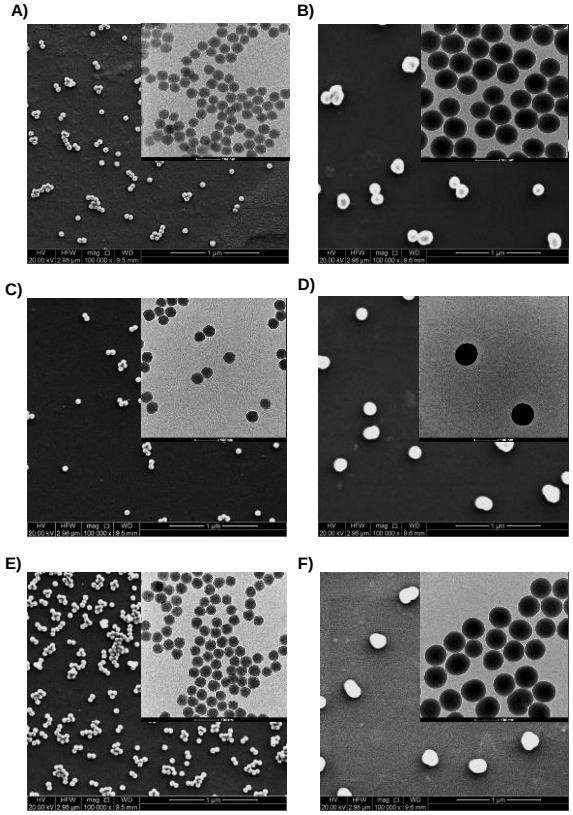

Figure 4-1 micrographs and TEM images (inset) of the different sized SN, A) SN50, B) SN100, C) SN50-NH_2, D) SN100-NH_2, E) SN50-EPX and F) SN100-EPX. Particle size and morphology are similar as the SN before modification.

The obtained nanoparticles possess surface functional OH groups and are called as SN-OH when they are discussed in general. For specific referring to the SN-OHs of each nanoparticle size, SN50 and SN100 are used in this study. Further chemical modifications were performed to introduce amine or epoxy groups to the surface of SN. SEM and TEM images of SN after surface functionalization are also presented in Fig 4-1. We found that there was no significant particle aggregation following surface functionalizing.

Thermogravimetric analysis was performed to study the surface functionality of SN and estimate the amount of their surface functional groups. To remove adsorbed

water, the dried SN were heated to 120 ºC and held for 20 min before temperature increment to 800 ºC. Fig 4-2A shows an evident weight loss for the nanoparticles after surface functionalizing in comparison with the SN50, which confirms the introduction of amine and epoxy functional groups on the surface of nanoparticles. The estimated quantity of surface functional groups based on the TGA observation was 6% and 9% for the SN50-NH_2 and SN50-EPX, respectively.

The successful surface modification of SN can be further confirmed by zeta potential measurements. The zeta potentials shown in Fig 4S-4 vary from negative to positive values for the SN-NH_2 compared with the SN-OH due to the presence of amine groups on SN-NH_2 surface. On the other hand, the SN-EPX demonstrated a lower magnitude of surface potential due to the loss of some surface hydroxyl groups. It should be noted that all zeta potential measurements (> 15 mV) indicated the high stability of these nanoparticles in aqueous solutions.

Table 4-1 shows the XPS results for the fabricated SN50 nanoparticles with different surface functionalities and the corresponding survey spectra for nanoparticles is presented in Supporting Information (Fig 4S-5). SN50 show the typical silica peaks at 532.72 eV, 284.72 eV,153.3 eV and103.22 eV corresponding to O 1s, C 1s, and Si 2s and Si 2p [27]. For the case of SN50-NH_2, N1s peak at 399.62 eV has emerged with 1.92 % composition which confirms the successful amine functionalizing. SN-EPX shows 30.60 % increase in the composition of C 1s which can be an indication of the successful epoxy functionalization.

Table 4-1 XPS results for SN50 with different surface functionalities.

Sample name	Atomic percentage of elements			
	N (%)	O (%)	C (%)	Si (%)
SN-OH	-	59.53	21.17	19.30
SN-NH_2	1.92	56.14	21.68	20.26
SN-EPX	-	54.18	27.65	18.17

4.4.2. Characterization of TFC and SN-TFC membranes

Fig 4-2B shows the ATR-FTIR spectra of PES support, control TFC membrane and a typical SN-TFC membrane. Two new bands at 1541 and 1612 cm^{-1} are emerged in the spectra of TFC and SN-TFC compared with that of the PES support, which are

associated with the vibrations of amide groups: C-N (amide II band) and N-H (aromatic amide) confirming PA fabrication [28]. Since the IR penetration depth (~ 0.5-1 µm) exceeds the thickness of the thin PA layer on the surface of PES support [28, 29], the resulting FTIR spectra from the TFC and SN-TFC membranes contain information from PA, PES and SN, where the vibration bands of SN at 955 cm^{-1} (stretching vibration of Si-OH) and 1090 cm^{-1} (asymmetric vibration of Si-O-Si) overlap with those of the PES. To further identify the overlapped peaks, detailed characterization of PA thin film without PES and SN and PA-SN thin films without PES are described in Supporting Information (Fig 4S-6).

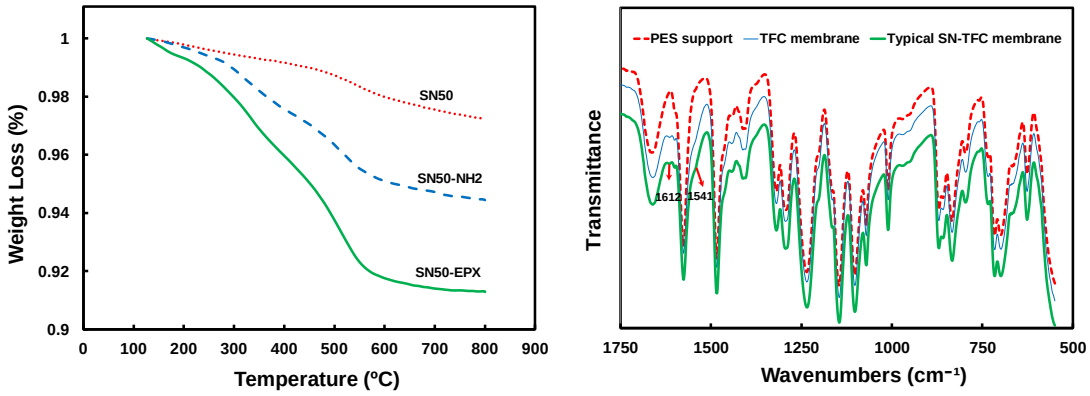

Figure 4-2 A) TGA thermograms for SN50 before and after surface functionalization, B) FTIR spectra for PES support, TFC membrane and a typical SN-TFC membrane.

Fig 4-3 presents the high and low magnification surface and cross-section SEM micrographs of the synthesized TFC and SN-TFC membranes incorporated with 0.05 wt% SN having different surface functionalities. As shown, leaf-like structure, which is the expected surface morphology of thin PA layers made from MPD and TMC monomers, is obtained for all fabricated membrane. For the 0.05 wt% SN-OH-TFC membranes, SN50-TFC membrane represents leafier surface morphology compared with SN100-TFC membrane which shows some lobe-like features (Fig 4-3 B and E). That may be due to the size difference of nanoparticles which can change the formation of surface strands. From the high magnification surface images, it is obvious that for the SN-NH_2-TFC and SN-EPX-TFC membranes, the membrane surface features are denser and the polymer strands are highly packed compared with the control TFC and SN-OH-TFC membranes (Fig 4-3 C, D, F and G). That comes from the variations in the interfacial polymerization process where surface functional groups of SN-NH_2 and SN-EPX can chemically interact with PA monomers.

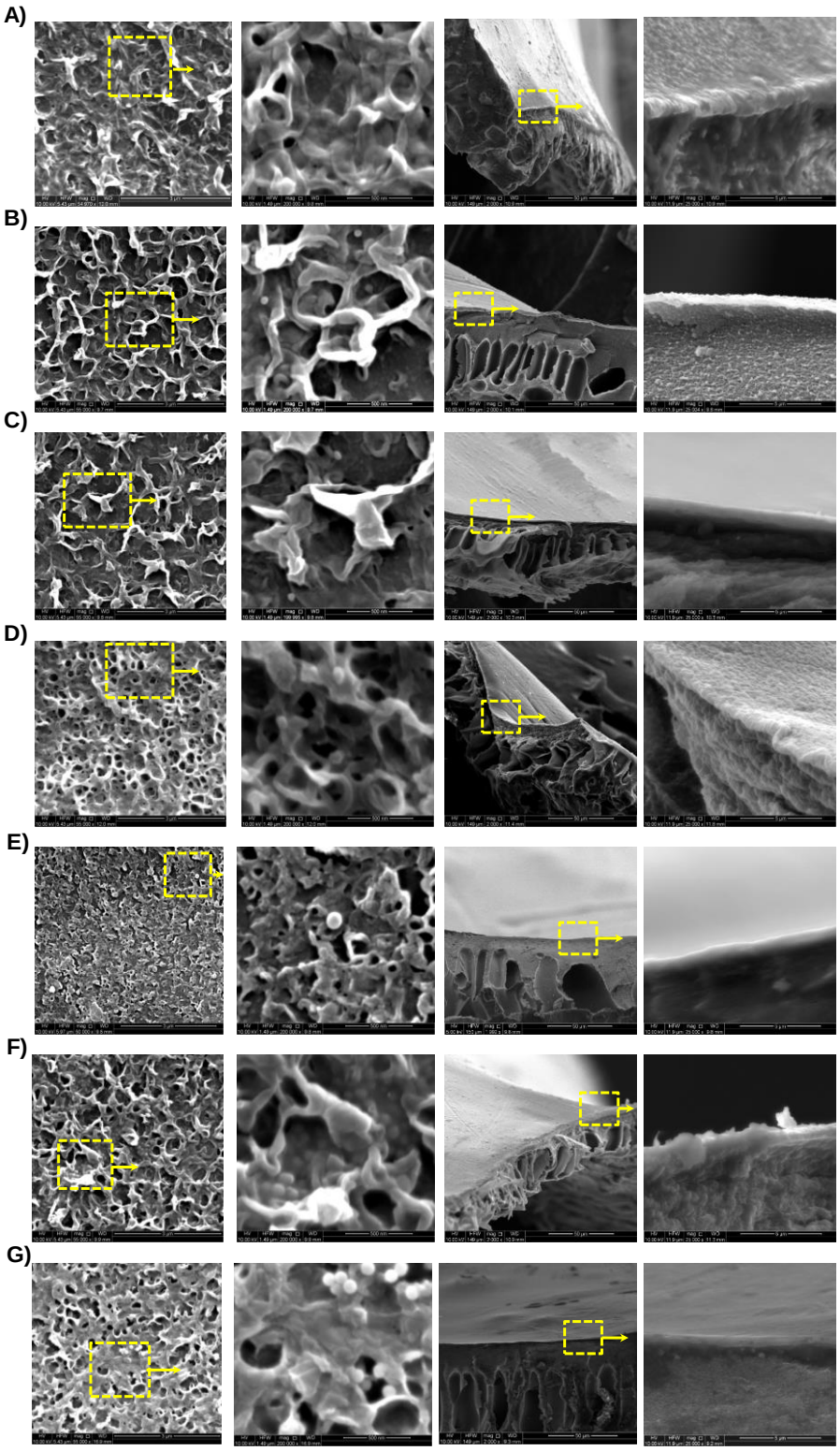

Figure 4-3 SEM micrographs of the surfaces and cross-section of different TFC/SN-TFC membranes: A) TFC, B) SN50-TFC, C) SN50-NH_2-TFC, D) SN50-EPX-TFC, E) SN100-TFC, F) SN100-NH_2-TFC, G) SN100-EPX-TFC. For the surface images, the low magnification images were taken at 55000x and the high magnification images were taken at 200000x and for the cross-section images, the low magnification images were at 2000x and the high magnification ones were at 25000x.

The high magnification images of SN-TFC membranes (Fig 4-3) show that although some variations in the leaf sizes and shapes are observed, all membranes still represent leaf-like surface morphology with emerging some nodulike features. Further, the presence of some nanoparticles with their sizes of around 50 and 100 nm on the surface of SN-TFC membranes confirms the successful incorporation of the different surface functionalized nanoparticles into the PA layers. The cross-section SEM images of the TFC/ SN-TFC membranes in Fig 4-3 show the structure of TFC membranes with PA layers having maximum thicknesses of ~ 550 nm. No significant aggregation can be observed on the surface of PA layers which confirms the fair distribution of nanoparticles. Fig 4S-7 also shows the SEM images of the SN50-TFC membranes containing different amounts of SN50. Presence of some nanoparticles on the surface is clear with emergence of some aggregated spots on the surface at higher concentrations. To further elucidate the distribution of nanoparticles in the TFC membrane, the SEM images were taken from some fractured areas on the surface of SN50-NH_2-TFC and SN100-EPX-TFC membranes as illustrated in Fig 4S-8, and such images again confirm the successful incorporation and the fair distribution of nanoparticles in the fabricated membranes.

To extensively analyse the distribution of SN in the PA thin film layers, cross-section TEM imaging was performed on SN50 with different surface functionalities, as shown in Fig 4-4. The thicknesses of PA thin film layers are in the range of 50-550 nm, which is consistent with the findings of previous studies [7, 8, 30]. TEM results further confirm that various SN have been successfully distributed in the PA thin film layer. No absolute conclusion can be made from PA cross section TEM imaging considering the inhomogeneous structure of this layer [8]. Herein, three cross-section samples were prepared from each membrane and the overall structure is shown as Fig 4-4. Considering the obtained TEM images, more SN is observed in the PA layers of SN50-NH_2-TFC and SN50-EPX-TFC membranes compared with that of SN50-TFC membrane. That can be attributed to the chemical interaction of SN-NH_2 and SN-EPX with PA monomers together with the particles' surface zeta potential. The electrostatic attraction of SN-NH_2 and negatively charged PES support [31], and the smaller electrostatic repultion between SN-EPX and PES compared with that of the SN-OH and PES makes them more prone to stay in the resulting PA layers.

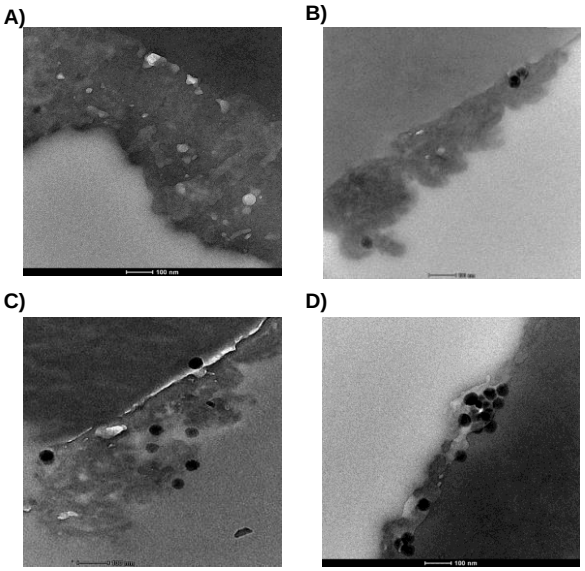

Figure 4-4 Cross-section TEM images of the A) TFC, B) SN50-TFC, C) SN50-NH_2-TFC and SN50-EPX-TFC membranes; the scale bars are 100 nm.

SN50-NH_2-TFC and SN50-EPX-TFC membranes have different thicknesses as observed in Fig 4-4. That can be due to the variation of amine/acid chloride molar ratio's after the introduction of the SN-NH_2 and SN-EPX into the PA monomer solutions. The amine/acid chloride ratio is identical to the feed MPD/TMC ratio for SN-OH-TFC; but this ratio may slightly increase for the SN-NH_2-TFC due to the introduction of more -NH_2 groups. Conversely, SN-EPX can consume some -NH_2 groups of MPD monomer and slightly decrease this ratio. Generally, the interfacial polymerization of MPD and TMC consists of two main stages: an extremely fast stage that forms an ultrathin dense core PA layer in the oil-water interface and a slow growth stage making a slightly thicker PA layer by diffusion of monomers (mainly MPD) [39]. Decreasing the MPD/TMC molar ratio could make a denser core PA layer while reducing the thickness of the PA layer formed during diffusion stage and vice versa [39-41]. Considering these theories, the SN-NH_2-TFC could have a less dense core layer but thicker secondary PA layer formed by diffusion and the SN-EPX-TFC could have denser core layer but thinner secondary PA layer. Thus, the overal thickness of SN-NH_2-TFC membrane can be higher than that of the SN-EPX-TFC membrane which is consistent with our TEM results.

Streaming potential measurements were performed to understand the surface electrical double layers for two selected SN-TFC membranes. Fig 4-5A shows the pH dependant zeta potentials of the fabricated TFC and SN50-NH_2-TFC membranes

measured using tangential streaming potential (TSP) method. For the TFC membranes, negative surface potentials are observed in the whole pH range. It is expected to observe the negative surface zeta potentials of TFC membranes due to the partially or incompletely interfacial polymerization and the hydrolysis of acyl chlorides. The pK_a of the carboxyl groups is 4.5-5.0. With increasing pH, the deprotonation results in the increasing negative surface potentials of the membranes. The surface potentials shift to a less negative value at low pHs due to the protonation of carboxyl groups, but surface potentials cannot shift to positive. That may be due to the presence of less unreacted MPD on the surface of fabricated membranes [11]. At the same time, the average surface zeta potentials of the SN50-NH_2-TFC membranes are less negative than that of the control TFC membranes in the whole pH range. This result appears to be consistent with the presence of amine functionalized nanoparticles (Fig 4-5A), again indicating the successful incorporation of nanoparticles into the resulting membranes.

XPS analysis was performed to give an estimation of the membranes' cross-linking density by measuring the elemental composition of the TFC and TFN membranes. The structure of cross-linked PA has one excess amide group compared with the linear PA while the linear PA possesses one more carboxylic acid. Hence, a higher N/O ratio can indicate a higher cross-linking density of the PA layer [32-34]. However, since the incorporation of nanoparticles induces more C and O in all cases and more N in the case of SN-NH_2, N/O ratio must be modified to better estimate the cross-linking density. XPS data in Table 4-1 can be used to correct the elemental composition of each element and calculate the corrected N/O ratio which is noted as *N/O. The calculation can be performed by considering the composition of captured Si element for each particular TFN membrane. Table 4-2, shows the initially obtained values for each constituent element and their corresponding *N/O ratios.

Table 4-2 XPS results for TFC membrane and TFN membranes incorporated with different surface functionalized SN50.

Sample name	Atomic percentage of elements				
	N (%)	O (%)	C (%)	Si (%)	*N/O
TFC	9.89	16.12	73.71	-	0.61
SN50-TFC	8.97	16.51	73.92	0.58	0.60
SN50-NH_2-TFC	9.58	16.85	72.59	0.96	0.67
SN50-EPX-TFC	9.19	17.09	72.44	1.26	0.69

Lower *N/O ratio is obtained for the SN50-TFC membrane compared with the TFC membrane which suggests the slight decrease of the cross-linking density of the PA layer after SN50 incorporation. That shows the unmodified nanoparticles alter the PA bulk structure and is consistent with the findings of other studies [7, 8, 34]. However, the *N/O ratio have increased after the introduction of SN50-NH_2 and SN-50-EPX suggesting a higher cross-linking density for these membranes. That can be due to the chemical interaction of the introduced functional nanoparticles with the PA layer and could be beneficial for the stability of nanoparticles in the PA structure.

Contact angle is a macroscopic manifestation of molecular level surface-water interactions and can be a representative of the amount of surface affinity towards water or its hydrophilicity [35]. It is calculated through the average of tangent lines to both sides of dispensed water droplets on the surface of the membrane. Fig 4-5B presents the contact angles for all fabricated membranes, in which the reported values are the average of at least 8 random points on the surface of each membrane. As presented, the contact angle drops with increasing the concentration of SN in the PA thin film layer. Further reduction in contact angle is observed in amine and epoxy functionalized SN-TFC membranes. No matter SN50 or SN100, similar trends are observed for the contact angles of TFC membranes incorporated with nanoparticles having different surface functionalities. Incorporation of SN100s results the membranes to be more hydrophilic. It has been established that high hydrophilicity of TFC/TFN membranes is in favour of water flux during the desalination process. Therefore, the observed decrease in contact angles for all SN-TFC membranes compared with the control TFC membrane can be deemed as an advantage for improving the membranes' end-use performance.

4.4.3. Performance evaluation of TFC and SN-TFC membranes

4.4.3.1. Effect of nanoparticle concentration

Fig 4-5C shows the performance evaluations for the TFC membranes incorporated with different concentrations of SN50. Previous studies on the TFC desalination performance evaluation indicate that the measured permeability and salt rejection are significantly influenced by the structure and properties of supporting layers and fabrication procedure (e.g. manual/ automated coating) [9, 29, 36, 37]. TFC membranes are usually made by polysulfune ultrafiltration support. In our study, due

to the different structure of applied PES support, shown in Fig 4S-9, and also manually coating procedure, performance results cannot be compared with those membranes that have been manufactured by polysulfone supports or have been automatically coated. TFC membranes with salt rejections in the similar range to this study have been reported by other researchers [9, 38]. Since the purpose of this study is to evaluate the structure-performance correlation of the TFC membranes incorporated with different surface functionalized nanoparticles, the relative performance values obtained at the same fabrication and evaluation proedure are valid rather than the absolute values.

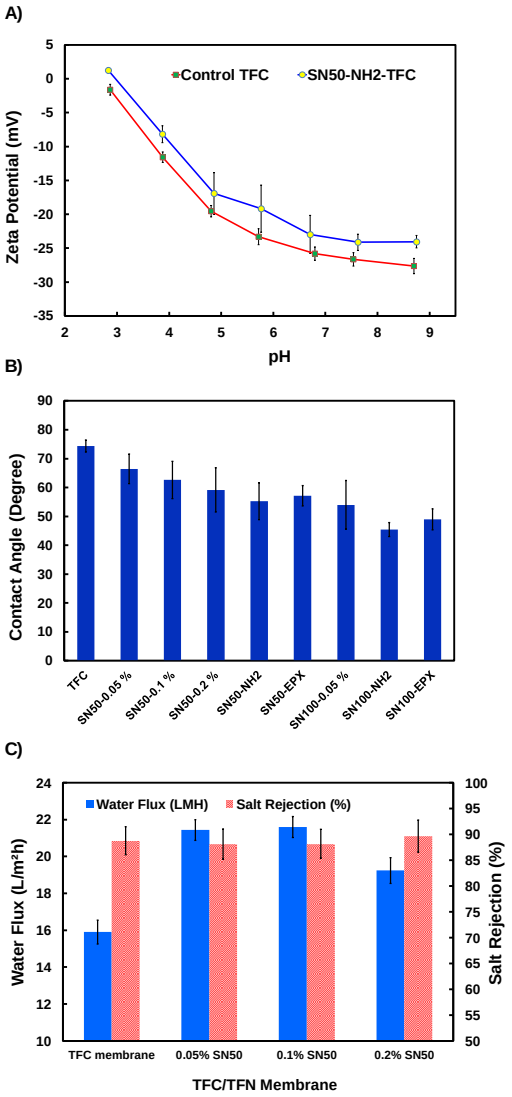

Figure 4-5 A) Comparison on the streaming potential measurements for the TFC membranes with and without SN50-NH_2, B) Contact angles for the TFC membranes incorporated with different concentrations of SN50 and 0.05 wt% SN-NH_2 and SN-EPX, C) Performance evaluation for various TFC membranes incorporated with different concentrations of SN50.

As shown in Fig 4-5C, all membranes display similar salt rejection capability; however, the incorporation of hydrophilic SN50 improves water permeability across the membarne with almost 40% enhancement for the membranes with 0.1 wt% SN50 incorporation in comparison with the control TFC membrane. This observation is in-line with the contact angle results, where the higher hydrophilicity of membranes containing SN adds to the membranes' water affinity and permeation. However, incorporation of nanomaterials into the membranes at a concentration higher than a threshold value can block water permeation path and enhance mass transfer resistance. The lower water flux for the 0.2 wt% SN50-TFC membrane might be attributed to this fact. Considering the promising water flux improvement and minor salt rejection impact of the fabricated membranes, 0.05 wt% was chosen as the optimum SN incorporation concentration for further study.

4.4.3.2. Effect of nanoparticle surface functionality

MPD monomer have -NH_2 functional groups while TMC monomer have -COCl functional groups. Interaction of these functional groups in the interface of MPD aqueous and TMC organic solutions (on the PES support) results in the formation of TFC membranes with a thin PA selective layer. To fabricate SN-TFC membranes, SN can be either dispersed in aqueous or organic monomer solutions. If the SN can be conjugated with the PA through chemical interaction with either of these monomers, the resulting SN-TFC membranes is expected to have more stable structure and excellent durability. Hence, we designed SN with two different surface functional groups: epoxy and amine, where epoxy groups of SN-EPX can interact with the -NH_2 groups of MPD monomer while amine groups of SN-NH_2 can interact with the -COCl groups of TMC monomer. After introducing functionalized SN to TFC membranes, the desalination performance of the fabricated membranes was evaluated subject to the sizes and surface functionalities of the SN.

Fig 4-6A shows that all SN-TFC membranes demonstrate a higher water flux compared with the control TFC membrane which can be due to the increase in their surface hydrphilicity. The highest water flux is given by the SN-OH-TFC membranes followed by the SN-EPX-TFC and SN-NH_2-TFC membranes. The membranes have almost similar salt rejections with an slight improvement for the amine and epoxy functionalized samples. No matter which size of nanoparticles is

used, the performance results follow a similar trend. The observed water flux and salt rejection values can be explained through the higher crosslinking density for the PA layers of SN-NH_2-TFC and SN-EPX-TFC membranes compared with that of the SN-OH-TFC and TFC membranes as evidenced by XPS analysis. For SN-NH_2 and SN-EPX, the SN can be entrapped into the PA layer through covalent bond formation ensuring higher stability for the resulting SN-TFC membranes which coincides with more compact structures. However, SN-OH have no interaction with the PA monomers making a loose PA structure with the possibility of nanoparticle leakage after long-time high pressure operation.

The other possibility contributing to this performance variation is the change of amine/acid chloride molar ratio by introducing functionalized nanoparticles that can change the dense core and loose secondary PA layers [39-41]. TEM results showed overall thicker PA layer for the SN50-NH_2-TFC membrane compared with SN50-EPX-TFC membrane. That could contribute to the slightly lower water flux and higher salt rejection of SN-NH_2-TFC compared with SN-EPX-TFC membranes. However, the effect of chemical interaction of SN-NH_2 and SN-EPX with PA on the overall permeation behaviour of membranes may be higher compared with this molar ratio influence due to the initially large -NH_2/-COCl molar ratio in the PA fabrication stage and the small ratio of SN/MPD in the MPD monomer solution. That can be the reason why both SN-NH_2-TFC and SN-EPX-TFC have almost similar trend in terms of water flux and salt rejection variation compared with SN-OH-TFC and control TFC membranes.

Fig 4-6B shows the normalized salt rejection curves for the membranes during a 6 h operation against 2000 ppm NaCl solution, where the data are the average of three repeats for each membrane and each point is the ratio of salt rejection at certain time normalized by the initial salt rejection.

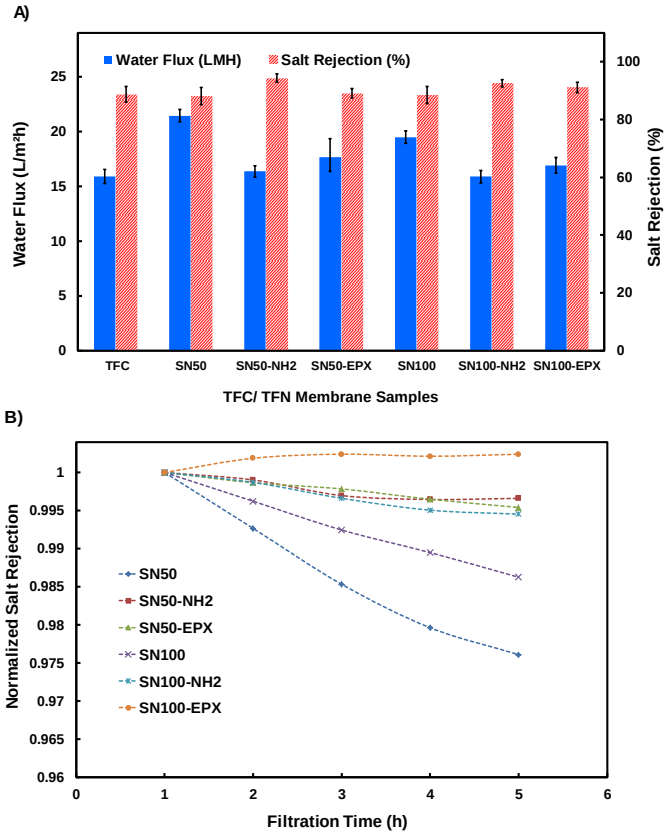

Figure 4-6 A) Desalination performance evaluation for the TFC membranes incorporated with various SN with different surface functionalities, B) Normalized salt rejection for the fabricated SN-TFC membranes vs. filtration time.

The salt rejection slightly decrease for all membranes with time. However, this trend is minimal for the SN-NH_2-TFC and SN-EPX-TFC membranes compared with SN-OH-TFC membranes. The reason could be again the chemical bond formation between SN-NH_2 and SN-EPX with the PA and the more compact structure of the resulting TFN membranes. However, SN-OH can only physically bond with the PA and might be lost under high pressure process generating defects on the SN-OH-TFC. The small salt rejection variability observed for the SN-NH_2-TFC and SN-EPX-TFC membranes confirms the higher performance stability of these membranes compared with SN-OH-TFC membranes which can be advantageous for their longer optimum performance.

4.5. Conclusions

In this study, new TFN (SN-TFC) membranes incorporated with various surface functionalized SN (amine, epoxy or hydroxyl groups) have been developed. The main focus is to understand the interaction of different SN and PA thin film layer in

the fabricated TFN membranes, and their influence on the membranes' physicochemical properties and overall desalination performance. Differently sized SN (~ 50 and ~ 100 nm) with varied surface functional groups were fabricated and could be successfully incorporated in the thin film PA layer of the resulting TFN membranes as evidenced by various characterizations (streaming potential, SEM, TEM, and FTIR). Water flux increases up to around 40 % by incorporating 0.1 wt % SN50 to the TFC membrane with minimal influence on salt rejection capability. Slightly higher water flux with comparable salt rejection and lower variation in surface morphology is observed for the SN50-TFC membranes in comparison with the SN100-TFC membranes. The high crosslinking density of SN-NH_2 and SN-EPX with the TFC membranes results in more stable salt rejections in these membranes. Desalination performance evaluation of the fabricated membranes show that no matter which functional group is present on SN, the resulting SN-TFC membranes have higher water flux and comparable or higher salt rejection compared with the control TFC membrane. Overall, covalent bond formation between SN-NH_2, SN-EPX and PA will improve the stability of SN inside the PA and the performance stability of the resulting SN-TFC membranes.

References

[1] L.Y. Ng, A.W. Mohammad, C.P. Leo, N. Hilal, Polymeric membranes incorporated with metal/metal oxide nanoparticles: A comprehensive review, Desalination, 308 (2013) 15-33.

[2] M. Elimelech, W.A. Phillip, The future of seawater desalination: energy, technology, and the environment, Science, 333 (2011) 712-717.

[3] K.P. Lee, T.C. Arnot, D. Mattia, A review of reverse osmosis membrane materials for desalination—Development to date and future potential, Journal of Membrane Science, 370 (2011) 1-22.

[4] G.D. Kang, Y.M. Cao, Development of antifouling reverse osmosis membranes for water treatment: A review, Water Research, 46 (2012) 584-600.

[5] S.G. Kim, D.H. Hyeon, J.H. Chun, B.H. Chun, S.H. Kim, Nanocomposite poly(arylene ether sulfone) reverse osmosis membrane containing functional zeolite nanoparticles for seawater desalination, Journal of Membrane Science, 443 (2013) 10-18.

[6] H. Zhao, S. Qiu, L. Wu, L. Zhang, H. Chen, C. Gao, Improving the performance of polyamide reverse osmosis membrane by incorporation of modified multi-walled carbon nanotubes, Journal of Membrane Science, 450 (2014) 249-256.

[7] B.H. Jeong, E.M.V. Hoek, Y. Yan, A. Subramani, X. Huang, G. Hurwitz, A.K. Ghosh, A. Jawor, Interfacial polymerization of thin film nanocomposites: A new concept for reverse osmosis membranes, Journal of Membrane Science, 294 (2007) 1-7.

[8] M.L. Lind, A.K. Ghosh, A. Jawor, X. Huang, W. Hou, Y. Yang, E.M.V. Hoek, Influence of zeolite crystal size on zeolite-polyamide thin film nanocomposite membranes, Langmuir, 25 (2009) 10139-10145.

[9] G.L. Jadav, P.S. Singh, Synthesis of novel silica-polyamide nanocomposite membrane with enhanced properties, Journal of Membrane Science, 328 (2009) 257-267.

[10] L. Jin, W. Shi, S. Yu, X. Yi, N. Sun, C. Ma, Y. Liu, Preparation and characterization of a novel PA-SiO_2 nanofiltration membrane for raw water treatment, Desalination, 298 (2012) 34-41.

[11] A. Tiraferri, Y. Kang, E.P. Giannelis, M. Elimelech, Highly hydrophilic thin-film composite forward osmosis membranes functionalized with surface-tailored nanoparticles, ACS Applied Materials & Interfaces, 4 (2012) 5044-5053.

[12] H. Wu, B. Tang, P. Wu, Optimizing polyamide thin film composite membrane covalently bonded with modified mesoporous silica nanoparticles, Journal of Membrane Science, 428 (2013) 341-348.

[13] R.X. Zhang, L. Braeken, P. Luis, X.L. Wang, B. Van der Bruggen, Novel binding procedure of TiO_2 nanoparticles to thin film composite membranes via self-polymerized polydopamine, Journal of Membrane Science, 437 (2013) 179-188.

[14] D. Emadzadeh, W.J. Lau, T. Matsuura, A.F. Ismail, M. Rahbari-Sisakht, Synthesis and characterization of thin film nanocomposite forward osmosis membrane with hydrophilic nanocomposite support to reduce internal concentration polarization, Journal of Membrane Science, 449 (2014) 74-85.

[15] J. Yin, Y. Yang, Z. Hu, B. Deng, Attachment of silver nanoparticles (AgNPs) onto thin-film composite (TFC) membranes through covalent bonding to reduce membrane biofouling, Journal of Membrane Science, 441 (2013) 73-82.

[16] Y. Liu, E. Rosenfield, M. Hu, B. Mi, Direct observation of bacterial deposition on and detachment from nanocomposite membranes embedded with silver nanoparticles, Water Research, 47 (2013) 2949-2958.

[17] F. Perreault, M.E. Tousley, M. Elimelech, Thin-film composite polyamide membranes functionalized with biocidal graphene oxide nanosheets, Environmental Science & Technology Letters, 1 (2014) 71-76.

[18] L. He, L.F. Dumée, C. Feng, L. Velleman, R. Reis, F. She, W. Gao, L. Kong, Promoted water transport across graphene oxide–poly(amide) thin film composite membranes and their antibacterial activity, Desalination, 365 (2015) 126-135.

[19] H.R. Chae, J. Lee, C.H. Lee, I.C. Kim, P.K. Park, Graphene oxide-embedded thin-film composite reverse osmosis membrane with high flux, anti-biofouling, and chlorine resistance, Journal of Membrane Science, 483 (2015) 128-135.

[20] C.F. de Lannoy, E. Soyer, M.R. Wiesner, Optimizing carbon nanotube-reinforced polysulfone ultrafiltration membranes through carboxylic acid functionalization, Journal of Membrane Science, 447 (2013) 395-402.

[21] L. Dumée, J. Lee, K. Sears, B. Tardy, M. Duke, S. Gray, Fabrication of thin film composite poly(amide)-carbon-nanotube supported membranes for enhanced performance in osmotically driven desalination systems, Journal of Membrane Science, 427 (2013) 422-430.

[22] H. Yamada, C. Urata, Y. Aoyama, S. Osada, Y. Yamauchi, K. Kuroda, Preparation of colloidal mesoporous silica nanoparticles with different diameters and their unique

degradation behavior in static aqueous systems, Chemistry of Materials, 24 (2012) 1462-1471.

[23] W. Stöber, A. Fink, J. Colloid Interface Sci., 26 (1968) 62.

[24] S. Fouilloux, A. Désert, O. Taché, O. Spalla, J. Daillant, A. Thill, SAXS exploration of the synthesis of ultra monodisperse silica nanoparticles and quantitative nucleation growth modeling, Journal of Colloid and Interface Science, 346 (2010) 79-86.

[25] B. Chang, D. Chen, Y. Wang, Y. Chen, Y. Jiao, X. Sha, W. Yang, Bioresponsive controlled drug release based on mesoporous silica nanoparticles coated with reductively sheddable polymer shell, Chemistry of Materials, 25 (2013) 574-585.

[26] J. Lu, W. Wei, L. Yin, Y. Pu, S. Liu, Flow injection chemiluminescence immunoassay of microcystin-LR by using PEI-modified magnetic beads as capturer and HRP-functionalized silica nanoparticles as signal amplifier, Analyst, 138 (2013) 1483-1489.

[27] B. Deng, J. Yin, Thin-film nano-composite membrane with mesoporous silica nanoparticles, in, Google Patents, 2014.

[28] V. Freger, J. Gilron, S. Belfer, TFC polyamide membranes modified by grafting of hydrophilic polymers: an FT-IR/AFM/TEM study, Journal of Membrane Science, 209 (2002) 283-292.

[29] A. Prakash Rao, S.V. Joshi, J.J. Trivedi, C.V. Devmurari, V.J. Shah, Structure–performance correlation of polyamide thin film composite membranes: effect of coating conditions on film formation, Journal of Membrane Science, 211 (2003) 13-24.

[30] A.K. Ghosh, B.H. Jeong, X. Huang, E.M.V. Hoek, Impacts of reaction and curing conditions on polyamide composite reverse osmosis membrane properties, Journal of Membrane Science, 311 (2008) 34-45.

[31] S. Salgın, Effects of ionic environments on bovine serum albumin fouling in a cross-flow ultrafiltration system, Chemical Engineering & Technology, 30 (2007) 255-260.

[32] S.H. Kim, S.Y. Kwak, T. Suzuki, Positron Annihilation spectroscopic evidence to demonstrate the flux-enhancement mechanism in morphology-controlled thin-film-composite (TFC) membrane, Environmental Science & Technology, 39 (2005) 1764-1770.

[33] J. Duan, Y. Pan, F. Pacheco, E. Litwiller, Z. Lai, I. Pinnau, High-performance polyamide thin-film-nanocomposite reverse osmosis membranes containing hydrophobic zeolitic imidazolate framework-8, Journal of Membrane Science, 476 (2015) 303-310.

[34] S.Y. Kwak, S.H. Kim, S.S. Kim, Hybrid organic/inorganic reverse osmosis (RO) membrane for bactericidal anti-fouling. 1. preparation and characterization of TiO_2 nanoparticle self-assembled aromatic polyamide thin-film-composite (TFC) membrane, environmental science & technology, 35 (2001) 2388-2394.

[35] S. Romero-Vargas Castrillón, X. Lu, D.L. Shaffer, M. Elimelech, Amine enrichment and poly(ethylene glycol) (PEG) surface modification of thin-film composite forward osmosis membranes for organic fouling control, Journal of Membrane Science, 450 (2014) 331-339.

[36] A. Prakash Rao, N.V. Desai, R. Rangarajan, Interfacially synthesized thin film composite RO membranes for seawater desalination, Journal of Membrane Science, 124 (1997) 263-272.

[37] G.D. Vilakati, M.C.Y. Wong, E.M.V. Hoek, B.B. Mamba, Relating thin film composite membrane performance to support membrane morphology fabricated using lignin additive, Journal of Membrane Science, 469 (2014) 216-224.

[38] A.K. Ghosh, E.M.V. Hoek, Impacts of support membrane structure and chemistry on polyamide–polysulfone interfacial composite membranes, Journal of Membrane Science, 336 (2009) 140-148.

[39] V. Freger, Nanoscale heterogeneity of polyamide membranes formed by interfacial polymerization, Langmuir, 19 (2003) 4791-4797.

[40] A.V. Berezkin, A.R. Khokhlov, Mathematical modeling of interfacial polycondensation, Journal of Polymer Science Part B: Polymer Physics, 44 (2006) 2698-2724.

[41] W. Xie, G.M. Geise, B.D. Freeman, H.S. Lee, G. Byun, J.E. McGrath, Polyamide interfacial composite membranes prepared from m-phenylene diamine, trimesoyl chloride and a new disulfonated diamine, Journal of Membrane Science, 403–404 (2012) 152-161.

TOC:

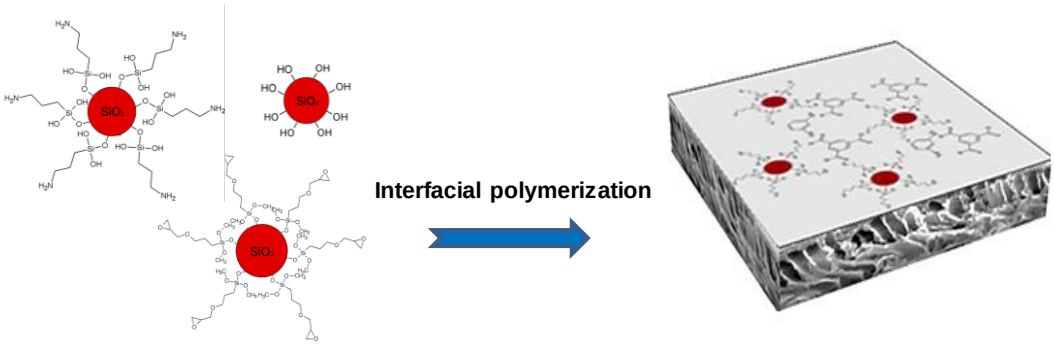

Functionalized nanoparticles **TFN membranes with enhanced performance**

4.6. Supporting Information

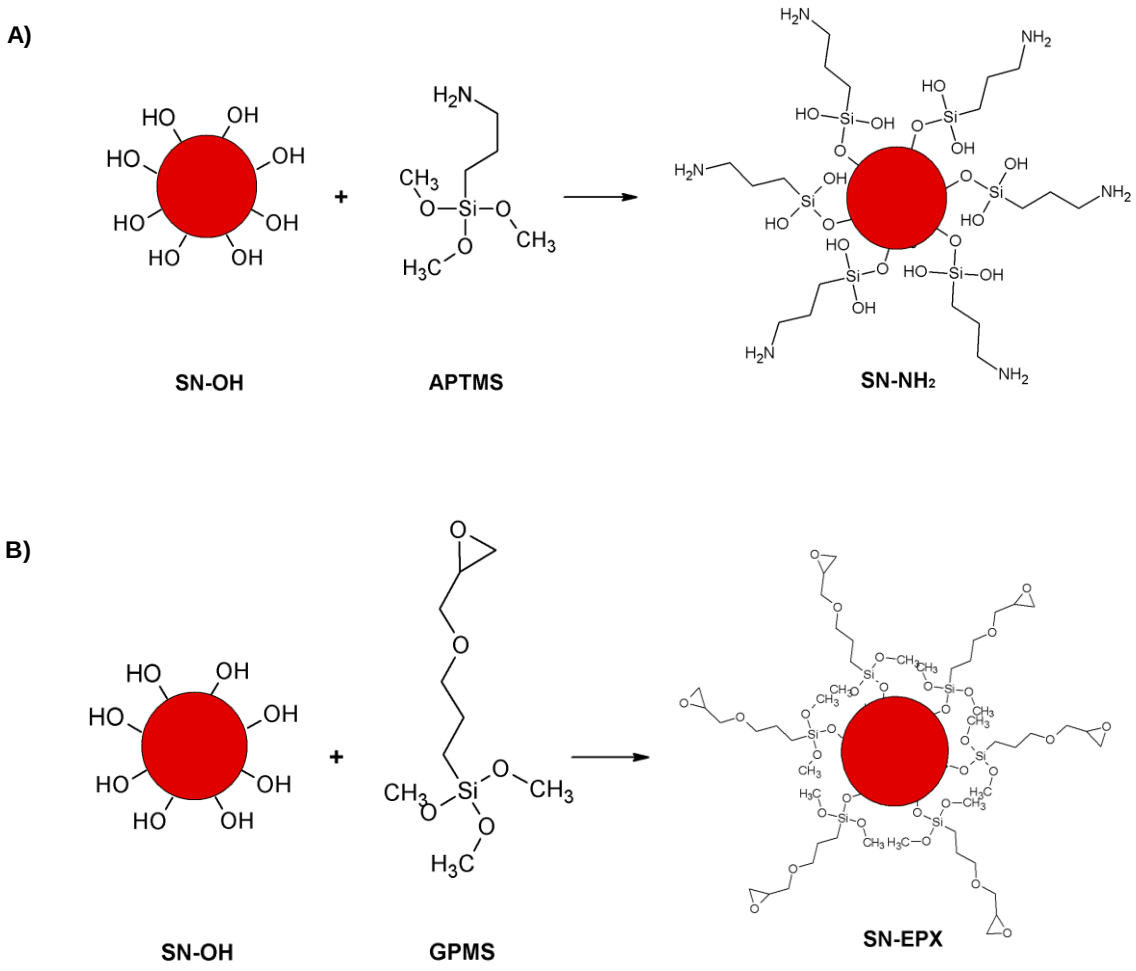

Fig 4S-1 General strategy to fabricate: A) SN-NH_2 and B) SN-EPX.

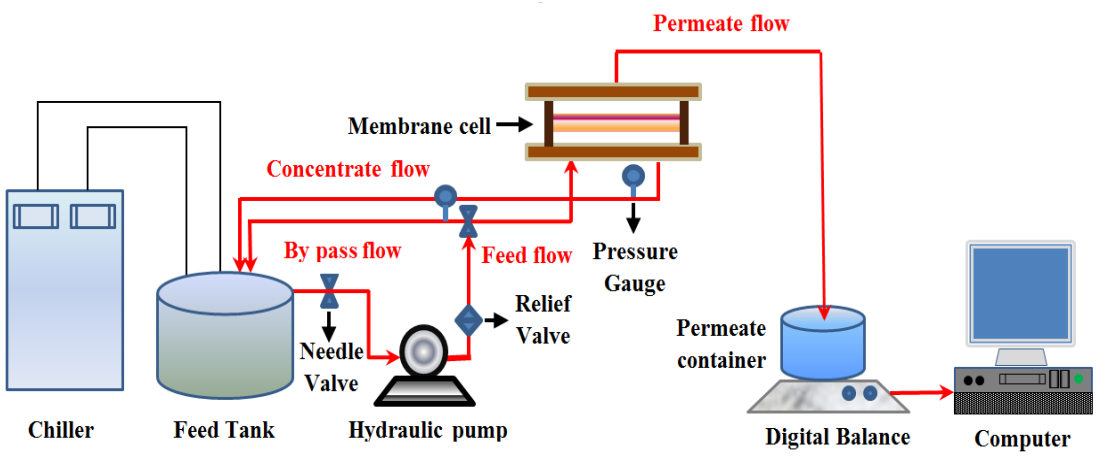

Fig 4S-2 The schematic representation of lab-scale desalination setup.

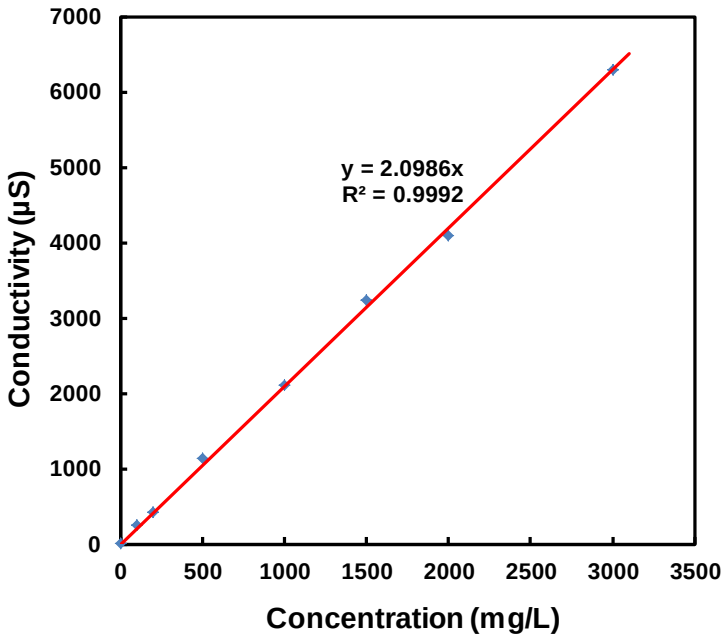

Fig 4S-3 Calibration curve between conductivity and NaCl concentration.

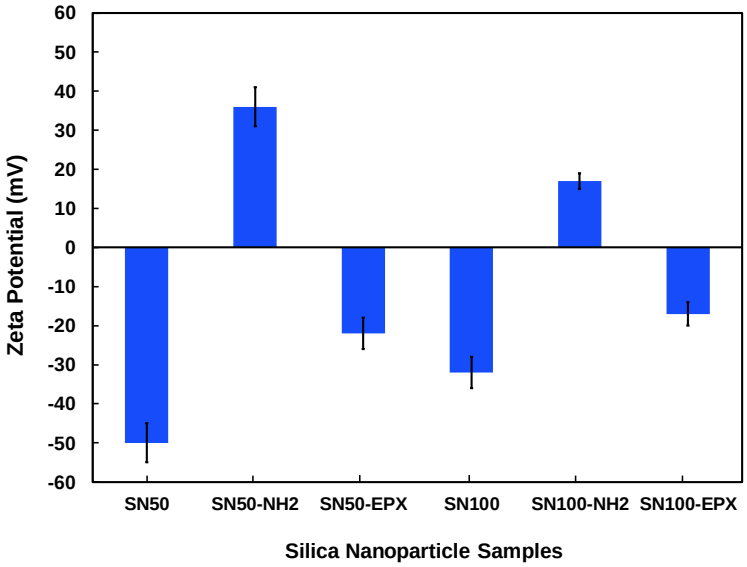

Fig 4S-4 Changes in the zeta potential values of SN samples before and after surface functionalizing with amine or epoxy functional groups.

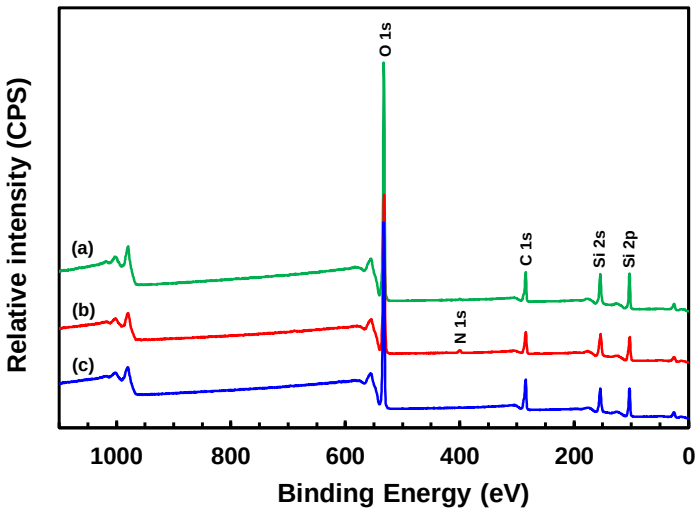

Fig 4S-5 XPS spectra for (a) SN50, (b) Sn50-NH_2 and (c) SN50-EPX.

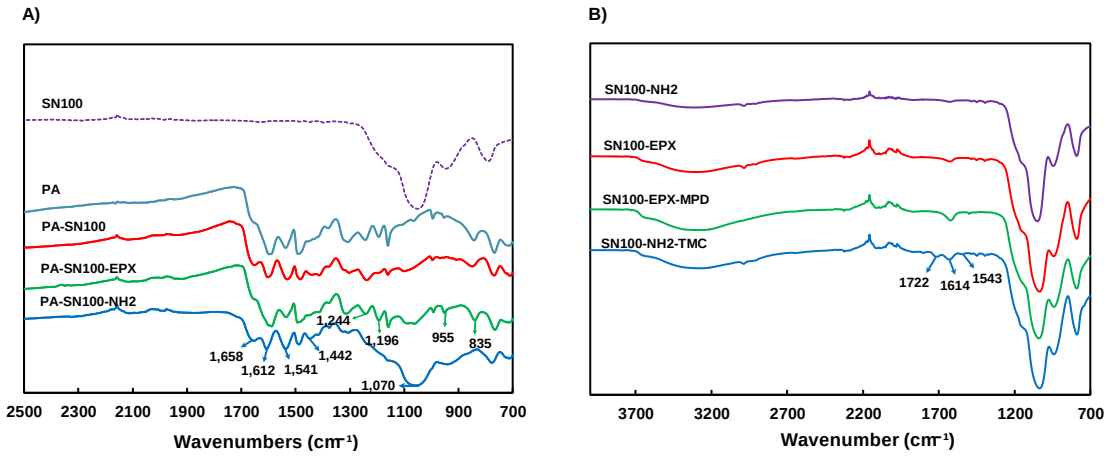

Fig 4S-6 FTIR spectra for: A) SN100, PA and PA-SN100 with hydroxyl, epoxy and amine functionalized SN, B) Functionalized SN with and without reacting with PA monomers.

The FTIR of PA-SN thin films shown in Fig 4-S6A confirm the presence of strong SN bands for all samples at 955 cm^{-1} (stretching vibration of Si-OH) and 1090 cm^{-1} (asymmetric vibration of Si-O-Si). For the PA-SN-NH_2 and PA-SN-EPX, distinguishing FTIR spectra are evident in comparison with the PA-SN. This can be associated with the covalent bond formation between modified SN and PA network. For the PA-SN-EPX, the peaks at around 835 and 1196 cm^{-1} correspond to the Si-OCH_3 and the peak at 1244 cm^{-1} is ascribed to the symmetric stretching of epoxy [1]. The characteristic bands associated with amine group of SN-NH_2 reaction with TMC (1540, 1612 and 1658 cm^{-1}) also partially overlap with PA amide bands. However, a strong band at 1442 cm^{-1} for the SN-NH_2 could be associated with stretching C-N amide and bending vibration of C-H bond in the methyl groups of APTMS, indicating the presence of SN-NH_2 in the resulting hybrids. Moreover, the reaction of TMC with SN-NH_2 can be further confirmed by the formation of amide bands between functionalized SN and TMC (Fig 4-S6B).

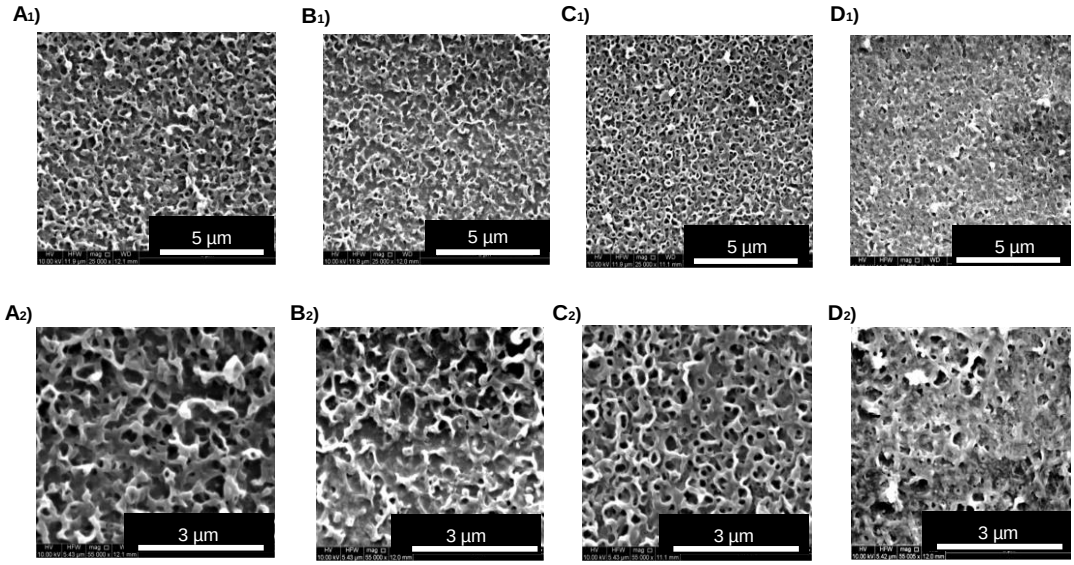

Fig 4S-7 SEM micrographs for the TFC membranes containing different amounts of SN50: A_1, A_2) 0%, B_1, B_2) 0.05%, C_1, C_2) 0.1% and D_1, D_2) 0.2%. As presented, the membrane surfaces gets leafier by increasing the nanoparticle concentration up to 0.1 % and some small aggregates are presented on the surface of 0.1% nanoparticle incorporated TFC membranes. However, for the 0.2%, a coarser surface with some visibly large aggregation of particles on the surface is observed. Images on the top are at 25000x magnification and images on the bottom are for the same membranes at 55000x magnification.

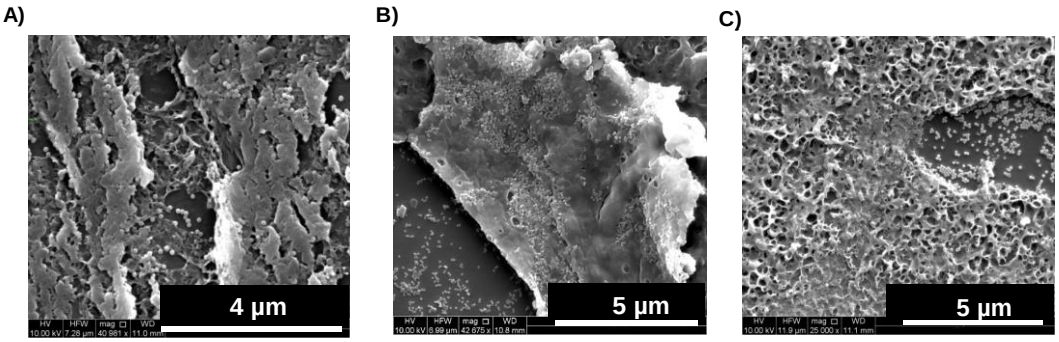

Fig 4S-8 SEM images of the fractured areas on A, B) SN50-NH_2-TFC membranes and C) SN100-EPX-TFC membranes confirming incorporation and fair distribution of nanoparticles in thin film PA layers.

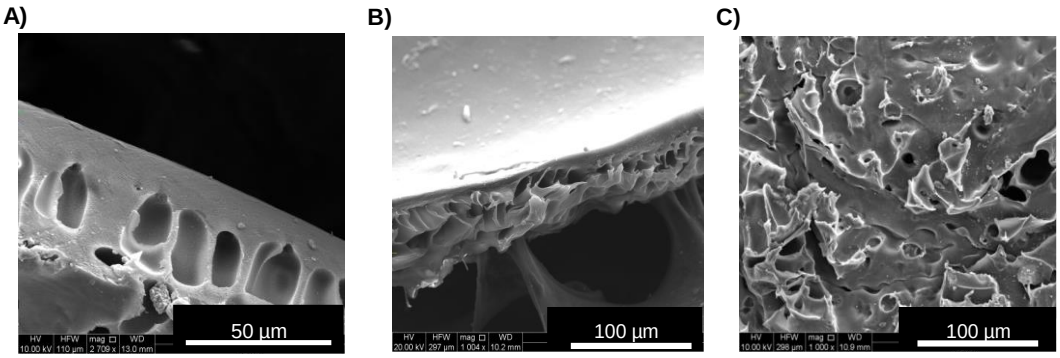

Fig 4S-9 SEM micrographs of the PES support A) cross-section before compaction, B) cross-section after compaction for16 h at 15 bar and 25 ºC and C) bottom view after removing non-woven fabric from PES.

As seen in Fig 4S-9, the surface layer of applied PES support is quite dense. This can contribute to the lower performance of the resulting TFC/SN-TFC membranes compared with commercial desalination membranes or fabricated membranes in some other studies mainly using microporous polysulfune as the supporting material. Membranes made through automated machine coating are expected to have higher water flux and salt rejection due to the applied automatically controlled fabrication strategy and higher porosity of supporting layer [2]. The manually coated membranes usually have a very thicker barrier layer compared with machine coated membranes and as flux is directly proportional to the thickness of selective layer, they show lower water flux. Therefore, salt rejection can get affected through the relatively lower water to salt diffusivity resulted from thick membranes [2, 3]. Moreover, the relatively dense surface layer of the PES support used in this study might also result in the lower saturation of the PES surface with the MPD monomer and slightly lower salt rejection for these membranes compared with some reported membrane in the literature.

It should be noted that salt rejection values lower than 98% are quite common in the literature and can be correlated to the structure of the support membrane and hand casting procedure as discussed [4-7]. However, since the main objective in this study is to investigate the interaction of nanoparticles with the PA structure and their relative influence on the properties of PA and the overall performance of resulting TFN membranes, obtained performances can be used as reference and justify our comparison purpose.

References:

[1] S. Peng, Z. Zeng, W. Zhao, H. Li, Q. Xue, X. Wu, Synergistic effect of thiourea in epoxy functionalized silica sol–gel coating for copper protection, Surface and Coatings Technology, 213 (2012) 175-182.

[2] G.L. Jadav, P.S. Singh, Synthesis of novel silica-polyamide nanocomposite membrane with enhanced properties, Journal of Membrane Science, 328 (2009) 257-267.

[3] A. Prakash Rao, S.V. Joshi, J.J. Trivedi, C.V. Devmurari, V.J. Shah, Structure–performance correlation of polyamide thin film composite membranes: effect of coating conditions on film formation, Journal of Membrane Science, 211 (2003) 13-24.

[4] A.K. Ghosh, E.M.V. Hoek, Impacts of support membrane structure and chemistry on polyamide–polysulfone interfacial composite membranes, Journal of Membrane Science, 336 (2009) 140-148.

[5] A. Prakash Rao, N.V. Desai, R. Rangarajan, Interfacially synthesized thin film composite RO membranes for seawater desalination, Journal of Membrane Science, 124 (1997) 263-272.

[6] P.S. Singh, S.V. Joshi, J.J. Trivedi, C.V. Devmurari, A.P. Rao, P.K. Ghosh, Probing the structural variations of thin film composite RO membranes obtained by coating polyamide over polysulfone membranes of different pore dimensions, Journal of Membrane Science, 278 (2006) 19-25.

[7] M.L. Lind, A.K. Ghosh, A. Jawor, X. Huang, W. Hou, Y. Yang, E.M.V. Hoek, Influence of Zeolite Crystal Size on Zeolite-Polyamide Thin Film Nanocomposite Membranes, Langmuir, 25 (2009) 10139-10145.

Chapter 5

Statement of Authorship

Title of Paper	Hollow Mesoporous Silica Nanoparticles: a Peculiar Structure for Thin Film Nanocomposite Membranes
Publication Status	☐ Published ☐ Accepted for Publication ☑ Submitted for Publication ☐ Unpublished and Unsubmitted w ork w ritten in manuscript style
Publication Details	Masoumeh Zargar, Yusak Hartanto, Bo Jin*, Sheng Dai*, Hollow Mesoporous Silica Nanoparticles: a Peculiar Structure for Thin Film Nanocomposite Membranes, Submitted to ACS Applied Materials and Interfaces.

Principal Author

Name of Principal Author (Candidate)	Masoumeh Zargar		
Contribution to the Paper	Designing and performing the experiments, analysis of the results and writing the manuscript.		
Certification:	This paper reports on original research I conducted during the period of my Higher Degree by Research candidature and is not subject to any obligations or contractual agreements with a third party that would constrain its inclusion in this thesis. I am the primary author of this paper.		
Signature		Date	22/09/2015

Co-Author Contributions

By signing the Statement of Authorship, each author certifies that their stated contribution to the publication is accurate and that permission is granted for the publication to be included in the candidate's thesis.

Name of Co-Author	Yusak Hartanto		
Contribution to the Paper	Assistance in performing the emulsion polymerization and some characterizations.		
Signature		Date	22/09/2015

Name of Co-Author	Bo Jin		
Contribution to the Paper	Supervising the development of the work, assisting in the manuscript review and assessment.		
Signature		Date	22/9/2015

Name of Co-Author	Sheng Dai		
Contribution to the Paper	Supervising the development of the work, assisting in the data interpretation and manuscript review and assessment.		
Signature		Date	22/9/2015

Hollow Mesoporous Silica Nanoparticles: a Peculiar Structure for Thin Film Nanocomposite Membranes

Masoumeh Zargar, Yusak Hartanto, Bo Jin*, Sheng Dai*

School of Chemical Engineering, The University of Adelaide, SA 5005, Australia

*Corresponding authors

Email: bo.jin@adelaide.edu.au; s.dai@adelaide.edu.au

Submitted to ACS Applied Materials & Interfaces (am-2015-094259)

5.1. Abstract

Incorporation of nanomaterials into the thin film composite (TFC) membranes has been introduced as an advantageous approach to enhance the filtration performance of resulting membranes. Herein, novel TFC membranes hybridized with hollow mesoporous silica nanoparticles (HMSN) were fabricated with the aim to enhance their desalination performance. This research focused on understanding the HMSN's functionality to alter the physicochemical properties and permeation behaviours of the hybridized membranes. Spherical HMSN with an average size of ~ 68 nm were fabricated using hydrothermal synthesis in the presence of soft templates. The HMSN were successfully incorporated into the selective polyamide layers of the TFC membranes to produce the thin film nanocomposite (TFN) membranes. The physicochemical properties of the HMSN and resulting TFN membranes were systematically investigated using DLS, TGA, ATR-FTIR, SEM, TEM, nitrogen sorption analyser, tensiometer and XPS analysis. The TFN membranes were more hydrophilic and showed highly improved water flux compared with the membranes without nanoparticle hybridization, while their rejection to NaCl was not significantly changed. The developed TFN membranes also displayed a higher compaction resistance in comparison to the control membranes, suggesting the positive interaction between HMSN and polyamide thin film layers.

Keywords: Thin film nanocomposite membranes; Hollow mesoporous silica; Interfacial polymerization; Water flux; Salt rejection

5.2. Introduction

Nowadays, thin film composite (TFC) membranes are the most commonly used membranes in desalination and water treatment processes. However, there is a strong urge to advance current membranes by improving their performance and physicochemical properties [1-3]. The advancement of nanotechnology has opened new frontiers in the development of high performance TFC membranes. Incorporation of nanoparticles into the TFC membranes, producing a structure known as thin film nanocomposite (TFN) membrane, has been proven to improve membranes' physicochemical properties (hydrophilicity, thermal resistance, mechanical stability, etc.) and permselectivity [4-7]. The most commonly reported nanomaterials in the TFN fabrication include zeolite [5, 8-10], silica [11-15], titania [16-18], silver [19, 20], carbon nanotube (CNT) [6, 21, 22] and graphene oxide [23, 24]. Especially, the introduction of porous nanomaterials into the thin film polyamide (PA) layer of TFC membranes have received considerable attention due to its prospect to enhance the permeability of resulting TFN membranes.

The structure of microporous (e.g. zeolite) and mesoporous (e.g. mesoporous silica) materials contain interconnected pores spanned throughout the whole material providing a high surface area and a large pore volume for water to pass through. Zeolites have excellent molecular sieving properties due to their small pore sizes. However, their irregular cubic structure and oriented pores make their even dispersion and permeation pass control difficult [25]. As of the CNTs, their diameters can be tuned to 1.1- 1.4 nm to ensure the promising increase in water flux without significant salt rejection loss [26]. However, aligning CNTs to achieve the best performance can be a challenge for their industrial application [27]. Mesoporous silica nanoparticles (MSN) are more dispersible than zeolites or carbon nanotubes because of their regular spherical morphology. They have uniform, non-oriented pores, high specific surface areas, and high thermal and mechanical properties together with hydrophilic nature due to the presence of numerous surface hydroxyl groups. Therefore, MSN have been widely used in membrane separation processes such as gas separation [28-30], ultrafiltration [31] and desalination [14, 25]. For instance, Bao et al. fabricated the TFN membranes incorporated with MSN with the mesopore size of 2.47 nm and reported the significant improvement in water permeability without much change of salt rejection [25].

Hollow mesoporous silica nanoparticles (HMSN) have exceptional and flexible porosity, high surface area, low density and high biocompatibility [32, 33]. Therefore, they have attracted considerable attention in various applications such as drug storage and delivery, high-performance catalysis and biomolecule separations [33-35]. Modulation of hollow cavity size and mesoporous shell thickness of this advance structure provides a better control over its surface area to pore volume ratio compared with MSN [33]. Technically, if being applied for water filtration processes, more water molecules can enter the internal cavity of HMSN rather than non-specifically adsorb to the pore walls which makes HMSN superior to the MSN. However, to the best of our knowledge, no study on the incorporation of HMSN into the TFN membranes has been reported. It is expected that the introduction of these nanoparticles can facilitate mass transfer and improve the water permeability of resulting TFN membranes.

Herein, hydrophilic hollow mesoporous silica nanoparticles (HMSN) were designed to fabricate the novel TFN membranes. The HMSN were synthesized using a hydrothermal method in the presence of poly-(tert-butylacrylate) (PtBA) core template and cetyltrimethylammonium bromide (CTAB) structure-directing agent, followed by simultaneous template extraction. The HMSN incorporated TFN membranes were prepared using interfacial polymerization in the presence of HMSN in water phase. From our cross-flow filtration evaluation, the incorporation of HMSN to TFC membranes at the optimum HMSN loading content can significantly improve water flux without obvious alteration of salt rejection. Moreover, the compaction resistance of TFN membranes has been enhanced after HMSN incorporation.

5.3. Experimental

5.3.1. Materials

Polyether sulfone support (PES-MQ-50 kDa) was obtained from Synder filtration (USA). 1, 3-phenylenediamine (MPD, >99 %), 1, 3, 5-benzenetricarbonyl trichloride (TMC, 98 %), n-hexane, tetraethyl orthosilicate (TEOS, >99 %), tert-butyl acrylate (tBA, 98 %), cetyltrimethylammonium bromide (CTAB, >96 %) and ammonium nitrate (NH_4NO_3) were purchased from Sigma-Aldrich. Potassium persulfate (KPS) was supplied from Chem-Supply. Sodium chloride (NaCl) and aqueous ammonia

solution (28 %) were purchased from VWR International. The deionized water used was from a Millipore purification system.

5.3.2. Fabrication of HMSN

Nanoparticles were fabricated by a modified approach as reported by Jiao et al. [33]. First, emulsion polymerization was used to obtain the core templates. 2 g CTAB was mixed with 89 ml of milli-Q water in a 3-neck flask and 2 ml tBA was added to the solution. The mixture was stirred using a mechanical stirrer rotating at 250 rpm under nitrogen protection for 1 h to get rid of dissolved oxygen. The temperature was then raised to 60 °C. 5 ml aqueous KPS solution (0.08 M) was injected into the degassed solution followed by the injection of another 10 ml tBA over a 2 h period using a syringe pump. The reaction was then left to continue for another 3 h at the same temperature and stirring rate. The obtained PtBA emulsion was dialyzed against milli-Q water for 6 days using a dialysis membrane (MWCO 12-14 kDa) with daily change of milli-Q water.

In order to synthesize the HMSN, a volume of purified emulsion containing 120 mg PtBA was added to the mixture of 80 ml milli-Q water and 40 ml absolute ethanol. A homogeneous solution of 0.6 g CTAB in 40 ml milli-Q water was then added to the mixture. After vigorous stirring for 1 h at 40 °C, 1.4 ml aqueous ammonia solution (28 %) and 2.4 ml TEOS were quickly injected to the mixture. The reaction was allowed to continue for 24 h at the same temperature and stirring rate. The obtained nanoparticles were washed several times with water and ethanol to remove unreacted residuals and the purified product was noted as HMSN-b in this study. The HMSN-b were then added to an ammonium nitrate ethanol solution (10 mg/ml) and stirred at 80 ºC under reflux for 1 h to remove the PtBA and CTAB templates. The obtained HMSN were centrifuged at 4000 rpm and washed with ethanol and milli-Q water for three times, and finally redispersed in milli-Q water for further experiments.

5.3.3. Fabrication of TFC and TFN membranes

TFC membranes were fabricated through the interfacial polymerization method on the surface of an ultrafiltration PES support. In detail, PES support was clamped inside a frame equipped with an acrylic plate and a rubber gasket. For PA thin film layer formation on the top of PES support, 2 % (w/v) MPD aqueous solution was

poured to the frame, maintained for 10 min and then drained. A soft rubber roller was used after MPD soaking to remove extra solution. 0.1 % (w/v) TMC hexane solution was then poured into the frame, and allowed to react with the surface adsorbed MPD for 1 min. The excess TMC solution was immediately removed, and the membranes were cured in the oven at 60 °C for 10 min. The resulting TFC membranes were subsequently washed with 22 °C distilled water and stored wet at 5 °C for further characterization and evaluation. The TFC membrane without nanoparticle loading is noted as the control TFC membrane in this study, where the HMSN incorporated TFC membranes are noted as TFN membranes.

The TFN membranes were fabricated according to the above mentioned method except that different concentrations of HMSN (0.01, 0.0325, 0.05 and 0.1 wt %) were dispersed in MPD aqueous solution before interfacial polymerization. TFN membrane incorporated with 0.0325 wt % HMSN is noted as 0.03 wt % in this study. To ensure well dispersion of HMSN, the mixture was sonicated for 1 h in an ultrasonication bath with the temperature controlled at 22 ºC exactly before the interfacial polymerization process.

5.3.4. Characterization of nanoparticles, TFC and TFN membranes

Malvern Zetasizer Nano ZS (Malvern Inst. Ltd., U.K.) was used for obtaining particle size distribution of PtBA and surface charge of HMSN based on the dynamic light scattering (DLS). The samples were prepared by dispersing these nanoparticles in milli-Q water and the measurements were performed at room temperature.

A NICOLET 6700 attenuated total reflectance Fourier transform infrared spectroscopy (ATR-FTIR) equipped with a diamond ATR was used to evaluate the chemical functionalities of various fabricated nanoparticles and membranes.

Thermogravimetric analysis (TGA) was performed using a TGA/DSC 2 STAR System from 30 °C to 800 °C at a heating rate of 10 °C/min under air. An isotherm at 120 °C was set for 1 h during TGA analysis to remove the physically adsorbed water.

The structure of HMSN and the surface and cross-section morphologies of fabricated membranes were characterized using a scanning electron microscope (FEI Quanta 450 FEG Environmental SEM (ESEM)) with a voltage of 10 kV and working distance of 10 mm. The microscope was equipped with an energy-dispersive X-ray

(EDX) detector for elemental analysis. For the cross-section imaging, wet membrane samples were freeze fractured in liquid nitrogen and mounted vertically on the SEM stands. A CRESSINGTON 208 high-resolution sputter coater was used to coat SEM samples with ~ 5 nm layer of platinum before imaging.

Transmission electron microscopy (TEM) images were taken on a FEI Tecnai G2 Spirit Transmission Electron Microscope at an acceleration voltage of 100 kV. HMSN TEM sample was prepared by placing a drop of ethanol dispersed HMSN on a carbon coated copper grid followed by air-drying. The membrane samples for cross-section TEM imaging were prepared by peeling away the polyester backing layer gently to ensure PA and PSF remained together. Small pieces of fabric free membranes were cut and embedded in Epon resin followed by their overnight curing at 50 ºC. Cross sections of 60-70 nm thickness from the cured samples were cut on a Leica EM UC6 Ultramicrotome and mounted on formvar and carbon coated copper grids for imaging.

Nitrogen adsorption/ desorption isotherms were obtained for the HMSN using a TriStar (Micrometrics) analyser at -196 ºC. The dried HMSN were degassed at 120 ºC for at least 12 h prior to the measurement. The Brunauer-Emmett-Teller (BET) surface area and the Barrett-Joyner-Halenda (BJH) pore size distribution were obtained from the adsorption branch of the isotherms.

X-ray photoelectron spectroscopy (XPS) was performed using a Kratos Axis Ultra with a monochromatic aluminium x-ray running at 225 W with a characteristic energy of 1486.6 eV. The area of analysis (Iris aperture) was 0.3 mm x 0.7 mm and the analysis depth was approximately 15 nm from the sample surface with a normal electron take off angle to the sample surface. The spectra were scanned in the range of -10 to 1110 eV with a 160 eV pass energy and 500 meV step. Due to the presence of high surface charges of the samples, charge neutraliser system was used to reduce the surface charge and give high resolution XPS spectra. The obtained survey spectra were interpreted using the CasaXSP software package.

The Attension Theta Optical tensiometer system was used to perform contact angle tests in sessile drop mode at room temperature. The membranes were attached to clean glass slides using double sided tape and a milli-Q water droplet (1 µl) was automatically dispensed on the surface of the membranes. A FireWire camera (55

mm focus length) recorded the droplet surface contact angle equilibrated for 10 s from the time it was dispensed. Curve fitting and data analysis was then performed using the OneAttension software. The reported contact angles were the average of at least 8 different positions on each membrane.

5.3.5. Membrane performance evaluation

A cross-flow filtration unit (CF042, Sterlitech) with an effective membrane surface area of 42 cm^2 was applied to evaluate the performance of fabricated membranes. The membrane coupons were first compacted with distilled water under the pressure of 1.5 MPa to reach an equilibrium flux. The system was then operated with 15 L of 2000 mg/L NaCl solution with the pressure, temperature and concentrate flow rate controlled at 1.5 MPa, 25 ± 0.1 °C and 4 L/min. The concentrate flow was recycled back to the feed tank while the permeate was collected in a container positioned on a digital balance for flux measurement. The permeate weight was reported using a LabX Direct Software (Mettler Toledo) in a continuous mode and the flux (J) was calculated using Equation 1. For salt rejection evaluation, the conductivities of feed water and collected permeate were measured using a conductometer with a probe cell constant of k = 1.0 (AQUA, Cond. / pH, TPS, Australia), and were subsequently converted to the equivalent salt concentrations using a pre-calibration curve. The salt rejections (R %) were obtained by Equation 2.

$$J = \frac{V_P}{\mathrm{A.t}} \quad (1)$$

$$R\ \% = \left(1 - \frac{C_P}{C_F}\right) \times 100 \quad (2)$$

where J is the permeate water flux (LMH), V_P is the permeate volume (L), A is the active membrane surface area (m^2), t is the operation time (h), R is the salt rejection and C_P and C_F are the equivalent NaCl concentrations in collected permeate and feed water, respectively.

5.4. Results and Discussion

5.4.1. Synthesis and characterization of HMSN

Fig 5-1 shows the schematic illustration of HMSN fabrication procedure. At first, PtBA core template was synthesized using emulsion polymerization. The CTAB encapsulated silica shell was then formed around the successfully fabricated PtBA

core following a hydrothermal sol-gel synthesis. Finally, the obtained HMSN-b were refluxed in an ethanol solution of ammonium nitrate (10 mg/ml) which can simultaneously extract CTAB and PtBA templates through ion exchange and dissolution leaving behind HMSN.

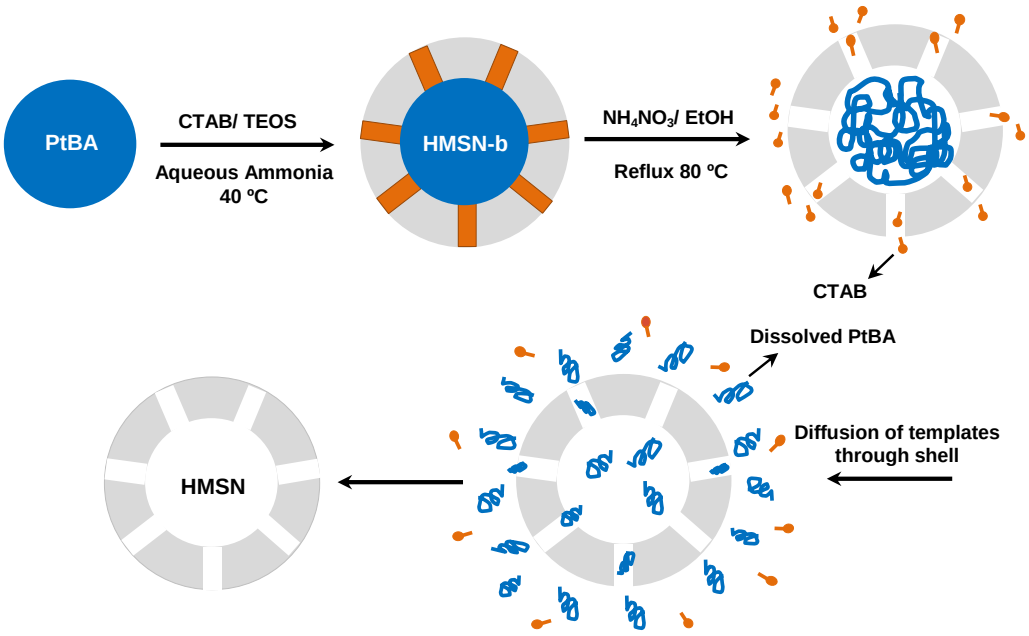

Figure 5-1 The schematic illustration of the HMSN fabrication strategy. The CTAB and PtBA templates can be removed simultaneously through ion exchange and dissolution.

Fig 5S-1 (Supporting Information) shows DLS measurement results for the fabricated PtBA templates. The PtBA templates have an average hydrodynamic diameter of 34.8±3.6 with a relatively low polydispersity index (PDI) of 0.08, which indicates the uniformity of latex nanospheres.

FTIR and TGA were performed to examine the successful template encapsulation, HMSN-b extraction and HMSN formation. Fig 5-2A represents the FTIR spectra for the CTAB and PtBA templates, HMSN-b, and HMSN. The IR characteristic peaks of CTAB appeared at 2918 cm^{-1} (asymmetric -C-H), 2848 cm^{-1} (symmetric -C-H) and ~ 1470 cm^{-1} (bending vibrations of -C-H) [36, 37]. For PtBA, the main characteristic peaks emerged at ~ 2916 cm^{-1} (asymmetric -C-H), 2850 cm^{-1} (symmetric -C-H), 1481 cm^{-1} (bending vibrations of -C-H), 1365 cm^{-1} (tert-butyl-C-H) and 1392 cm^{-1} (tert-butyl -C-C). The other peaks of the PtBA appeared at 1722 cm^{-1} and 1142 cm^{-1} which correspond to the vibration of its -C=O and -C-O groups [33, 38]. FTIR spectrum of HMSN-b show strong peaks at ~ 800, 955 and 1050 cm^{-1}, corresponding to the

vibrations of Si-O-Si symmetric bond, Si-OH stretching bond and Si-O-Si asymmetric bond. All characteristic peaks of C-H, C-O and C=O, originated from CTAB and PtBA templates, are also observed in the FTIR spectrum of HMSN-b. After template extraction, the FTIR spectrum of HMSN displays the main silica peaks and all other peaks associated with CTAB and PtBA are disappeared. FTIR confirms the successful synthesis of HMSN-b and removal of templates from the fabricated nanoparticles to form hollow mesoporous structured HMSN.

TGA analysis was performed to estimate the weight percentage of the templates to the final HMSN. The TGA temperature was raised to 120 ºC and kept at this temperature for 1 h to remove the physically adsorbed water and then slowly increased to 800 ºC. TGA thermograms in Fig 5-2B show the normalized weight loss over temperature for CTAB, PtBA, HMSN-b and HMSN. The TGA of CTAB shows a sharp decomposition stage with the onset decomposition temperature of 237.3 ºC. 97.4 % of CTAB is decomposed between 202 and 340 ºC which is due to the Hoffman degradation and its successive carbon chain fragmentation or decomposition [39, 40]. CTAB is finally fully decomposed at ~ 573 ºC. For PtBA, two decomposition stages with the onset decomposition temperatures of 241.9 ºC and 486.9 ºC are observed. The first sharp decomposition stage contributes to 79.2 % residual weight loss and is happened between 200 ºC and 340 ºC. That includes the thermolysis of the PtBA ester and the organic components removal by oxidation [41]. The remaining of PtBA slowly decomposes after that with the final decomposition temperature of ~ 573 ºC.

For the HMSN-b, the residual weight is sharply decreased between ~ 170 ºC to ~ 570 ºC with an onset decomposition temperature of 202.8 ºC. The weight is then slightly decreases up to 800 ºC. The total residual weight loss of HMSN-b is ~ 46.1 % which is attributed to the CTAB and PtBA template extraction in addition to the dihydroxylation of HMSN-b's Si-OH groups [38]. However, the HMSN showed only 11.4 % weight loss over the temperature range of ~ 170-800 ºC which is attributed to the Si-OH groups' dihydroxylation. Comparing the TGA thermograms of HMSN-b and HMSN, it can be concluded that ~ 35 % of the HMSN-b weight is from CTAB and PtBA templates which fully decompose in the studied temperature

range. TGA results again confirm the successful removal of templates from the HMSN-b.

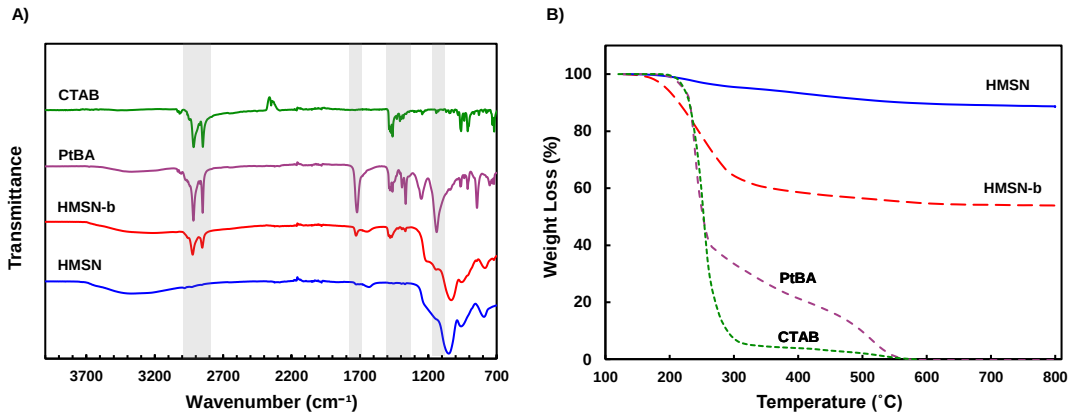

Figure 5-2 A) FTIR spectra for the CTAB and PtAB templates, HMSN-b and HMSN B) TGA thermograms for CTAB and PtBA templates, HMSN-b and HMSN.

Fig 5-3 shows SEM and TEM images of the fabricated HMSN. From the SEM images, the HMSN particles are spherical and well-dispersed in water. TEM images confirm the hollow core structure of the HMSN with the average particle size of ~ 68 nm and the average core size and shell thicknesses of ~ 25 nm and ~ 21.5 nm.

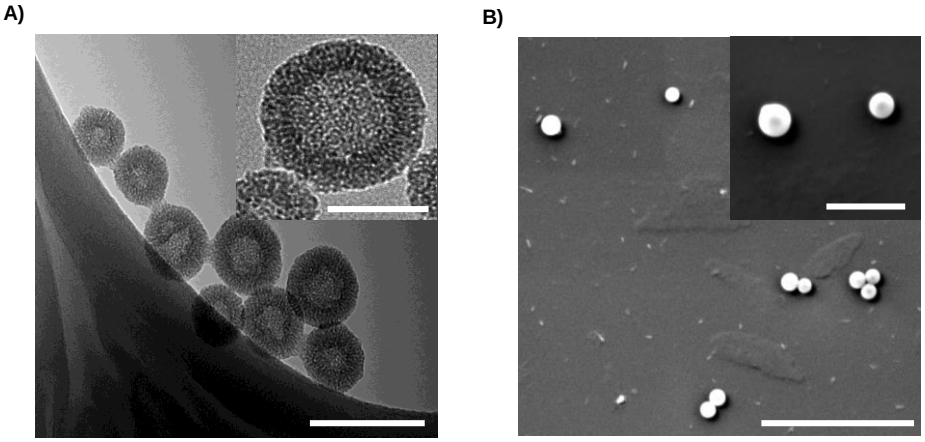

Figure 5-3 High and low magnification A) TEM and B) SEM images of the HMSN. The hollow mesoporous structure of HMSN can be clearly seen from the high resolution TEM image.Scale bars for the TEM images are 100 nm and 50 nm (inset) and for the SEM images are 1 µm and 200 nm (inset).

The mesopores on the shell are also evident from the obtained high resolution TEM image. The average core size of HMSN achieved using TEM was smaller than the average hydrodynamic diameter of the fabricated PtBA obtained through DLS measurement. That is due to the hydration layer formed on the PtBA nanospheres in

their aqueous DLS sample while the size given by TEM is the size of samples in their dried state.

The nitrogen sorption results in Fig 5-4 show a type IV isotherm with a type H4 hysteresis loop, which is typical for hollow structures with mesoporous walls [42-45]. The capillary condensation step, appearing in the relative pressure interval P/P_0 = 0.2–0.4, indicates the presence of uniform mesopores. The H4 loop with parallel and almost horizontal adsorption and desorption branches in a wide range of P/P_0 represents hollow cores with mesoporous walls. Physisorption results again confirm the successful synthesis of HMSN. The pore size distribution calculated using the BJH method, embedded in Fig 5-4, shows that HMSN possess mesopores with an average size of 2.1 nm. In addition, they have relatively high specific surface area and total pore volume of 910.8 m^2/g and 0.75 cm^3/g.

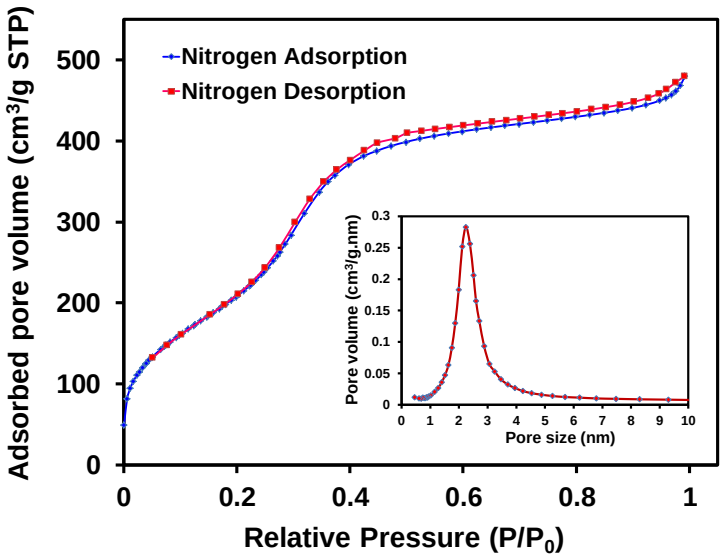

Figure 5-4 Nitrogen adsorption/ desorption isotherms for the fabricated HMSN; the inset is the pore size distribution obtained from the BJH method.

Fig 5S-2 (Supporting Information) represents the zeta potential of HMSN in milli-Q water at room temperature. The negative zeta potential of -26.5±5.2 mV indicates the well dispersion of HMSN in aqueous system which facilitates the random distribution of nanoparticles in the TFN membranes. The negative charge of HMSN is due to the hydrolysis of their surface hydroxyl groups which render the nanoparticles to be highly hydrophilic.

XPS results for the fabricated HMSN show the typical spectrum for silica [46]. As seen in Fig 5S-3 (Supporting Information), O 1s peak is at 529.5 eV, C 1s peak is at 281.5 eV, Si 2p peak is at 100 eV and Si 2s peak is at 154.3 eV. The key elemental compositions are summarized in Table 5-1.

Tab 5-1 XPS results for HMSN, TFC and 0.05 wt % HMSN incorporated TFN membrane.

Sample name	Atomic percentage of elements			
	N (%)	O (%)	C (%)	Si (%)
HMSN	-	67.09	11.3	21.61
TFC	9.76	16.54	73.71	-
TFN	10.41	15.12	73.73	0.74

5.4.2. Characterization of TFN membranes

Fig 5-5 shows the high and low magnification surface and cross-section SEM images of the fabricated membranes with different concentrations of HMSN.

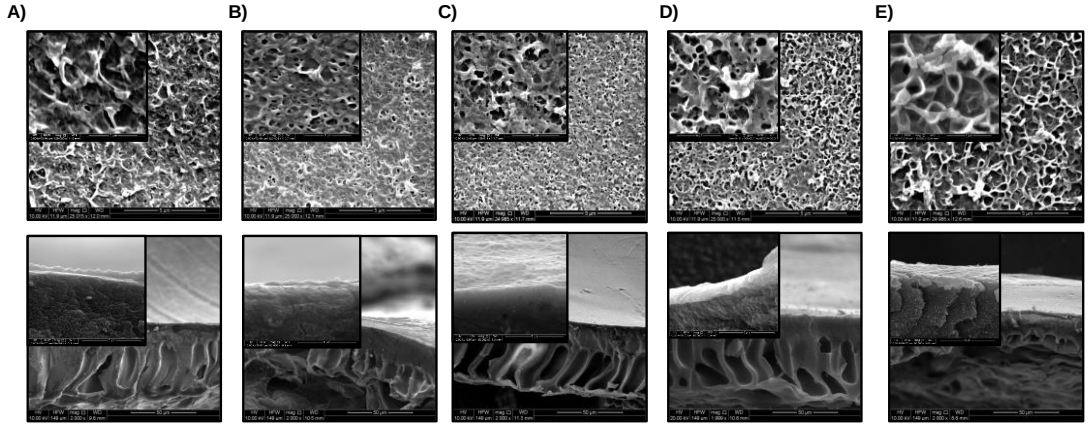

Figure 5-5 Low and high magnification SEM surface (top) and cross-section (bottom) images of the synthesized TFC membrane and TFN membranes incorporated with different concentrations of HMSN: A) TFC, B) TFN, 0.01 wt %, C) TFN, 0.03 wt %, D) TFN, 0.05 wt % and E) TFN, 0.1 wt %. For the surface images, the magnifications are 25000x and 120000x, and for the cross-section images, the magnifications are 2000x and 50000x.

The ridge and valley structure, which is expected from PA membranes fabricated from MPD and TMC monomers, is observed for all membranes. Increasing the concentration of HMSN in the TFN membranes affects the surface morphology through enlarging the PA leaves as shown in high magnification surface SEM images. That can increase the surface areas of the TFN membranes, and therefore,

enhance permeability. Cross-section SEM images indicate the presence of a thin PA layer with the thickness of ~ 50-450 nm on the surface of PES support for all samples.

Fig 5-6 A shows surface SEM images obtained from tilting a typical cross-section SEM sample (TFN incorporated with 0.05 wt % HMSN). The cross-section TEM image of the same sample is shown in Fig 5-6 B. The presence of HMSN attached to the surface or embedded under the PA surface leaves is evident from the high magnification cross section images which confirm the successful incorporation of HMSN into the PA layer.

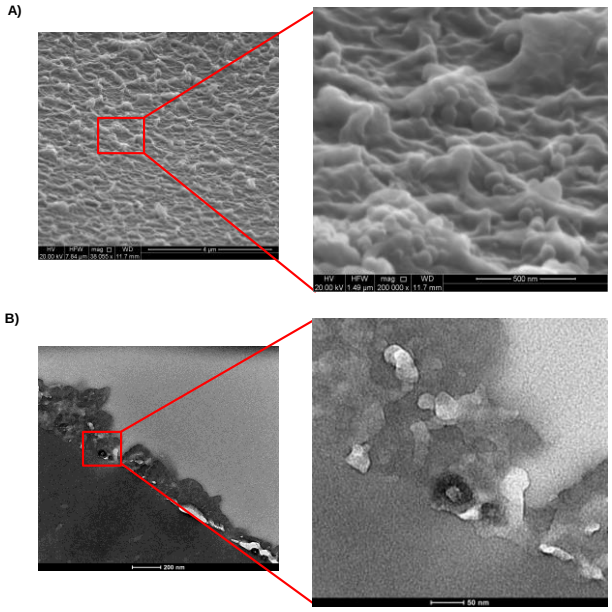

Figure 5-6 Images taken from a typical TFN membrane incorporated with 0.05 wt % HMSN A) tilted surface images from cross-section SEM sample, and B) cross-section TEM images. For the SEM images, the scale bars are 4 µm and 500 nm, and for the TEM images the scale bars are 200 nm and 50 nm.

Fig 5-7 shows the contact angles for the fabricated TFN membranes as a function of HMSN incorporation concentration. The contact angle of membranes decreases from 74.4º to 53.8º by increasing HMSN loading from 0 to 0.1 wt % in the PA layer. That is due to the presence of abundant surface hydroxyl groups of HMSN. This observation agrees with those being reported in literature for TFN membranes incorporated with hydrophilic nanoparticles [15, 18, 25, 46]. For instance, Niksefat et al. found that the contact angle of their TFC membranes decreased from 82º to 44º through introduction of 0.1 (w/v) % solid silica nanoparticles in TFC membranes

[15]. Rajaeian et al. also reported a drop of contact angle from 87.3º to 59º by increasing the concentration of hydrophilic titania in their TFN membranes [18]. Lower contact angles indicate the higher hydrophilicity of membrane surfaces and can be beneficial for their permeability enhancement.

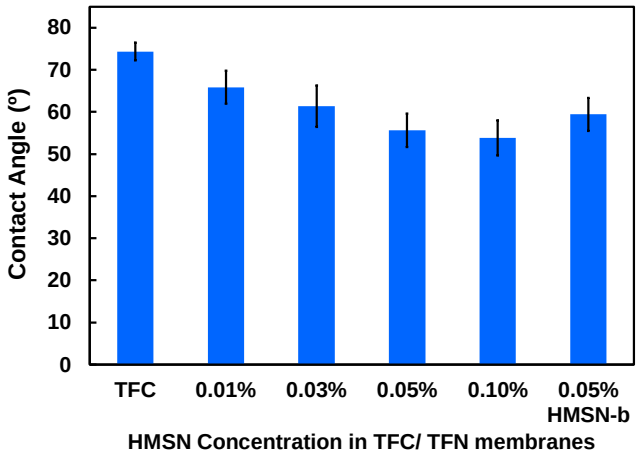

Figure 5-7 Comparison on the contact angles of various fabricated TFC/TFN membranes as a function of HMSN loading. Contact angle of the TFN membrane incorporated with 0.05 % HMSN-b is also included for comparision. The reported contact angles are the average of at least 8 different positions on each membrane.

XPS is an analysis technique that uses the photoelectric effect to identify and quantify elements on the surface of materials. The survey XPS spectra of HMSN, TFC and a typical TFN membrane containing 0.05 wt % HMSN are shown in Supporting Information, Fig 5S-3 and Table 5-1 lists the constituents' elements and their atomic percentages of the samples. For TFC membrane, the core electron binding energies present at 284.5 eV for C 1s, 400.0 for N 1s and 531.5 eV for O 1s [47]. In the case of TFN membrane, in addition to the C, N and O peaks at similar positions to that of TFC membrane, two new small peaks at 102.1 eV and 154.3 eV, which are attributed to Si 2p and Si 2s [48], are also emerged. That again justifies the successful incorporation of HMSN to the TFN membrane. Moreover, the EDX spectra presented in Fig 5S-5 (Supporting Information) indicate the successful incorporation of HMSN to the typical TFN membrane.

5.4.3. Desalination performance of TFN membranes

The membrane performance evaluation in terms of water flux and salt rejection was performed on the synthesized membranes using a cross-flow filtration unit. Fig 5-8

presents the performance results of various TFN membranes as a function of HMSN loading.

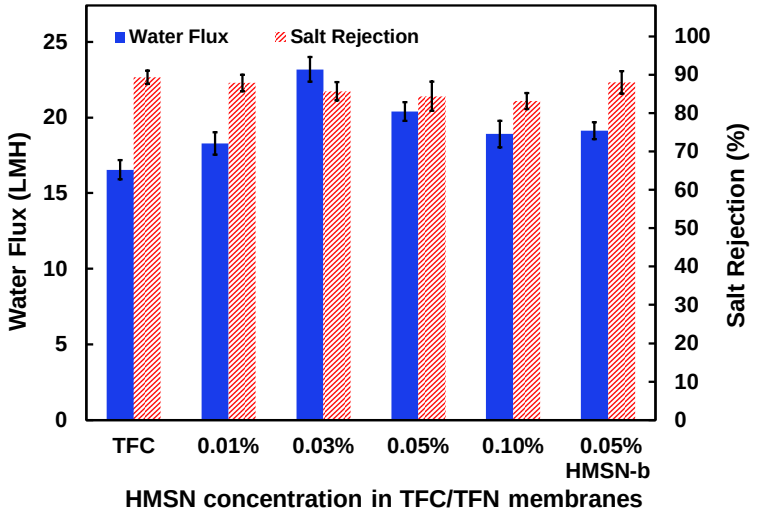

Figure 5-8 The performance evaluations of the fabricated TFC/TFN membranes in terms of water flux and salt rejection as a function of HMSN loading. The performance of the TFN membrane with 0.05 wt % HMSN-b is also shown for comparison.

Water flux increases up to ~ 40 % with increasing HMSN loading of 0.03 wt % and then decreases as more nanoparticles are added. The incorporation of nanomaterials into the membranes at a concentration higher than a threshold value can block water permeation path and enhance mass transfer resistance. The lower water flux for the concentrations higher than 0.03 wt % HMSN might be due to that fact. However, although for the highest HMSN loading (0.1 wt %), the water flux is ~ 18 % lower than the optimum concentration of HMSN, it is still ~ 15 % higher than the water flux of the control TFC membrane. The results indicate that the incorporation of HMSN, in the whole HMSN concentration range, has improved the water flux of resulting TFN membranes.

For salt rejection, a slight decrease is observed with HMSN percentage (~ 6 % decrease at 0.1 wt % HMSN). Loading more nanoparticles to the PA layer might increase the formation of defects in the PA structure which results in the salt rejection drop. Lind et al. performed a pioneer study on the performance of TFN membranes incorporated with zeolite nanoparticles at different sizes and with different chemistries for PA layer. They stated that the incorporation of zeolite

nanoparticles could change the bulk PA structure and generate some defects [9]. Similarly, the incorporation of other nanomaterials can influence the porosity of PA layer and change its performance properties. In addition to the structural change of the PA layer, the mesopores on the HMSN wall might also contribute to the salt permeability across the membrane. However, considering previous studies on the MSN incorporation and the small mesopore size of the fabricated HMSN in this study (2.1 nm), this contribution may not be too significant. Wu et al. studied the performance of TFN membranes containing MSN with different pore sizes, and reported around 5 % loss of salt rejection for their TFN membranes containing MSN with 2.2 nm pores. However, with further increase of the pore diameters to 2.9 or 3.2 nm in their study, 41 % and 47 % rejection loss were observed [14]. Bao et al. fabricated TFN membranes containing MSN with 2.47 nm pore diameter, and reported negligible salt rejection change for their TFN membranes. They correlated their small salt rejection alteration to the attachment of counterions to the MSN mesopore walls and the overlap of electrical double layers [25]. For the HMSN incorporated TFN membranes in this study, the alteration rate of the salt rejections agrees with those reported by Bao et al. and Wu et al. Depending on the pore structure and its wall's surface potential, the accumulation of counterions on the pore walls can be at such high densities that the ions' size effectively repel more ions [49].

To further investigate the influence of HMSN pores on the desalination performance, 0.05 wt % HMSN-b was incorporated to the PA layer through the same procedure. Based on the TGA results, ~ 35 % of the HMSN weight is related to CTAB and PtBA templates. From that, the content of 0.05 wt % HMSN-b nanoparticles is equivalent to that of the 0.03 wt % HMSN. The comparison of the performance results show that for the 0.05 wt % HMSN-b, the water flux is ~ 21 % lower than that of the TFN membrane incorporated with 0.03 wt % HMSN while their salt rejection difference is negligible (~ 2.5 %). It suggests that the peculiar porous structure of HMSN can effectively facilitate the water permeability of resulting TFN membranes.

Compaction resistance is an important parameter for the TFC membranes. Both ultrafiltration support and PA layer of TFC membranes experience irreversible compaction under high pressure loading which results in the permanent decrease of

water flux [50-52]. Fig 5-9 shows the compaction rates for the fabricated membranes obtained through measuring the water flux as a function of time during the membrane compaction stage.

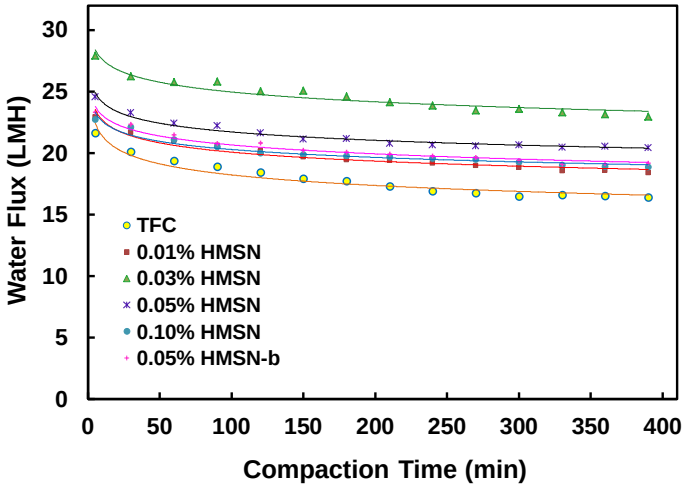

Figure 5-9 The water flux of the fabricated TFC and TFN membranes versus compaction time against DI water at 1.5 MPa and 25 ± 0.1 ºC.

The results show that the compaction resistance of the TFN membranes have slightly increased by increasing HMSN loading in the PA layer. The compaction rates are 19.00 %, 17.02 %, 16.34 % and 15.88 % for 0.01 %, 0.03 %, 0.05 % and 0.1% HMSN and 17.40% for 0.05 % HMSN-b whilst it is 21.59 % for the control TFC membrane. Prendergast et al. also observed improved compaction resistance for their TFN membrane, incorporated with zeolite in the thin PA layer; and reported the importance of enhancing the mechanical properties of thin PA layer for improving the overall TFC membrane performance [52]. Compaction results suggest that HMSN incorporation can be beneficial for strengthening the resulting membranes.

5.5. Conclusions

The HMSN with an average particle size of ~ 68 nm were synthesized and successfully incorporated into the PA thin film layer of the TFC membranes. Various analytical techniques have been applied to investigate the physicochemical properties of fabricated HMSN and resulting TFN membranes. The HMSN have an average core size and shell thicknesses of ~ 25 nm and 21.5 nm together with a zeta potential of -26.5±5.2 mV. The surface morphologies of the fabricated TFN membranes are changed after incorporating HMSN, and larger leaves on the PA layer contribute to

the enhanced hydrophilicity of the resulting TFN membranes. Desalination performance in terms of water flux and salt rejection has been evaluated using a cross-flow filtration unit. The permeability of membranes increases after introducing HMSN with an optimum HMSN concentration of 0.03 wt %, where the water flux moves up to 40 % compared with the control TFC membrane while a negligible salt rejection compensation is observed. Moreover, TFN membranes show an improved compaction resistance in comparison to the control TFC membranes, which serves another advantage for the application of the HMSN incorporated TFN membranes.

References

[1] M. Elimelech, W.A. Phillip, The Future of Seawater Desalination: Energy, Technology, and the Environment, Science, 333 (2011) 712-717.

[2] S.S. Shenvi, A.M. Isloor, A.F. Ismail, A review on RO membrane technology: Developments and challenges, Desalination, 368 (2015) 10-26.

[3] H.M. Hegab, A. ElMekawy, T.G. Barclay, A. Michelmore, L. Zou, C.P. Saint, M. Ginic-Markovic, Fine-Tuning the Surface of Forward Osmosis Membranes via Grafting Graphene Oxide: Performance Patterns and Biofouling Propensity, ACS Applied Materials & Interfaces, 7 (2015) 18004-18016.

[4] G.D. Kang, Y.M. Cao, Development of antifouling reverse osmosis membranes for water treatment: A review, Water Research, 46 (2012) 584-600.

[5] S.G. Kim, D.H. Hyeon, J.H. Chun, B.H. Chun, S.H. Kim, Nanocomposite poly(arylene ether sulfone) reverse osmosis membrane containing functional zeolite nanoparticles for seawater desalination, Journal of Membrane Science, 443 (2013) 10-18.

[6] H. Zhao, S. Qiu, L. Wu, L. Zhang, H. Chen, C. Gao, Improving the performance of polyamide reverse osmosis membrane by incorporation of modified multi-walled carbon nanotubes, Journal of Membrane Science, 450 (2014) 249-256.

[7] A.W. Mohammad, Y.H. Teow, W.L. Ang, Y.T. Chung, D.L. Oatley-Radcliffe, N. Hilal, Nanofiltration membranes review: Recent advances and future prospects, Desalination, 356 (2015) 226-254.

[8] B.H. Jeong, E.M.V. Hoek, Y. Yan, A. Subramani, X. Huang, G. Hurwitz, A.K. Ghosh, A. Jawor, Interfacial polymerization of thin film nanocomposites: A new concept for reverse osmosis membranes, Journal of Membrane Science, 294 (2007) 1-7.

[9] M.L. Lind, A.K. Ghosh, A. Jawor, X. Huang, W. Hou, Y. Yang, E.M.V. Hoek, Influence of Zeolite Crystal Size on Zeolite-Polyamide Thin Film Nanocomposite Membranes, Langmuir, 25 (2009) 10139-10145.

[10] J. Duan, Y. Pan, F. Pacheco, E. Litwiller, Z. Lai, I. Pinnau, High-performance polyamide thin-film-nanocomposite reverse osmosis membranes containing hydrophobic zeolitic imidazolate framework-8, Journal of Membrane Science, 476 (2015) 303-310.

[11] G.L. Jadav, P.S. Singh, Synthesis of novel silica-polyamide nanocomposite membrane with enhanced properties, Journal of Membrane Science, 328 (2009) 257-267.

[12] L. Jin, W. Shi, S. Yu, X. Yi, N. Sun, C. Ma, Y. Liu, Preparation and characterization of a novel PA-SiO_2 nanofiltration membrane for raw water treatment, Desalination, 298 (2012) 34-41.

[13] A. Tiraferri, Y. Kang, E.P. Giannelis, M. Elimelech, Highly hydrophilic thin-film composite forward osmosis membranes functionalized with surface-tailored nanoparticles, ACS Applied Materials & Interfaces, 4 (2012) 5044-5053.

[14] H. Wu, B. Tang, P. Wu, Optimizing polyamide thin film composite membrane covalently bonded with modified mesoporous silica nanoparticles, Journal of Membrane Science, 428 (2013) 341-348.

[15] N. Niksefat, M. Jahanshahi, A. Rahimpour, The effect of SiO_2 nanoparticles on morphology and performance of thin film composite membranes for forward osmosis application, Desalination, 343 (2014) 140-146.

[16] R.X. Zhang, L. Braeken, P. Luis, X.L. Wang, B. Van der Bruggen, Novel binding procedure of TiO_2 nanoparticles to thin film composite membranes via self-polymerized polydopamine, Journal of Membrane Science, 437 (2013) 179-188.

[17] D. Emadzadeh, W.J. Lau, T. Matsuura, A.F. Ismail, M. Rahbari-Sisakht, Synthesis and characterization of thin film nanocomposite forward osmosis membrane with hydrophilic nanocomposite support to reduce internal concentration polarization, Journal of Membrane Science, 449 (2014) 74-85.

[18] B. Rajaeian, A. Rahimpour, M.O. Tade, S. Liu, Fabrication and characterization of polyamide thin film nanocomposite (TFN) nanofiltration membrane impregnated with TiO_2 nanoparticles, Desalination, 313 (2013) 176-188.

[19] J. Yin, Y. Yang, Z. Hu, B. Deng, Attachment of silver nanoparticles (AgNPs) onto thin-film composite (TFC) membranes through covalent bonding to reduce membrane biofouling, Journal of Membrane Science, 441 (2013) 73-82.

[20] Y. Liu, E. Rosenfield, M. Hu, B. Mi, Direct observation of bacterial deposition on and detachment from nanocomposite membranes embedded with silver nanoparticles, Water Research, 47 (2013) 2949-2958.

[21] C.F. de Lannoy, E. Soyer, M.R. Wiesner, Optimizing carbon nanotube-reinforced polysulfone ultrafiltration membranes through carboxylic acid functionalization, Journal of Membrane Science, 447 (2013) 395-402.

[22] L. Dumée, J. Lee, K. Sears, B. Tardy, M. Duke, S. Gray, Fabrication of thin film composite poly(amide)-carbon-nanotube supported membranes for enhanced performance in osmotically driven desalination systems, Journal of Membrane Science, 427 (2013) 422-430.

[23] F. Perreault, M.E. Tousley, M. Elimelech, Thin-film composite polyamide membranes functionalized with biocidal graphene oxide nanosheets, Environmental Science & Technology Letters, 1 (2014) 71-76.

[24] L. He, L.F. Dumée, C. Feng, L. Velleman, R. Reis, F. She, W. Gao, L. Kong, Promoted water transport across graphene oxide–poly(amide) thin film composite membranes and their antibacterial activity, Desalination, 365 (2015) 126-135.

[25] M. Bao, G. Zhu, L. Wang, M. Wang, C. Gao, Preparation of monodispersed spherical mesoporous nanosilica–polyamide thin film composite reverse osmosis membranes via interfacial polymerization, Desalination, 309 (2013) 261-266.

[26] T.V. Ratto, J.K. Holt, A.W. Szmodis, Membranes with embedded nanotubes for selective permeability, Google Patents, (2010) US 7993524 B2.

[27] X. Qu, J. Brame, Q. Li, P.J.J. Alvarez, Nanotechnology for a safe and sustainable water supply: enabling integrated water treatment and reuse, Accounts of Chemical Research, 46 (2013) 834-843.

[28] B. Zornoza, S. Irusta, C. Téllez, J. Coronas, Mesoporous silica sphere−polysulfone mixed matrix membranes for gas separation, Langmuir, 25 (2009) 5903-5909.

[29] K.S. Jang, H.J. Kim, J.R. Johnson, W.G. Kim, W.J. Koros, C.W. Jones, S. Nair, Modified mesoporous silica gas separation membranes on polymeric hollow fibers, Chemistry of Materials, 23 (2011) 3025-3028.

[30] R. Kishor, A.K. Ghoshal, APTES grafted ordered mesoporous silica KIT-6 for CO2 adsorption, Chemical Engineering Journal, 262 (2015) 882-890.

[31] J. Huang, K. Zhang, K. Wang, Z. Xie, B. Ladewig, H. Wang, Fabrication of polyethersulfone-mesoporous silica nanocomposite ultrafiltration membranes with antifouling properties, Journal of Membrane Science, 423–424 (2012) 362-370.

[32] N. Kato, T. Ishii, S. Koumoto, Synthesis of monodisperse mesoporous silica hollow microcapsules and their release of loaded materials, Langmuir, 26 (2010) 14334-14344.

[33] Y. Jiao, J. Guo, S. Shen, B. Chang, Y. Zhang, X. Jiang, W. Yang, Synthesis of discrete and dispersible hollow mesoporous silica nanoparticles with tailored shell thickness for controlled drug release, Journal of Materials Chemistry, 22 (2012) 17636-17643.

[34] Z. Feng, Y. Li, D. Niu, L. Li, W. Zhao, H. Chen, L. Li, J. Gao, M. Ruan, J. Shi, A facile route to hollow nanospheres of mesoporous silica with tunable size, Chemical Communications, (2008) 2629-2631.

[35] Y. Yin, W. Deng, H. Wang, A. Li, C. Wang, Z. Jiang, H. Wu, Fabrication of hybrid membranes by incorporating acid-base pair functionalized hollow mesoporous silica for enhanced proton conductivity, Journal of Materials Chemistry A, 3 (2015) 16079-16088.

[36] L. Pan, Q. He, J. Liu, Y. Chen, M. Ma, L. Zhang, J. Shi, Nuclear-targeted drug delivery of TAT peptide-conjugated monodisperse mesoporous silica nanoparticles, Journal of the American Chemical Society, 134 (2012) 5722-5725.

[37] P. Zhang, P.Y. Zheng, F.Y. Zhao, Q.F. An, C.J. Gao, Preparation and pervaporation characteristics of novel ethanol permselective polyelectrolyte-surfactant complex membranes, RSC Advances, 5 (2015) 63545-63552.

[38] K. Möller, J. Kobler, T. Bein, Colloidal suspensions of nanometer-sized mesoporous silica, Advanced Functional Materials, 17 (2007) 605-612.

[39] J. Goworek, A. Kierys, W. Gac, A. Borówka, R. Kusak, Thermal degradation of CTAB in as-synthesized MCM-41, J Therm Anal Calorim, 96 (2009) 375-382.

[40] F. Kleitz, W. Schmidt, F. Schüth, Calcination behavior of different surfactant-templated mesostructured silica materials, Microporous and Mesoporous Materials, 65 (2003) 1-29.

[41] J. Duvigneau, H. Schönherr, G.J. Vancso, Atomic force microscopy based thermal lithography of poly(tert-butyl acrylate) block copolymer films for bioconjugation, Langmuir, 24 (2008) 10825-10832.

[42] A.H. Lu, Zhao, Dongyuan, Wan, Ying, Nanocasting : a versatile strategy for creating nanostructured porous materials, Royal Society of Chemistry, Cambridge, 2010.

[43] W. Hao, Y. Xi, J. Hu, T. Wang, Y. Du, X.L. Wang, Magnetic properties and microstructures of iron oxide@mesoporous silica core-shell composite for applications in magnetic dye separation, Journal of Applied Physics, 111 (2012) 07B301.

[44] X. Zhou, X. Cheng, W. Feng, K. Qiu, L. Chen, W. Nie, Z. Yin, X. Mo, H. Wang, C. He, Synthesis of hollow mesoporous silica nanoparticles with tunable shell thickness and pore size using amphiphilic block copolymers as core templates, Dalton Transactions, 43 (2014) 11834-11842.

[45] J. Liu, H.Q. Yang, F. Kleitz, Z.G. Chen, T. Yang, E. Strounina, G.Q. Lu, S.Z. Qiao, Nanoreactors: yolk–shell hybrid materials with a periodic mesoporous organosilica shell:

Ideal nanoreactors for selective alcohol oxidation, Advanced Functional Materials, 22 (2012) 661-661.

[46] B. Deng, J. Yin, Thin-film nano-composite membrane with mesoporous silica nanoparticles, in, Google Patents, 2014.

[47] S.Y. Kwak, S.H. Kim, S.S. Kim, Hybrid organic/inorganic reverse osmosis (RO) membrane for bactericidal anti-fouling. 1. Preparation and characterization of TiO_2 nanoparticle self-assembled aromatic polyamide thin-film-composite (TFC) membrane, environmental science & technology, 35 (2001) 2388-2394.

[48] W. Li, S. Wang, S. He, J. Wang, Y. Guo, Y. Guo, Enhanced photoluminescence from CdS with SiO_2 nanopillar arrays, Scientific Reports, 5 (2015) 11375.

[49] D. Gillespie, High Energy Conversion Efficiency in Nanofluidic Channels, Nano Letters, 12 (2012) 1410-1416.

[50] E.M.V. Hoek, A.K. Ghosh, X. Huang, M. Liong, J.I. Zink, Physical–chemical properties, separation performance, and fouling resistance of mixed-matrix ultrafiltration membranes, Desalination, 283 (2011) 89-99.

[51] M.T.M. Pendergast, J.M. Nygaard, A.K. Ghosh, E.M.V. Hoek, Using nanocomposite materials technology to understand and control reverse osmosis membrane compaction, Desalination, 261 (2010) 255-263.

[52] M.M. Pendergast, A.K. Ghosh, E.M.V. Hoek, Separation performance and interfacial properties of nanocomposite reverse osmosis membranes, Desalination, 308 (2013) 180-185.

TOC:

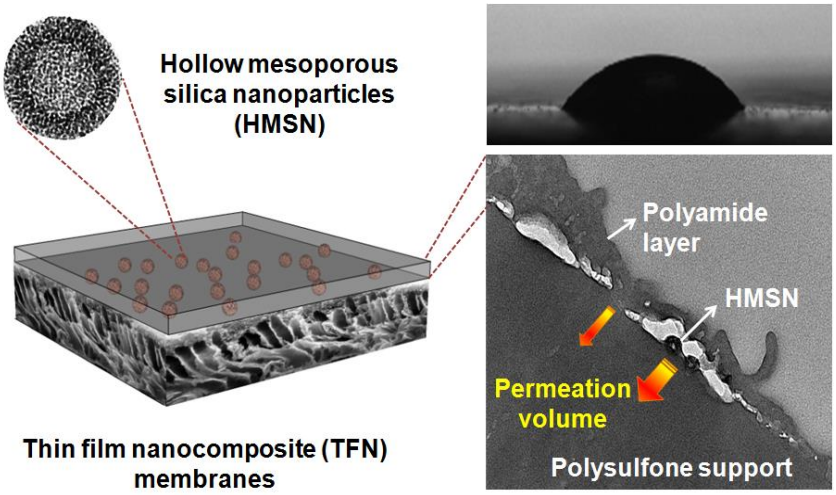
Hollow mesoporous
silica nanoparticles
(HMSN)
Thin film nanocomposite (TFN)
membranes
Polyamide
layer
HMSN
Permeation
volume
Polysulfone support

5.6. Supporting Information

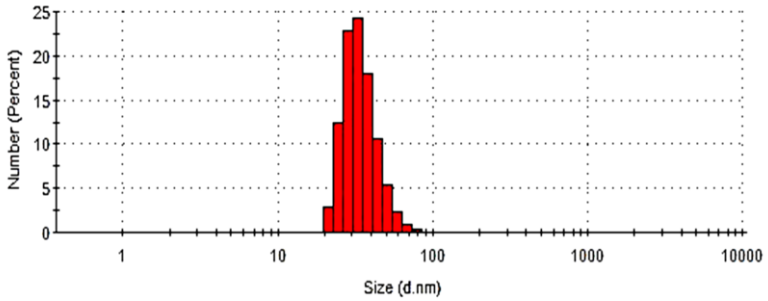

Fig 5S-1 Hydrodynamic size distribution of PtBA nanospheres used as the core template in HMSN synthesis. The PtBA nanospheres have an average hydrodynamic diameter of 34.8±3.6 nm.

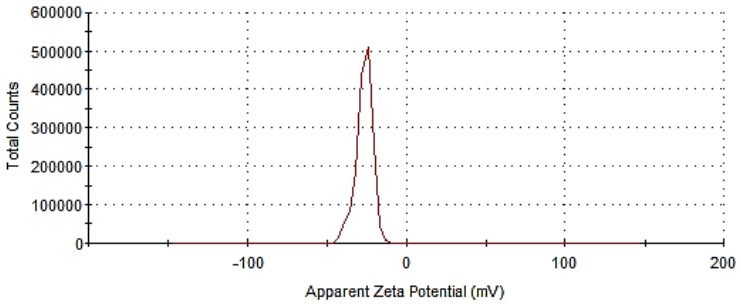

Fig 5S-2 Zeta potential for the fabricated HMSN; the particles have a narrow charge distribution with an average surface zeta potential of -26.5±5.2 mV.

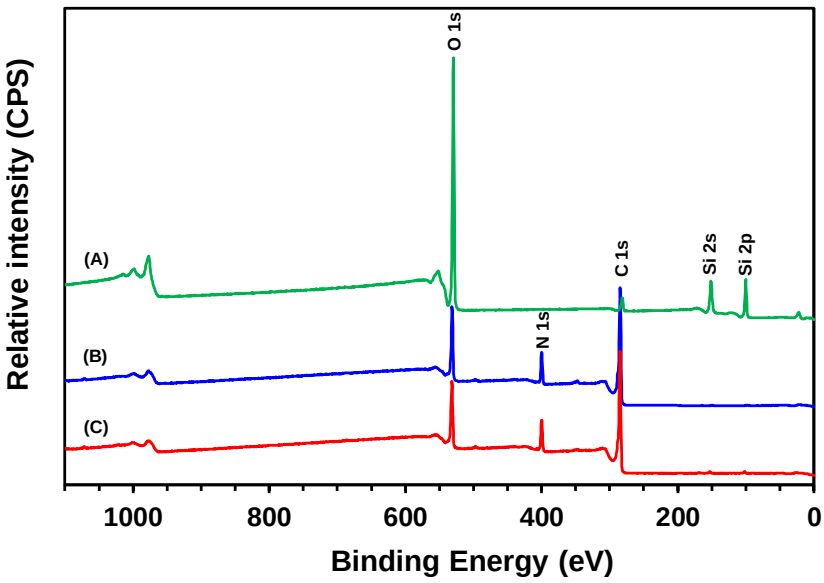

Fig 5S-3 XPS spectra for (a) HMSN, (b) TFC membrane and (c) a typical TFN membrane containing 0.05% HMSN.

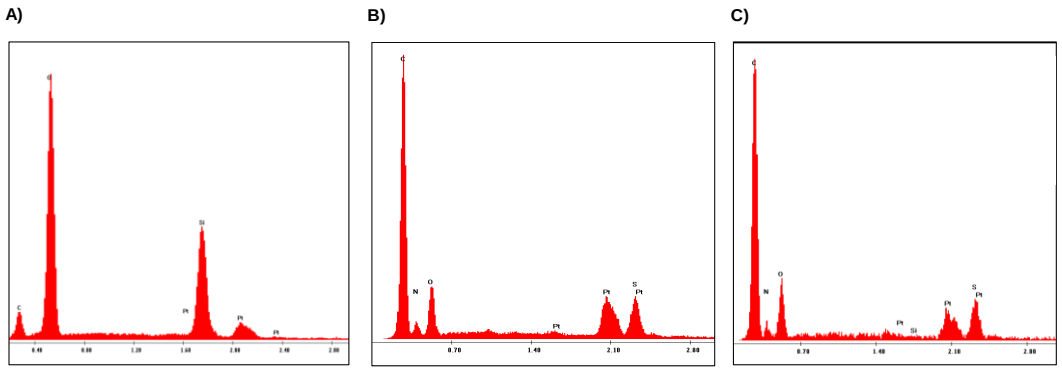

Fig 5S-4 EDX spectra for the fabricated A) HMSN, B) TFC membrane, and C) a typical TFN membrane containing 0.05% HMSN.

Chapter 6

Statement of Authorship

Title of Paper	Polyethylenimine Modification of Silica Nanoparticles: a Positive Approach to Develop Sustainable Thin Film Nanocomposite Membranes
Publication Status	☐ Published ☐ Accepted for Publication ☐ Submitted for Publication ☑ Unpublished and Unsubmitted w ork w ritten in manuscript style
Publication Details	Masoumeh Zargar, Yusak Hartanto, Bo Jin*, Sheng Dai*

Principal Author

Name of Principal Author (Candidate)	Masoumeh Zargar		
Contribution to the Paper	Designing and performing the experiments, analysis of the results and writing the manuscript.		
Certification:	This paper reports on original research I conducted during the period of my Higher Degree by Research candidature and is not subject to any obligations or contractual agreements with a third party that would constrain its inclusion in this thesis. I am the primary author of this paper.		
Signature		Date	22/09/2015

Co-Author Contributions

By signing the Statement of Authorship, each author certifies that their stated contribution to the publication is accurate and that permission is granted for the publication to be included in the candidate's thesis.

Name of Co-Author	Yusak Hartanto		
Contribution to the Paper	Assistance in some characterizations.		
Signature		Date	22/09/2015

Name of Co-Author	Bo Jin		
Contribution to the Paper	Supervising the development of the work, assisting in the manuscript review and assessment.		
Signature		Date	22/9/2015

Name of Co-Author	Sheng Dai		
Contribution to the Paper	Supervising the development of the work, assisting in the data interpretation, manuscript review and assessment.		
Signature		Date	22/09/2015

Polyethyleneimine Modification of Silica Nanoparticles: a Positive Approach to Develop Sustainable Thin Film Nanocomposite Membranes

Masoumeh Zargar, Yusak Hartanto, Bo Jin*, Sheng Dai*

School of Chemical Engineering, The University of Adelaide, SA 5005, Australia

*Corresponding authors

E-mail: s.dai@adelaide.edu.au; bo.jin@adelaide.edu.au

6.1. Abstract

Incorporation of inorganic hydrophilic nanoparticles into the thin film composite (TFC) membranes is a beneficial approach to enhance the water permeability of these membranes. However, the incompatibility of introduced nanoparticles with the organic thin film polyamide (PA) layer of TFC membranes and their instability in the resulting thin film nanocomposite (TFN) structures are the challenges for their end-use industrial applications. Herein, hydrophilic polyethyleneime (PEI) modified silica nanoparticles (SN-PEI) were synthesized and introduced into the PA layer of TFC membranes. Our research objective is to improve the compatibility and stability of SN in the PA layer so as to improve TFN membranes' desalination performance. The successful fabrication and incorporation of SN-PEI into the TFC membranes have been confirmed through various analytical techniques. SN-PEI introduction to the TFC membranes could facilitate the formation of covalent bonds between SN-PEI and PA layer, improve the stability of SN in the organic PA and enhance the physicochemical properties of the resulting TFN membranes. The cross-flow filtration evaluation of the fabricated membranes displayed up to 46 % improvement in the water flux combined with higher NaCl rejections for the TFN membranes compared with the control TFC membrane. The higher hydrophilicity of the developed TFN membranes together with the improved stability of the introduced nanoparticles in the membranes can be dominative in their performance improvement.

Keywords: Thin film nanocomposite membrane; silica nanoparticles; polyethyleneimine; water flux; salt rejection.

6.2. Introduction

Thin film composite (TFC) membranes are the most popular membranes applied in industrial water and wastewater, especially in deselination, processes. However, the high energy and capital costs due to the low permeability and fouling associated with these membranes have been a challenge for their industrial applications [1, 2]. Therefore, there is an on-going need to improve the performance of TFC membranes in order to make them more technically and economically feasible [3, 4]. Development of nanotechnology has made nanoparticle incorporated membranes (TFN) very promising for enhancing the performance and efficiency of TFC membranes [5-7]. To date, a variety of nanomaterials have been used to enhance permeability and fouling resistance of the TFC membranes through either encapsulation of nanoparticles into the thin film layers of TFC membranes or direct deposition of them on the surface of the membranes, some of which include silica [8, 9], zeolite [6, 10, 11], silver [12, 13], titanium dioxide [14, 15], graphene oxide [4, 16], carbon nanotubes [7, 17], etc.

The surface deposition of nanoparticles after initial membrane formation is mainly used to alleviate fouling issue. The resulting surface modified TFC membranes usually face permeability loss due to the mass transfer resistance generated by the dense layer of nanomaterials. Moreover, the surface deposition of nanoparticles on the TFC membranes for large scale process could lead to substantial fabrication difficulty and production costs [5]. The other strategy of *in situ* incorporating nanomaterials into the thin film polyamide (PA) layer of TFC membranes has received increasing attention in recent years due to its positive influence on TFC membranes' surface properties and bulk PA structures, which may result in the simultaneous improvement of water flux and fouling resistance of the developed TFN membranes. For instance, Dong et al. incorporated clay nanofillers into the PA layer of TFC membranes and reported enhanced desalination performance together with strong antifouling capability of their developed TFN membranes [18].

Among different nanomaterials used for the fabrication of TFN membranes, silica nanoparticles (SN) have attracted considerable attention due to their high biocompatibility, mechanical stability and hydrophilicity [19]. The prospect for enhancing surface hydrophilicity and consequently permeability and fouling

resistance of the TFC membranes by introducing SN into the PA layers has been confirmed through several previous studies [8, 9, 19, 20]. However, the normal approach for the incorporation of SN is via physical interaction. Thus, the incorporated SN through this approach are unstable during the high pressure operations. The interaction of SN and other nanomaterials with PA could be improved through their surface functionalization which can enhance SN's reactivity with the PA and their stability. Zargar et al. studied the incorporation of amine and epoxy functionalized SN and reported enhanced properties for their developed TFN membranes due to the strong covalent interaction of functionalized SN with PA thin film monomers [21]. Polymer surface modification of nanomaterials used for the fabrication of nanocomposites can generate excellent integration and improved interface between the introduced nanofillers and the bulk polymer [22]. Hence, it is expected that the compatibility of SN with PA can be further improved by their polymer surface modification. To the best of our knowledge, no such study can be found in the literature on the incorporation of polymer surface modified nanoparticles into the thin film layer of TFC membranes.

Low molecular weight branched polyethylenimine (PEI) is a positive charged, non-toxic polymer that has primary, secondary and tertiary amines. Therefore, PEI is highly reactive and hydrophilic, and has antibacterial properties [23, 24]. Due to its peculiar characteristics, branched PEI has been widely used for various applications, such as the developing of adhesion promoter in cell culture and gene delivery vectors [25, 26], biosensors [27], heavy metals' chelating agents, antibacterial coatings [28, 29] and surface modifications [30, 31]. Surface modification of SN with PEI, producing a structure noted as SN-PEI, can make them capable to enteract with PA structure because of the primary amine groups of PEI which readily react with the acid chloride groups of the TMC monomers. Further, SN-PEI is expected to have higher hydrophilic properties resulting from excessive amine groups and high charge density of PEI. Therefore, the incorporation of SN-PEI into the TFC membranes might be a promising approach for improving the performance and properties of the resulting TFN membranes.

Herein, SN modified with low molecular weight branched PEI were applied to develop novel TFN membranes. Different concentrations of SN-PEI were introduced into the TFC membranes through dispersion of them in the aqueous phase during the

interfacial polymerization. Physicochemical properties and desalination performance of the resulting TFN membranes were systematically characterized. The modified membranes display improved physicochemical properties combined with higher water permeability and salt rejection compared with the control TFC membrane which did not contain nanoparticles.

6.3. Experimental

6.3.1. Materials

Commercial polyester non-woven fabric (100 µm) was kindly supplied by PURUIXIN-TOP-SCIENCE. Polysulfone (PSF, Udel P-1700) was kindly provided by Solvay Specialty Polymers and used to fabricate PSF support interlayer. An adjustable casting knife (Elcometer 3530/2, Elcometer, UK) was used for casting PSF support layer. 1-Methyl-2-pyrrolidinone (NMP, Anhydrous 99.5 %), polyethyleneimine (PEI-25, branched, MW ~ 800 Da), glutaraldehyde (GA, 25 % aqueous solution), 1, 3-phenylenediamine (MPD, >99 %), 1, 3, 5-benzenetricarbonyl trichloride (TMC, 98 %), n-hexane, tetraethyl orthosilicate (TEOS, >99 %) and (3-aminopropyl) trimethoxysilane (APTMS, 97 %) were all purchased from Sigma-Aldrich and used directly. Sodium chloride (NaCl) and aqueous ammonia solution (28 %) were obtained from VWR International.

6.3.2. Fabrication of PEI modified silica nanoparticles (SN-PEI)

SN with an average size of ~ 100 nm were fabricated according to a modified Stöber approach [32]. Briefly, 50 ml absolute ethanol, 2.04 ml of 28 % aqueous ammonia and 0.9 ml Milli-Q water were mixed in a container followed by the quick injection of 2.9 ml of TEOS. The solution was stirred at 25 ºC for 24 h. The obtained SN were washed four times with absolute ethanol.

PEI modified SN (SN-PEI) were fabricated using a three stage procedure [26]. A modified approach from Chang et al. was applied to functionalize the surface of nanoparticles with amine groups [33]. 300 mg of the synthesized SN were dispersed in 80 ml of ethanol and degassed with nitrogen for 1 h. This was followed by increasing the temperature to 80 ºC and the quick injection of 400 µL APTMS to the reaction vessel. The solution was then refluxed for 6 h. After centrifugation and washing with ethanol and water for three times, amine-functionalized SN (SN-NH_2)

was obtained. SN-NH_2 was then mixed with 30 ml phosphate buffer solution (PBS, pH=7.4) and sonicated for around 30 min followed by the addition of 0.5 ml GA and stirring at room temperature for 6 h. The GA functionalized nanoparticles (SN-GA) were washed with ethanol for three times. Finally, 250 mg SN-GA was dispersed in 50 ml PEI aqueous solution (0.5 mg/ml) and stirred for 6 h at room temperature. The particles were then washed with ethanol for several times to obtain the SN-PEI.

6.3.3. Fabrication of TFC/TFN membranes

PSF support membranes were synthesized using the phase inversion process. In detail, 2 wt % PVP and 15 wt % PSF beads were dissolved in 83 wt % NMP in turn. The mixture was stirred at room temperature for several hours. The obtained clear homogenous solution was then degassed in an ultrasonication bath equipped with degassing function for 4 h. Subsequently, the commercial non-woven fabric was tapped to a glass plate and wetted with degassed NMP. Excessive NMP was removed by rolling a soft rubber roller on the surface of fabric followed by tap drying the fabric by tissue. The above-prepared PSF solution was then casted on the polyester fabric using an adjustable casting knife with a fixed gap height at 250 µm. The glass plate was immediately immersed in a precipitation bath containing distilled water at 20 °C to initiate phase inversion process. The precipitated PSF supports were allowed to stay in the bath for at least 30 min to ensure complete phase separation and then washed thoroughly with distilled water and stored in distilled water at 5 °C for further experiments.

In order to fabricate the PA selective barrier layer of TFC membranes, the synthesized PSF support was clamped between an acrylic plastic plate, a rubber gasket and an acrylic plastic frame on the top of that. 2 % (w/v) MPD aqueous solution was poured inside the frame and allowed to soak for 5 min. The excess MPD solution was then drained and the frame was disassembled followed by rolling the PSF support with a soft rubber roller until no visible droplets were remained on the surface of the support. At the next stage, 0.075 % (w/v) TMC in n-hexane solution was poured into the frame and allowed to react with the adsorbed MPD for 1 min resulting in the formation of an ultra-thin PA selective layer over the surface of PSF support. The excess organic phase was then drained and the membrane was air-dried for 1 min followed by heat curing in a recirculating oven set at 60 °C for 5 min.

The fabricated TFC membranes were then washed with 20 °C distilled water and stored in distilled water at 5 °C for further characterization and evaluations. For the SN-PEI incorporated TFC (TFN) membranes, different concentrations of SN-PEI (0.025 wt %, 0.05 wt % and 0.1 wt %) were mixed with MPD aqueous solution and sonicated for 1 h to fully disperse them immediately before initiating the interfacial polymerization. 0.025 % incorporation is noted as 0.03 in this study.

6.3.4. Characterization

Malvern Zetasizer Nano ZS (Malvern Inst. Ltd.) was used to study the hydrodynamic size distributions of the fabricated nanoparticles and their zeta potentials (based on electrophoresis measurements) at room temperature. Attenuated total reflectance Fourier transform infrared spectroscopy (ATR-FTIR) was performed using a NICOLET 6700 spectrometer equipped with a diamond ATR to study the chemical structures of the samples. To evaluate the surface modification of nanoparticles, thermogravimetric analysis (TGA) was performed by a TGA/DSC 2 STAR System. To perform the TGA analysis, ~ 5 mg sample was loaded in the Alumina crucible and heated from 30 °C to 800 °C at a heating rate of 10 °C/min under air with 50 ml/min flow. The heating methodology was involved an isotherm at 120 °C for 1 h to remove the adsorbed water. The normalized weight loss of each sample after this isotherm was calculated and reported. A scanning electron microscope (FEI Quanta 450 FEG Environmental SEM) equipped with an energy-dispersive X-ray (EDX) detector for elemental mapping was used to study the structure of fabricated nanoparticles and membranes. The prepared samples were dried overnight and sputter coated with 3-5 nm layer of platinum using a CRESSINGTON 208 high-resolution sputter coater before imaging. The SEM images were taken at a voltage of 10 kV and a working distance of 10 mm. FEI Tecnai G2 Spirit Transmission Electron Microscope was used at an accelerating voltage of 100 kV to further study the nanoparticles' structure. TEM samples were prepared by pouring one drop of the nanoparticle ethanol solution on carbon coated 200 mesh copper grids and air dried before imaging. A Kratos Axis Ultra X-ray photoelectron spectroscopy (XPS) was used to obtain the samples' constituent elements and their atomic percentages. XPS was run with a monochromatic aluminium x-ray at 225 W and characteristic energy of 1486.6 eV with the electron take off angle of normal to the sample surface. The scan range of the spectra was -10 to 1110 eV with 500 meV steps and 160 eV pass

energy and the analysis area (Iris aperture) was 0.3 mm x 0.7 mm. Charge neutraliser system was used to reduce the surface charge of samples and give high resolution XPS spectra. The obtained survey spectra were interpreted using the CasaXSP software package. Contact angles were measured on an Attension Theta Optical tensiometer system in sessile drop mode at room temperature using milli-Q water as the liquid and the dispensing volume of 1 µl. Curve fitting and data analysis was performed using OneAttension software. The reported contact angles were the average of at least 8 different positions on each membrane.

6.3.5. Membrane performance evaluation

The performance evaluation of the fabricated membranes was performed on a cross-flow filtration unit (CF042, Sterlitech) with an effective surface area of 42 cm^2. Before starting the actual tests, the membranes were compacted with distilled water at 1.5 MPa and 25±0.1 °C to reach equilibrium flux. 15 L of 2000 mg/L NaCl solution was then circulated in the system at the specified pressure and temperature and the fixed concentrate flow rate of 4 L/min. During the filtration tests, the concentrate flow was returned back to the feed tank and the permeate flow was collected on a digital balance. The permeate weight was recorded using a LabX Direct Software (Mettler Toledo) in a continuous mode and the flux (*J*) was calculated using Equation 1 accordingly. To obtain the salt rejection values, permeate and feed water conductivities were measured using a conductometer (AQUA, Cond. / pH, TPS, k = 1.0), and the values were converted to the equivalent salt concentrations using a pre-calibration curve. Equation 2 was then used to calculate the equivalent salt rejections.

$$J = \frac{V_P}{\mathrm{A.\,t}} \qquad (1)$$

$$R\,\% = \left(1 - \frac{C_P}{C_F}\right) \times 100 \qquad (2)$$

where *J* is the permeate water flux (LMH), V_P is the permeate volume (l), *A* is the active membrane surface area (m^2), *t* is the operation time (h), *R* is the salt rejection and C_P and C_F are the equivalent NaCl concentrations in collected permeate and feed water, respectively.

6.4. Results and Discussion

6.4.1. Synthesis and characterization of the surface modified nanoparticles

A multi-step fabrication strategy was performed to fabricate SN-PEI. The schematic illustration of the fabrication approach is illustrated in Fig 6-1.

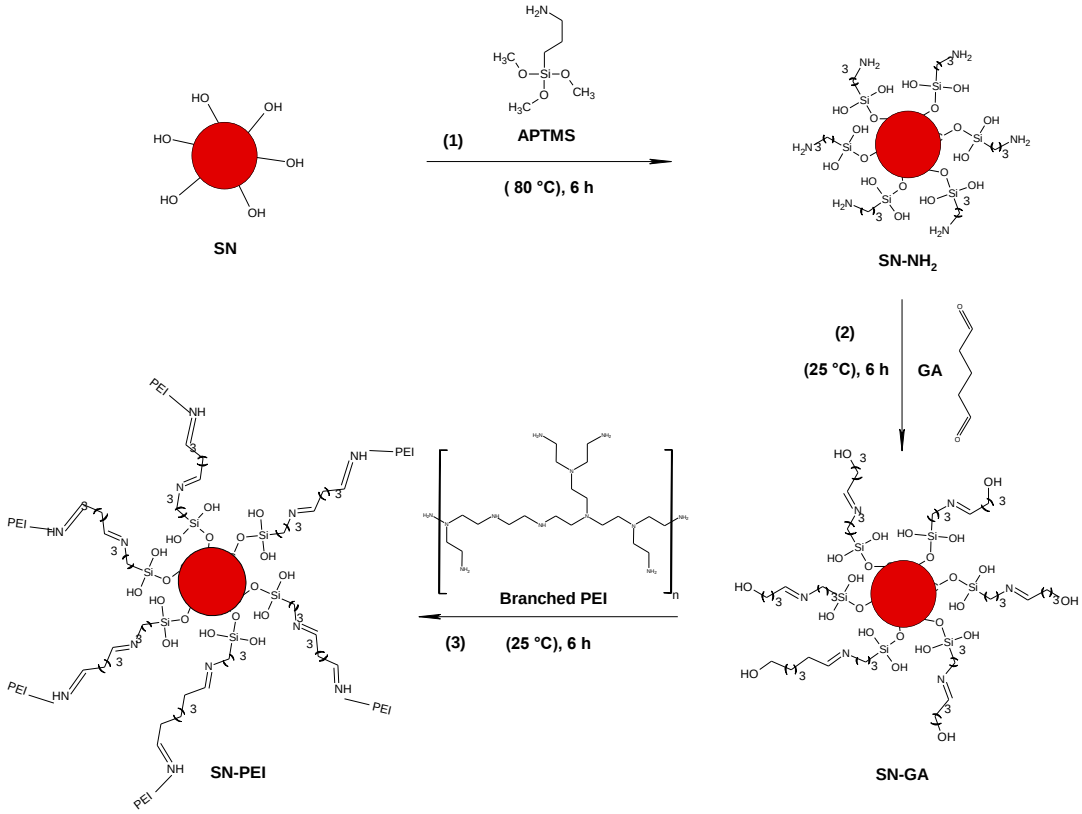

Figure 6-1 The schematic description of the general strategy to fabricate SN-PEI.

The obtained nanoparticles were characterized using various analytical techniques. Table 6-1 shows the average hydrodynamic sizes and the zeta potentials of the SN, SN-NH_2 and SN-PEI. The hydrodynamic size of SN is 118±7, which is increased after various surface modifications. That can be attributed to the formation of thicker surface hydration layers due to the presence of excessive hydrophilic amine functional groups [9]. The zeta potentials vary from negative to positive for the SN compared with SN-NH_2 and SN-PEI which can be associated to the introduction of surface amine groups on the SN-NH_2 and SN-PEI. SN-PEI has a larger zeta potential compared with SN-NH_2 which is due to the larger quantity of the amine groups in

PEI and hence SN-PEI compared with SN-NH_2. The zeta potentials of > 15 mV confirm the high aqueous stability of these nanoparticles in the water phase.

Table 6-1 Hydrodynamic sizes and zeta potentials of SN, SN-NH_2 and SN-PEI.

Nanoparticles	Hydrodynamic Diameter (nm)	Zeta potential (mV)
SN	118±7	-32±4
SN-NH_2	126±17	17±4
SN-PEI	151±28	31±6

Fig 6S-1 in the Supporting Information presents the FTIR spectra for SN, SN-NH_2 and SN-PEI. All spectra show the typical characteristic peaks of silica at ~ 787, 950 and 1050 cm^{-1}, corresponding to the vibrations of Si-O-Si symmetric bond, Si-OH stretching bond and Si-O-Si asymmetric bond [34]. The observed peak at around 1635 cm^{-1} is due to physisorbed water. The small percentage of surface functional groups compared with the bulk SN makes the silica peaks dominant. Hence, except for the range of 1400-1600 cm^{-1}, which is highlighted in Fig 6S-1, no discernible difference is observed among the obtained FTIR spectra. Characteristic vibration peaks at ~ 1442 cm^{-1}, corresponding to the C-H bond of the methyl groups of APTMS and PEI, and ~ 1540 cm^{-1}, corresponding to the amine groups of SN-NH_2 and SN-PEI, are emerged in this region [35].

The surface functionalization and PEI modification can be further confirmed through TGA analysis. Fig 6-2 presents the TGA themograms corresponding to SN, SN-NH_2 and SN-PEI which shows a progressive increase in the weight loss after each functionalization. SN experienced 2.9 % residual weight loss that can be attributed to the dihydroxylation of their surface hydroxyl groups [36]. For the SN-NH_2, the particles lost 5.6 % of their residuals weight which is attributed to the decomposition of surface amine moieties in addition to the dihydroxylation of the remained surface hydroxyl groups on the nanoparticles. For the SN-PEI, the residual weight loss is 12.4 %. The SN-PEI thermogram shows a sharp decomposition stage up to ~ 600 ºC having the onset decomposition temperature (T_d) of 336 ºC. That can be correlated to the oxidation and decomposition of PEI at ~ 150-600 ºC and the dehydroxylation of remained hydroxyl groups [37]. TGA data can be used to estimate the number of PEI chains on each SN. The nanoparticles are assumed to have homogeneous spherical shape and the whole 9.5 % residual weight loss difference of SN-PEI and SN is

assumed to be due to the PEI decomposition. Considering these, the PEI grafting density corresponds to 2.62 PEI_{800}/nm^2.

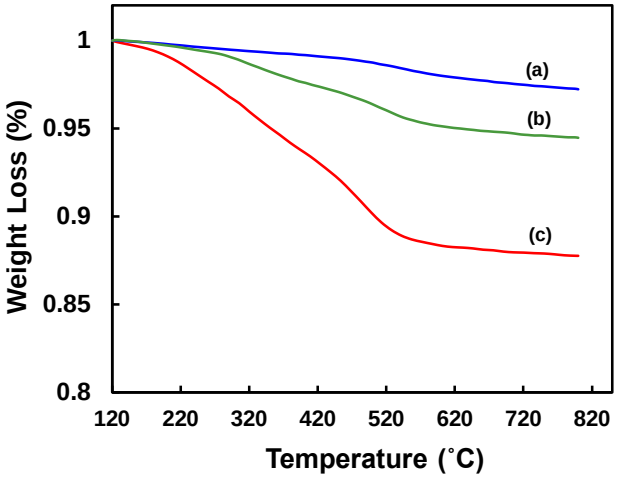

Figure 6-2 TGA thermograms for: a) SN, b) SN-NH_2, and c) SN-PEI.

Fig 6-3 shows the SEM and TEM images and the EDX spectra for the fabricated SN and SN-PEI nanoparticles.

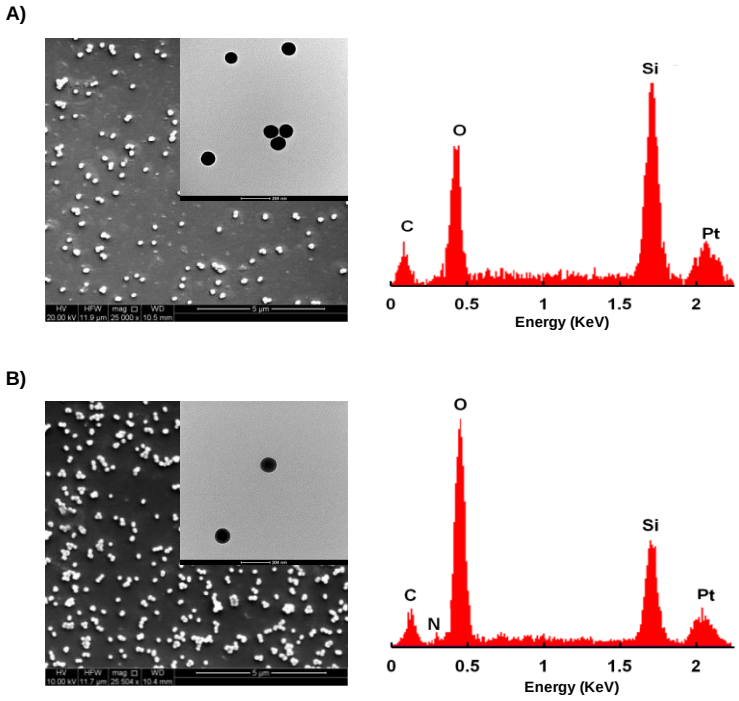

Figure 6-3 SEM images, TEM images (inset), and EDX spectra for A) SN, and B) SN-PEI. The scale bars are 200 nm for TEM images and 5 µm for SEM images.

As shown, the particles are spherical and monodisperse and have an average particle size of ~ 100 nm. The emergence of nitrogen peak in the EDX spectra associated

with the SN-PEI nanoparticles indicates the successful surface modification of SN. It should be also noted that the particle size obtained using TEM is slightly smaller than the hydrodynamic diameter of particles obtained from DLS measurement which is due to the hydration layer formed on the particles in their aqueous DLS sample while the size given by TEM is the dried sample size.

To further identify the surface modification success, XPS analysis was performed on the SN, SN-NH_2 and SN-PEI. The elemental composition of the samples is presented in Table 6-2. Carbon has been increased for the SN-PEI compared with SN and SN-NH_2 while nitrogen has emerged for both SN-NH_2 and SN-PEI samples with a larger value for SN-PEI compared with SN-NH_2. The increase in C element is due to the additional carbon induced on the surface of SN-PEI from the PEI backbone monomers. The high atomic composition of N in SN-PEI is due to the large quantity of amine groups in PEI. XPS analysis further confirms the successful surface modification of SN with PEI.

Table 6-2 XPS analysis for SN, SN-NH_2 and SN-PEI.

Sample Name	Atomic percentage of elements			
	N (%)	O (%)	C (%)	Si (%)
SN	-	59.53	21.17	19.3
SN-NH_2	1.92	56.14	21.68	20.26
SN-PEI	3.89	39.83	41.90	14.38

6.4.2. Characterization of TFC and TFN membranes

The top, bottom and cross-section morphology of the fabricated PSF membrane used as the PA support is presented in Fig 6S-2. As shown, PSF membrane has large macrovoids with open pores on the bottom and surface pores of ~ 20 nm. Fig 6-4 represents the high and low resolution SEM images from the surface of fabricated TFC/TFN membranes. The rugose structure with leaf-like folds, as observed for the control TFC membrane, is the expected surface morphology for the PA membranes fabricated through the MPD-TMC system [38]. However, the decrease of leaf-like folds and the presence of more nodular features on the surface of the TFN membranes suggest the different interactions of the PA monomers due to the nanoparticles' integration.

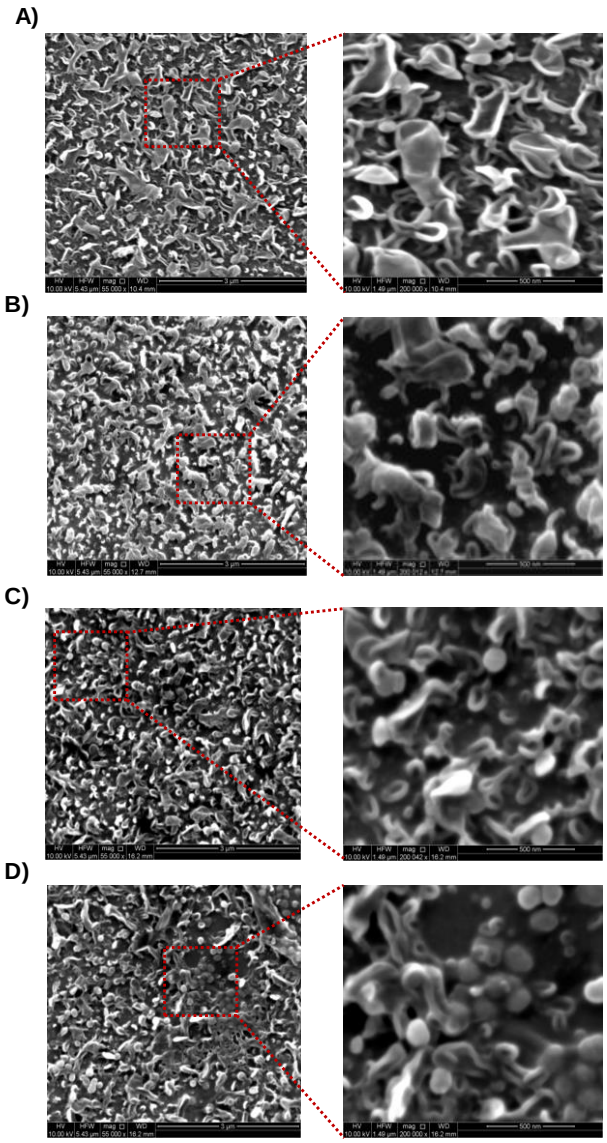

Figure 6-4 High and low magnification SEM surface images of the fabricated membranes: A) control TFC, B) TFN incorporated with 0.03 wt % SN-PEI C) TFN incorporated with 0.05 wt % SN-PEI, and D) TFN incorporated with 0.1 wt % SN-PEI.

Incorporation of SN-PEI with a large quantity of NH_2 surface functional groups can alter the PA monomers interactions through consuming some of the carboxylic chloride groups of TMC by SN-PEI rather than MPD. The covalent bond formation between SN-PEI and PA makes the nanoparticles more stable in the fabricated nanocomposites and can be beneficial for the long term optimum performance of the developed TFN membranes. The interaction of SN-PEI and PA is evident from the surface SEM image taken from an apparently defected area on the TFN membrane incorporated with 0.1 wt % SN-PEI (Fig 6S-3). SN-PEI is clearly connected, though partially, with the surface features of PA which can justify the different surface

morphology of the fabricated TFN membranes compared with the control TFC membrane.

Fig 6-5 A, D show the cross-section SEM images from TFC membrane and a typical TFN membrane containing 0.1 wt % SN-PEI. The thickness of PA layer has not been significantly changed in the cross-section SEM image. However, images taken from a tilted area on the membranes, which are presented in Fig 6-5 B, E, clearly show the difference in the surface features of these two membranes and a more clear view of the embedded nanoparticles in the PA layer of the TFN membrane. Fig 6-5 C, F show the EDX mapping spectra obtained from the surface of the tilted cross-section SEM samples. The emergence of silicon peak at 1.740 Kev in the TFN spectra again confirms the successful incorporation of SN-PEI into the TFN membrane.

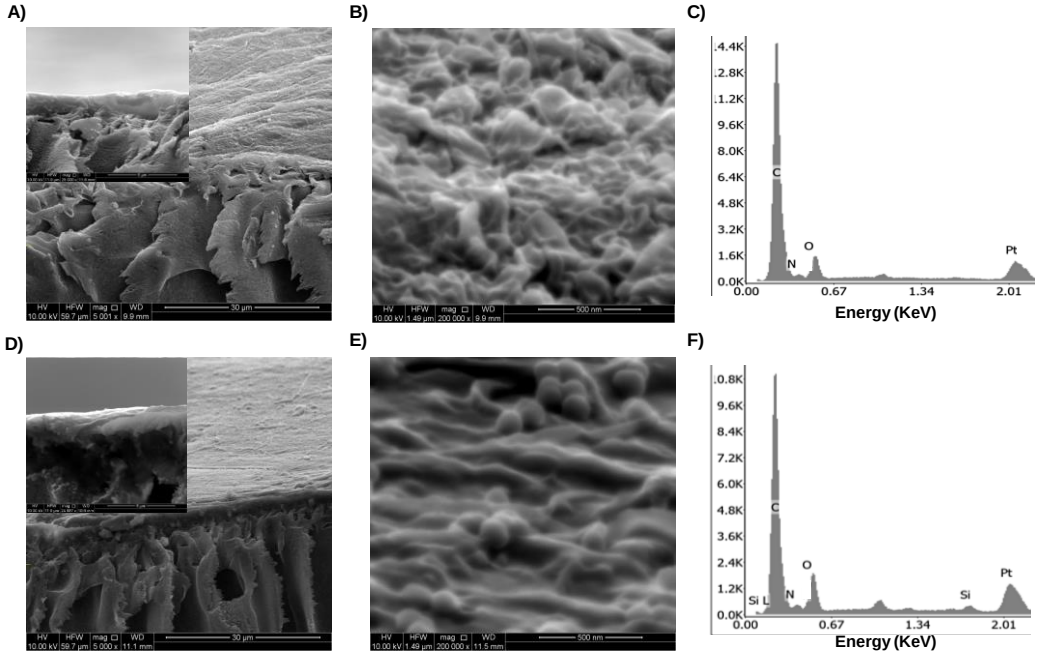

Figure 6-5 A) SEM cross-section image, B) surface SEM image obtained from the tilted cross-section SEM sample, and C) EDX spectra obtained through EDX mapping for the control TFC membrane; and D) SEM cross-section image, E) surface SEM image obtained from the tilted cross-section SEM sample, and F) EDX spectra obtained through EDX mapping for the TFN membrane incorporated with 0.1 wt % SN-PEI.

Fig 6-6 presents the contact angles of the fabricated TFN membranes as a function of SN-PEI loading concentration. The contact angle of membranes decreases from 61.69º to 41.18º by increasing SN-PEI concentration from 0 to 0.1 wt % in the PA layer which is due to the surface hydrophilic groups of the SN-PEI [39]. This observation agrees with those reported studies for TFN membranes incorporated with

hydrophilic nanoparticles [40, 41], or surface modified with hydrophilic polymers [42, 43]. For instance, Zargar et al. reported a decrease in the contact angle of their TFN membranes incorporated with hydrophilic silica having hydroxyl, epoxy and amine functional groups compared with the control TFC membrane [21]. Lower contact angles indicate the higher hydrophilicity of membrane surfaces and can be beneficial for their permeability enhancement [5, 44].

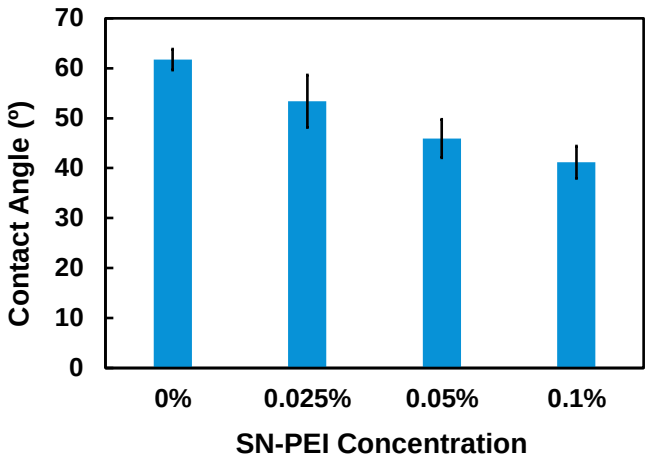

Figure 6-6 The comparison of the contact angles of various fabricated TFC and TFN membranes.

XPS analysis was performed on SN-PEI, TFC and a typical TFN membrane containing 0.05 wt % SN-PEI to identify the elemental composition of fabricated samples in addition to the chemical structure of the PA layer after SN-PEI introduction. The survey XPS spectra of the samples are shown in Supporting Information Fig 6S-3 and Table 6-3 lists the constituents' elements and their atomic percentages of the samples. The thin PA layer of control TFC membrane contain carbon, hydrogen, oxygen and nitrogen with their core-electron binding energies at 284.5 eV for C 1s, 396.0 eV for N 1s and 531.6 eV for O 1s. Since hydrogen cannot be detected by XPS due to its small photoelectron cross-section, its atomic concentration is excluded from the elemental analysis of samples [45]. In the case of TFN membrane, in addition to the C, N and O peaks, two new small peaks at 97.5 eV and 155.0 eV, which are attributed to Si 2p and Si 2s, are also emerged [46]. That confirms the successful incorporation of SN-PEI in the TFN membrane. N/O ratio is typically accepted as an indication of the PA thin films' cross-linking density in a way that a larger N/O indicates the formation of a more cross-linked PA structure [10, 45, 47]. Since SN-PEI has the same elements as PA, the corrected N/O ratio

noted as N/O* is calculated by considering the elemental composition of SN-PEI and used for comparison. As shown in Table 6-3, the cross-linking density of PA has increased after SN-PEI incorporation which can be attributed to the covalent bond formation between the amine groups of SN-PEI and carboxylic chloride functional groups of TMC monomer.

Table 6-3 XPS analysis for SN-PEI, TFC and the TFN membrane with 0.05 wt % SN-PEI.

Sample	Atomic percentage of elements					
	N (%)	O (%)	C (%)	Si (%)	N/O	N/O*
SN-PEI	3.89	39.83	41.90	14.38	-	-
TFC	10.78	14.17	74.99	-	0.76	0.76
TFN	11.06	12.62	76.09	0.23	0.87	0.91

6.4.3. Performance evaluation of TFC and TFN membranes

The membrane performance evaluation in terms of water flux and salt rejection was performed on the TFC/TFN membranes using a cross-flow filtration unit. Fig 6-7 presents the performance results of various TFN membranes as a function of SN-PEI loading.

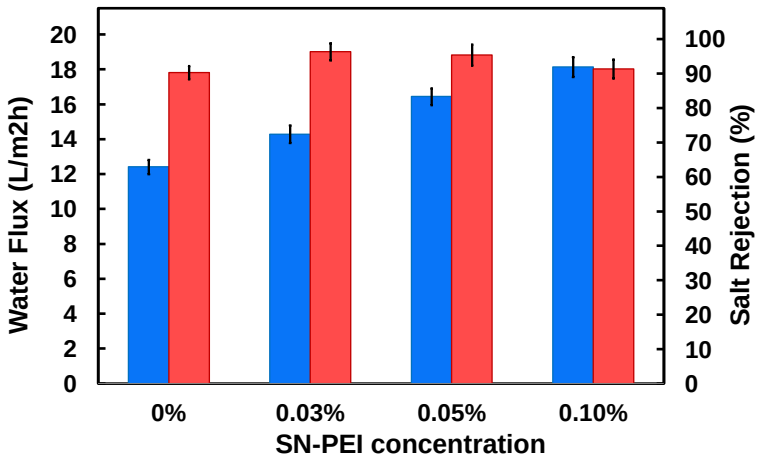

Figure 6-7 Performance evaluation for the fabricated TFC/TFN membranes in terms of water flux and salt rejection as a function of SN-PEI loading.

Water flux increases up to ~ 46 % for the TFN membranes as the concentration of SN-PEI increases. That can be resulted from the new properties of the developed TFN membranes. Incorporation of PEI modified nanoparticles enhances the surface hydrophilicity of TFN membranes as evidenced by the contact angle results which

contributes to higher water affinity of the TFN membranes. In addition, incorporation of SN-PEI introduces some interparticle voids in the PA layer that can contribute to the higher water permeation across the PA layer.

Fig 6-8 shows the compaction rates for the fabricated membranes obtained through measuring the water flux as a function of time during the membrane compaction stage.

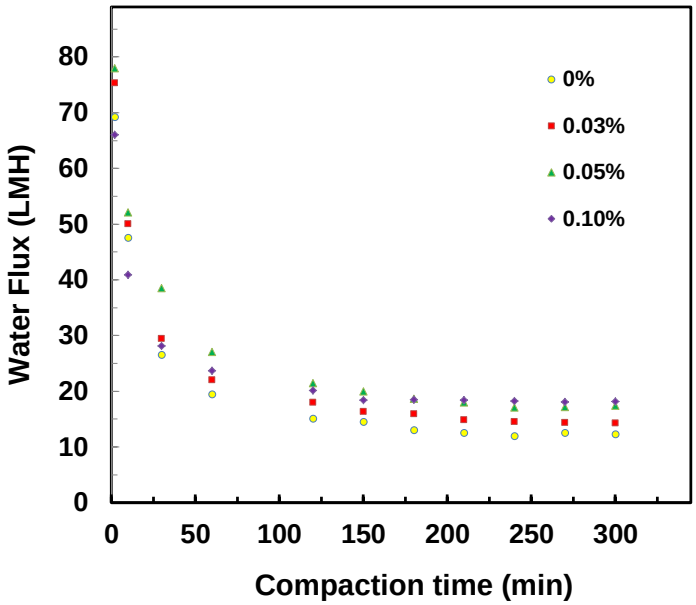

Figure 6-8 The water flux of the fabricated TFC and TFN membranes versus compaction time at 1.5 MPa and 25±0.1 ºC.

The compaction resistance of membranes slightly improves following the incorporation of SN-PEI with the ratios of 82.07 %, 81.02 %, 77.5 % and 72.5 % for the TFC, 0.03 wt %, 0.05 wt % and 0.1 wt % SN-PEI incorporated TFC membranes. Compaction results suggest that the integration of SN-PEI with the PA layer can be beneficial for strengthening the resulting TFN membranes. Prendergast et al. also reported a higher compaction resistance for their TFN membranes (incorporated with zeolite nanoparticles) compared with TFC membrane [48].

It is interesting to note that the TFN membrane incorporated with 0.03 wt % SN-PEI demonstrated 6.8 % increase in their salt rejection compared with the control TFC membrane. Further increase of the nanoparticles' loading, for instance, TFN membranes incorporated with 0.05 wt % and 0.1 wt % SN-PEI, results in declining the salt rejection for 1.1 % and 5.2 %. Considering the performance results of the

fabricated membranes, it seems that 0.05 wt % can be considered as the optimum SN-PEI incorporation concentration with which by applying a moderate amount of nanoparticles, a desirable level of improvement in both water flux and salt rejection can be achieved.

In general, the TFN membranes show higher salt rejection compared with the control TFC membrane. That can be correlated to the higher cross-linking density of the TFN membranes resulting from the covalent bond formation between amine groups of SN-PEI and carboxylic chloride groups of TMC monomer. These results can be evidenced by XPS analysis of the typical TFN membrane incorporated with 0.05 wt % SN-PEI. The dropping trend observed for the salt rejection of the TFN membranes by increasing the SN-PEI loading can be explained by some possible reasons. First, small voids can be unavoidably introduced at the organic-inorganic interface in the PA which their quantity increases by nanoparticle loading concentration increment as reported previously [10, 11]. That can contribute to the simultaneous higher permeation of the salt and water molecules. Lind et al. performed a pioneer study on the performance of TFN membranes incorporated with zeolite nanoparticles at different sizes and with different PA chemistries. They suggested that the incorporation of zeolite nanoparticles could change the bulk PA structure and generate some voids in the PA, and as a result decrease the TFN membranes' salt rejection [10]. Similarly, the incorporation of other nanomaterials can influence the porosity of PA layer. Further, slight aggregation of nanoparticles might happen at the high loading concentrations which can generate some defects in the PA layer and decrease its selectivity as reported in the literature [11, 49]. Presence of some SN-PEI aggregates at 0.1 wt % loading can be observed in SEM surface and cross-section images of the resulting TFN membrane shown in Fig 6-4D and Fig 6-5E.

Overall, our developed TFN membranes display improved water flux and salt rejection in comparison to the control TFC membrane which suggests the positive influence of introducing SN-PEI into the PA layer of TFC membranes.

6.5. Conclusions

PEI modified silica nanoparticles with an average particle size of ~ 100 nm were fabricated and incorporated into the TFC membranes. The physicochemical

properties and desalination performance of the resulting TFN membranes have been extensively characterized. The surface charge and the hydrodynamic diameter of the fabricated nanoparticles change after surface functionalizing. XPS and EDX spectra also confirm the successful surface modification of the nanoparticles and their incorporation into the PA layer of TFN membranes. Introduction of SN-PEI to the TFC membranes facilitates the formation of hydrophilic TFN membranes with more cross-linked PA layer. As a result, the developed TFN membranes show higher water flux and salt rejection compared with the control TFC membrane. Surface modification of SN with polymers having the same end cap functional groups as PA monomers (MPD in this case) can strenghten the integration of nanoparticles with PA structure through covalent binding. This coincides with the higher compatibility of polymer coated nanoparticles with the PA and can facilitate the sustainble improvement of the performance and properties of the developed TFN membranes.

References

[1] J.P. Chen, E.S.K. Chian, P.X. Sheng, K.G.N. Nanayakkara, L.K. Wang, e.P. Ting, Desalination of Seawater by Reverse Osmosis, in: L.K. Wang, J.P. Chen, Y.T. Hung, N.K. Shammas (Eds.) Membrane and Desalination Technologies, Springer, New York Dordrecht Heidelberg London, 2011.

[2] D. Li, H. Wang, Development of reverse osmosis membranes in desalination: a review, in: Chemeca 2010: Engineering at the Edge, Barton, A.C.T.: Engineers Australia, Hilton Adelaide, South Australia, 2010, pp. 490-499.

[3] M. Elimelech, W.A. Phillip, The future of seawater desalination: energy, technology, and the environment, Science, 333 (2011) 712-717.

[4] H.M. Hegab, A. ElMekawy, T.G. Barclay, A. Michelmore, L. Zou, C.P. Saint, M. Ginic-Markovic, Fine-tuning the surface of forward osmosis membranes via grafting graphene oxide: performance patterns and biofouling propensity, ACS Applied Materials & Interfaces, 7 (2015) 18004-18016.

[5] G.D. Kang, Y.M. Cao, Development of antifouling reverse osmosis membranes for water treatment: A review, Water Research, 46 (2012) 584-600.

[6] S.G. Kim, D.H. Hyeon, J.H. Chun, B.H. Chun, S.H. Kim, Nanocomposite poly(arylene ether sulfone) reverse osmosis membrane containing functional zeolite nanoparticles for seawater desalination, Journal of Membrane Science, 443 (2013) 10-18.

[7] H. Zhao, S. Qiu, L. Wu, L. Zhang, H. Chen, C. Gao, Improving the performance of polyamide reverse osmosis membrane by incorporation of modified multi-walled carbon nanotubes, Journal of Membrane Science, 450 (2014) 249-256.

[8] G.L. Jadav, P.S. Singh, Synthesis of novel silica-polyamide nanocomposite membrane with enhanced properties, Journal of Membrane Science, 328 (2009) 257-267.

[9] A. Tiraferri, Y. Kang, E.P. Giannelis, M. Elimelech, Highly hydrophilic thin-film composite forward osmosis membranes functionalized with surface-tailored nanoparticles, ACS Applied Materials & Interfaces, 4 (2012) 5044-5053.

[10] M.L. Lind, A.K. Ghosh, A. Jawor, X. Huang, W. Hou, Y. Yang, E.M.V. Hoek, Influence of zeolite crystal size on zeolite-polyamide thin film nanocomposite membranes, Langmuir, 25 (2009) 10139-10145.

[11] H. Dong, L. Zhao, L. Zhang, H. Chen, C. Gao, W.S. Winston Ho, High-flux reverse osmosis membranes incorporated with NaY zeolite nanoparticles for brackish water desalination, Journal of Membrane Science, 476 (2015) 373-383.

[12] J. Yin, Y. Yang, Z. Hu, B. Deng, Attachment of silver nanoparticles (AgNPs) onto thin-film composite (TFC) membranes through covalent bonding to reduce membrane biofouling, Journal of Membrane Science, 441 (2013) 73-82.

[13] Y. Liu, E. Rosenfield, M. Hu, B. Mi, Direct observation of bacterial deposition on and detachment from nanocomposite membranes embedded with silver nanoparticles, Water Research, 47 (2013) 2949-2958.

[14] R.X. Zhang, L. Braeken, P. Luis, X.L. Wang, B. Van der Bruggen, Novel binding procedure of TiO_2 nanoparticles to thin film composite membranes via self-polymerized polydopamine, Journal of Membrane Science, 437 (2013) 179-188.

[15] D. Emadzadeh, W.J. Lau, T. Matsuura, A.F. Ismail, M. Rahbari-Sisakht, Synthesis and characterization of thin film nanocomposite forward osmosis membrane with hydrophilic nanocomposite support to reduce internal concentration polarization, Journal of Membrane Science, 449 (2014) 74-85.

[16] L. He, L.F. Dumée, C. Feng, L. Velleman, R. Reis, F. She, W. Gao, L. Kong, Promoted water transport across graphene oxide–poly(amide) thin film composite membranes and their antibacterial activity, Desalination, 365 (2015) 126-135.

[17] L. Dumée, J. Lee, K. Sears, B. Tardy, M. Duke, S. Gray, Fabrication of thin film composite poly(amide)-carbon-nanotube supported membranes for enhanced performance in osmotically driven desalination systems, Journal of Membrane Science, 427 (2013) 422-430.

[18] H. Dong, L. Wu, L. Zhang, H. Chen, C. Gao, Clay nanosheets as charged filler materials for high-performance and fouling-resistant thin film nanocomposite membranes, Journal of Membrane Science, 494 (2015) 92-103.

[19] L. Jin, W. Shi, S. Yu, X. Yi, N. Sun, C. Ma, Y. Liu, Preparation and characterization of a novel PA-SiO_2 nanofiltration membrane for raw water treatment, Desalination, 298 (2012) 34-41.

[20] A. Peyki, A. Rahimpour, M. Jahanshahi, Preparation and characterization of thin film composite reverse osmosis membranes incorporated with hydrophilic SiO_2 nanoparticles, Desalination, 368 (2015) 152-158.

[21] M. Zargar, Y. Hartanto, B. Jin, S. Dai, Understanding functionalized nanoparticle incorporation in thin film composite membranes: interactions and desalination performance Journal of Membrane Science, Submitted (2015) (JMS-15-1287).

[22] R.Y. Hong, Q. Chen, Organic-inorganic hybrid nanomaterials, in: S. Kalia, Y. Haldorai (Eds.) Advances in Polymer Science, Springer International Publishing, 2015.

[23] C. Feng, J. Xu, M. Li, Y. Tang, C. Gao, Studies on a novel nanofiltration membrane prepared by cross-linking of polyethyleneimine on polyacrylonitrile substrate, Journal of Membrane Science, 451 (2014) 103-110.

[24] J. Xu, Z. Wang, J. Wang, S. Wang, Positively charged aromatic polyamide reverse osmosis membrane with high anti-fouling property prepared by polyethylenimine grafting, Desalination, 365 (2015) 398-406.

[25] D. Şen Karaman, T. Gulin-Sarfraz, G. Hedström, A. Duchanoy, P. Eklund, J.M. Rosenholm, Rational evaluation of the utilization of PEG-PEI copolymers for the facilitation of silica nanoparticulate systems in biomedical applications, Journal of Colloid and Interface Science, 418 (2014) 300-310.

[26] L. Xiong, X. Du, B. Shi, J. Bi, F. Kleitz, S.Z. Qiao, Tunable stellate mesoporous silica nanoparticles for intracellular drug delivery, Journal of Materials Chemistry B, 3 (2015) 1712-1721.

[27] H.J. Yun, H. Hong, J. Lee, C.J. Choi, Chemical and structural properties of polyethyleneimine film coated on a SiO_2 substrate in different concentrations, Materials Transactions, 55 (2014) 801-805.

[28] T. He, V. Chan, Covalent layer-by-layer assembly of polyethyleneimine multilayer for antibacterial applications, Journal of Biomedical Materials Research Part A, 95A (2010) 454-464.

[29] J.D. Schiffman, Y. Wang, E.P. Giannelis, M. Elimelech, Biocidal activity of plasma modified electrospun polysulfone mats functionalized with polyethyleneimine-capped silver nanoparticles, Langmuir, 27 (2011) 13159-13164.

[30] P. Sunintaboon, S. Duangphet, P. Tangboriboonrat, Polyethyleneimine-functionalized poly(methyl methacrylate) colloidal nanoparticles for directly coating natural rubber sheet, Colloids and Surfaces A: Physicochemical and Engineering Aspects, 350 (2009) 114-120.

[31] B. Gao, P. Jiang, F. An, S. Zhao, Z. Ge, Studies on the surface modification of diatomite with polyethyleneimine and trapping effect of the modified diatomite for phenol, Applied Surface Science, 250 (2005) 273-279.

[32] W. Stöber, A. Fink, J. Colloid Interface Sci., 26 (1968) 62.

[33] B. Chang, D. Chen, Y. Wang, Y. Chen, Y. Jiao, X. Sha, W. Yang, Bioresponsive controlled drug release based on mesoporous silica nanoparticles coated with reductively sheddable polymer shell, Chemistry of Materials, 25 (2013) 574-585.

[34] J. Yin, E.S. Kim, J. Yang, B. Deng, Fabrication of a novel thin-film nanocomposite (TFN) membrane containing MCM-41 silica nanoparticles (NPs) for water purification, Journal of Membrane Science, 423–424 (2012) 238-246.

[35] J. Fujiki, K. Yogo, Carbon Dioxide Adsorption onto polyethylenimine-functionalized porous chitosan beads, Energy & Fuels, 28 (2014) 6467-6474.

[36] K. Möller, J. Kobler, T. Bein, Colloidal suspensions of nanometer-sized mesoporous silica, Advanced Functional Materials, 17 (2007) 605-612.

[37] X. Xu, C. Song, J.M. Andresen, B.G. Miller, A.W. Scaroni, Novel polyethylenimine-modified mesoporous molecular sieve of MCM-41 type as high-capacity adsorbent for CO_2 capture, Energy & Fuels, 16 (2002) 1463-1469.

[38] A.K. Ghosh, B.H. Jeong, X. Huang, E.M.V. Hoek, Impacts of reaction and curing conditions on polyamide composite reverse osmosis membrane properties, Journal of Membrane Science, 311 (2008) 34-45.

[39] W. Albrecht, B. Seifert, T. Weigel, M. Schossig, A. Holländer, T. Groth, R. Hilke, Amination of poly(ether imide) membranes using di- and multivalent amines, macromolecular chemistry and physics, 204 (2003) 510-521.

[40] B. Rajaeian, A. Rahimpour, M.O. Tade, S. Liu, Fabrication and characterization of polyamide thin film nanocomposite (TFN) nanofiltration membrane impregnated with TiO_2 nanoparticles, Desalination, 313 (2013) 176-188.

[41] N. Niksefat, M. Jahanshahi, A. Rahimpour, The effect of SiO_2 nanoparticles on morphology and performance of thin film composite membranes for forward osmosis application, Desalination, 343 (2014) 140-146.

[42] Y. Zhou, S. Yu, C. Gao, X. Feng, Surface modification of thin film composite polyamide membranes by electrostatic self deposition of polycations for improved fouling resistance, Separation and Purification Technology, 66 (2009) 287-294.

[43] S. Romero-Vargas Castrillón, X. Lu, D.L. Shaffer, M. Elimelech, Amine enrichment and poly(ethylene glycol) (PEG) surface modification of thin-film composite forward osmosis membranes for organic fouling control, Journal of Membrane Science, 450 (2014) 331-339.

[44] K.P. Lee, T.C. Arnot, D. Mattia, A review of reverse osmosis membrane materials for desalination—Development to date and future potential, Journal of Membrane Science, 370 (2011) 1-22.

[45] S.Y. Kwak, S.H. Kim, S.S. Kim, Hybrid organic/inorganic reverse osmosis (RO) membrane for bactericidal anti-fouling. 1. preparation and characterization of TiO_2 nanoparticle self-assembled aromatic polyamide thin-film-composite (TFC) membrane, Environmental Science & Technology, 35 (2001) 2388-2394.

[46] W. Li, S. Wang, S. He, J. Wang, Y. Guo, Y. Guo, Enhanced photoluminescence from CdS with SiO_2 nanopillar arrays, Scientific Reports, 5 (2015) 11375.

[47] S.H. Kim, S.Y. Kwak, T. Suzuki, Positron annihilation spectroscopic evidence to demonstrate the flux-enhancement mechanism in morphology-controlled thin-film-composite (TFC) membrane, Environmental Science & Technology, 39 (2005) 1764-1770.

[48] M.T.M. Pendergast, J.M. Nygaard, A.K. Ghosh, E.M.V. Hoek, Using nanocomposite materials technology to understand and control reverse osmosis membrane compaction, Desalination, 261 (2010) 255-263.

[49] H. Wu, B. Tang, P. Wu, Optimizing polyamide thin film composite membrane covalently bonded with modified mesoporous silica nanoparticles, Journal of Membrane Science, 428 (2013) 341-348.

6.6. Supporting Information

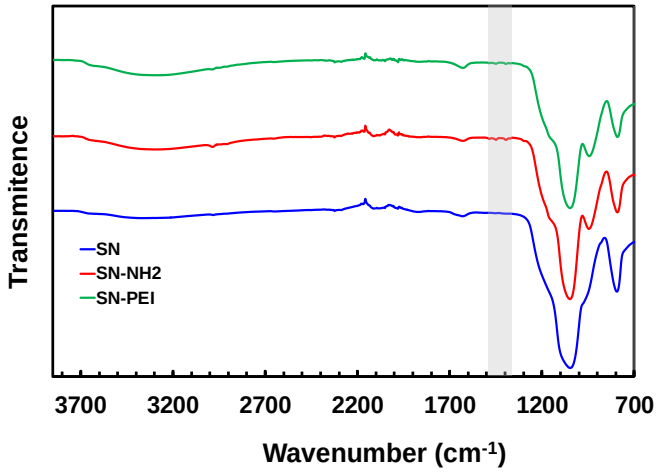

Fig 6S-1 FTIR spectra for the SN, SN-NH_2 and SN-PEI

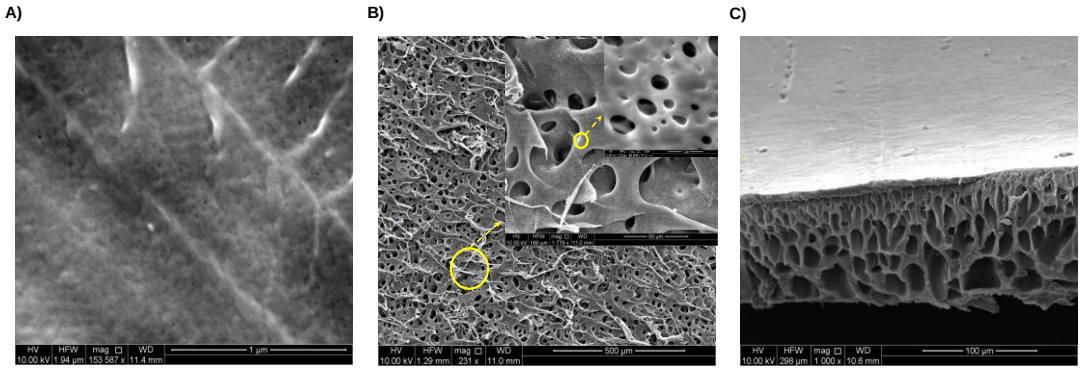

Fig 6S-2 A) surface, B) bottom and C) cross-section morphology of the fabricated PSF membrane used as the support for the TFC/TFN membranes' fabrication.

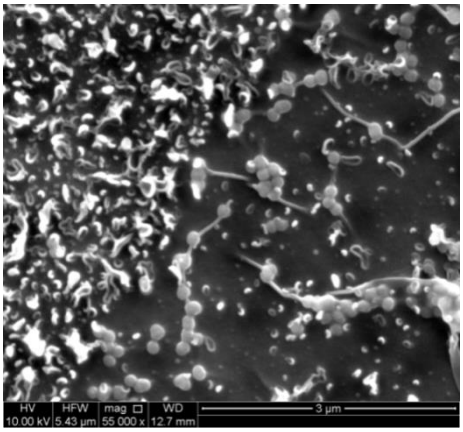

Fig 6S-3 The SEM image of an area on the edge of the fabricated TFN membrane containing 0.1 wt % SN-PEI. The area has a less PA like structure (more like a defected area) which might be due to its position in the side of the PA preparation frame which induces less monomers adsorbed to the PSF substrate. As seen, SN-PEI nanoparticles can be visibly seen on the surface and it is clear that the particles have contributed to the partially fulfilled interfacial polymerization reaction.

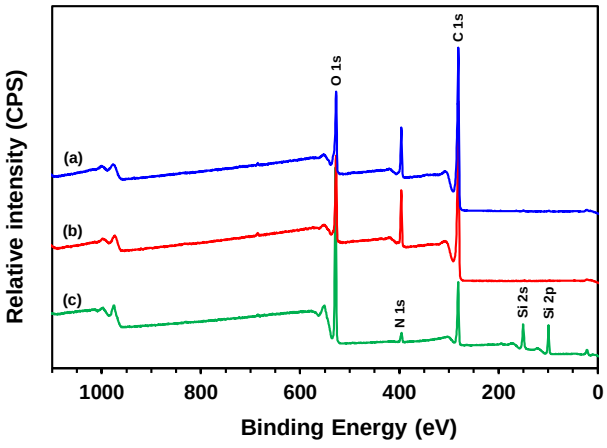

Fig 6S-4 The survey XPS spectra of a) TFN membrane containing 0.05 wt % SN-PEI, b) TFC membrane and c) SN-PEI.

Chapter 7

Conclusions

7.1. Conclusions

Thin film nanocomposite (TFN) membranes have received considerable attention recently due to their improved physicochemical properties (e.g. hydrophilicity, mechanical stability and thermal resistance) in addition to their higher permselectivity compared with the commonly used thin film composite (TFC) membranes. However, the future of TFN membranes is extremely dependent on the advancement of the developed nanoparticles and their sustainable and controllable incorporation into the TFC membranes. In fact, the incompatible nature of inorganic nanofillers and polymeric membranes makes it difficult to guarantee the longevity of improvements in the characteristics and performances of the developed TFN membranes. Hence, improving the integration of nanoparticles with polymeric membranes is extremely important. It is apparent that the reports to date fall short of fully understanding the structure-properties-performance correlation between the incorporated nanoparticles into the TFC membranes and their host polymer.

My PhD study was focused on the fabrication of various functional silica nanoparticles (SN) and thin film composite/nanocomposite (TFC/TFN) membranes. The main objective was to enhance the compatibility of inorganic nanosilica and polymeric TFC membranes and develop novel TFN membranes with improved physicochemical properties and desalination performance. SN with different sizes, surface functionalities and structures were synthesized and incorporated into the thin polyamide (PA) layer of TFC membranes and the structure-performance correlations of the developed TFN membranes were extensively evaluated. The integration of functional silica nanoparticles introduced herein with the PA layer of TFC membranes improved physicochemical properties and desalination performance of the developed TFN membranes. That proves the promising potential applications of the results for the future sustainable TFN membranes. The main conclusions drawn from my experimental results presented in Chapters 3-6 are summarized below:

In Chapter 3, statistical design and analysis on the three key TFC fabrication parameters including polysulfone (PSF) concentration in the phase inversion stage and aqueous phase soaking time and heat curing time in the interfacial polymerization course have been performed. Experimental data of desalination performance showed that for a higher PSF concentration, a higher MPD soaking time

gives the best performance. However, for a lower concentration of PSF, at low curing time, a lower MPD soaking time and at high curing time, a higher MPD soaking time are the optimum levels. This chapter highlights the importance of considering the interaction of parameters when devising a strategy to fabricate TFC membranes.

In Chapter 4, TFN membranes incorporated with various sizes and surface functionalized SN (amine, epoxy or hydroxyl groups) have been developed. The main focus is to understand the interaction of different SN and PA thin film layers of the resulting TFN membranes. The desalination performance evaluation of the fabricated membranes displays that no matter which functional group is present on SN, the resulting TFN membranes have higher water flux and comparable or higher salt rejection compared with the TFC membrane without any nanoparticle. Overall, covalent bond formation between SN-NH_2, SN-EPX and PA could improve the stability of SN inside the PA layer which eventually enhances the performance stability of the developed TFN membranes.

In Chapter 5, hollow mesoporous silica nanoparticles (HMSN) with an average particle size of ~ 68 nm have been synthesized and successfully incorporated into the thin PA layer of the TFC membranes. Various analytical techniques are applied to investigate the physicochemical properties of fabricated HMSN and resulting TFN membranes. The surface morphologies of the fabricated TFN membranes are changed after incorporating HMSN, and larger leaves on the PA layer contribute to the enhanced hydrophilicity of resulting TFN membranes. The water permeability of membranes increases up to 40 % after introducing HMSN with an optimum HMSN concentration of 0.03 wt % while negligible salt rejection compensation is observed. Moreover, TFN membranes show an improved compaction resistance which serves another advantage for their application.

In Chapter 6, polyethyleneimine (PEI) modified silica nanoparticles with an average particle size of ~ 100 nm have been fabricated and incorporated into the TFC membranes. Introduction of SN-PEI facilitates the formation of hydrophilic TFN membranes with more cross-linked PA layer. As a result, the developed TFN membranes show higher water flux and salt rejection compared with the TFC membrane without nanoparticles. Surface modification of SN with polymers having

the same end cap functional groups as PA monomers (m-phenylenediamine in this case) can strenghten the integration of nanoparticles with PA structre through covalent bonding. This coincides with the higher compatibility of polymer coated nanoparticles with the PA and can facilitate the sustainble improvement of the performance and properties of the developed TFN membranes.

7.2. Recommendations

For the further development of TFN membranes and advance desalinatation technology, the following recommendations in terms of scintific research and technology development are made based on the results generated from this PhD thesis:

- Influence of different surface functionality of nanomaterials and their polymeric modification on the other aspects of membrane performance such as fouling and chlorine attack resistance can be considered for further study.

- Considering the promising results obtained for the TFN membranes incorporated with PEI modified SN, the use of other hydrophilic polymers with different surface charge and functional groups as the surface modifier for the nanoparticles is recommended.

- Integration of polymer modified nanofillers with the support layer of TFC membranes is expected to improve the chemical structure and strength of the resulting nanocomposite supports and is therefore worthy of investigation.

- Integration of surface functionalized and polymer modifed HMSN with the PA and PSF layers of TFC membranes is also recommended to investigate the simultaneus contribution of the porousity and surface functionality of nanoparticles to the performance and properties of the resulting TFN membranes.